Inertial, Transient, and Turbulent Flow through Deformable and Propagating Fractures

Theory and Computational Engineering

by

Bruce Gee

A thesis
presented to the University of Waterloo
in fulfillment of the
thesis requirement for the degree of
Doctor of Philosophy
in
Civil Engineering

Waterloo, Ontario, Canada, 2023

Examining Committee Membership

The following served on the Examining Committee for this thesis. The decision of the Examining Committee is by majority vote.

External Examiner:	Dr. Brice Lecampion Associate Professor, Geo-Energy Laboratory, École Polytechnique Fédérale de Lausanne
Supervisor:	Dr. Robert Gracie Associate Professor, Dept. of Civil and Environmental Engineering, University of Waterloo
Internal Member:	Dr. Dipanjan Basu Professor, Dept. of Civil and Environmental Engineering, University of Waterloo
Internal-External Member:	Dr. Maurice B. Dusseault Professor, Dept. of Earth and Environmental Sciences, University of Waterloo
Internal-External Member:	Dr. Yuri Leonenko Associate Professor, Dept. of Earth and Environmental Sciences, University of Waterloo

Author's Declaration

This thesis consists of material all of which I authored or co-authored: see Statement of Contributions included in the thesis. This is a true copy of the thesis, including any required final revisions, as accepted by my examiners.

I understand that my thesis may be made electronically available to the public.

Statement of Contributions

This thesis consists of four manuscripts written for publication. Exceptions to sole authorship of material are as follows:

Chapters 1, 2, and 6 are based on the following journal article:

B. Gee and R. Gracie, "Beyond Poiseuille flow: A transient energy-conserving model for flow through fractures of varying aperture," *Advances in Water Resources*, vol. 164, p. 104192, 2022.

In this journal article, I was the primary author and was responsible for writing the article. Dr. Robert Gracie was responsible for editing the paper and conceptualization of the idea. I developed the methodology, conceptualized the verification cases, and performed the verification analysis of the developed model.

Chapters 1, 3, and 6 are based on the following journal article:

B. Gee and R. Gracie, "Beyond the cubic law: A finite volume method for convective and transient fracture flow," *International journal for numerical methods in fluids*, vol. 94, no. 11, pp. 1841–1862, 2022.

In this journal article, I was the primary author and was responsible for writing the article. Dr. Robert Gracie was responsible for editing the paper and conceptualization. I developed the mathematical formulation, implemented the computer code for the finite volume analysis, and ran the simulations.

Chapters 1, 4, and 6 are based on the following journal article:

B. Gee and R. Gracie, "Inertial and turbulent flow in hydro-mechanically coupled planar fractures," Submitted to *International Journal for Numerical and Analytical Methods in Geomechanics*, February 2023.

In this journal article, I was the primary author and was responsible for writing the article. Dr. Robert Gracie was responsible for editing the paper and conceptualization. I developed the mathematical formulation, implemented the computer code for the coupled system, and ran the simulations.

Chapters 1, 5, and 6 are based on the following journal article:

B. Gee and R. Gracie, "The Influence of Turbulence and Inertia in Radial Fracture Flow," Submitted for publication, April 2023.

In this journal article, I was the primary author and was responsible for writing the article. Dr. Robert Gracie was responsible for editing the paper and conceptualization. I developed the mathematical formulation, implemented the computer code for the coupled systems, and ran the simulations.

Abstract

Fluid flow in deformable fractures is important to many natural and industrial geological engineering applications including contaminant transport, geothermal energy, and hydraulic stimulation. Large-scale simulations of flow through fractures are almost exclusively based on the Poiseuille flow model which contains the ingrained assumptions of laminar quasi-steady-state flow conditions with negligible inertia. The high flow rates involved in industrial applications bring these assumptions into question, but the only alternative is the Navier-Stokes equations which are computationally prohibitive at reservoir scales. This thesis seeks to address the gap in available models by introducing a new reduced-dimension model that is capable of capturing inertial and transient flow behaviours without the computational burden of the Navier-Stokes equations.

First, a new fracture flow model is derived from the higher-dimensional Navier-Stokes equations by integrating over the fracture aperture and making simplifying assumptions which are less restrictive than those of Poiseuille flow. This new model, dubbed the GG22 fracture flow model, yields a two-field model (fluid flux and pressure) governed by the conservation of mass and momentum. The GG22 model conserves energy and is shown to include both Poiseuille flow and Forchheimer flow as limiting cases. The performance of the GG22 model is verified against the existing Poiseuille flow model and the solution to the full Navier-Stokes equations in three benchmarks problems. The GG22 model demonstrates complex transient and inertial behaviours not previously captured and produces up to 400% improvements in error over Poiseuille flow in steady-state flow conditions for $1 \leq Re \leq 100$. The GG22 model is demonstrated to be superior in all tested applications where the inertial forces are greater than viscous forces ($Re \geq 1$) and when aperture varies in space and/or time.

Next, a simulator to solve the GG22 governing equations in rigid fractures is developed. Novel numerical methods were developed as the GG22 model is more complex than Poiseuille flow. Since the GG22 model is derived from the Navier-Stokes equations, numerical methods developed for the Navier-Stokes equations may be adapted, but the new model contains its own idiosyncrasies which must be addressed. An explicit multistep finite volume method is developed and verified. The method is based on deriving a Poisson equation for pressure with an additional continuity correction to overcome numerical instabilities. The critical timestep is derived and shown to be a function of the fundamental frequency of the fracture-fluid system and the maximum fluid velocity. The results show excellent agreement with analytical solutions, and the method demonstrates a first-order rate of fluid flux convergence in time and a second-order rate of pressure convergence in space. Applying the model to a travelling aperture wave simulating seismic excitation reveals the changes in behaviours introduced by inertia and transience. These behaviours include lower average fluxes, higher pressures, and phase-shifts in the fluid response compared to the predictions of Poiseuille flow.

Finally, the GG22 model is numerically coupled with mechanical deformation of a rock mass to simulate the complex industrial applications of interest. A monolithic fully-coupled hydro-mechanical finite element - finite volume model with cohesive fracture propagation is developed and verified. The Newton-Raphson solution algorithm demonstrates poor

iterative convergence behaviour, so an adaptive steepest descent line-search with Aitken relaxation is introduced to improve the rate of convergence. The hydro-mechanical model is applied to fracture flow between oscillating elastic plates. The combined effects of inertia and transience are demonstrated to create phase-shifts in the fluid response, larger fluid pressures and rock mass stresses compared to the Poiseuille flow predictions, and induce wave-like behaviour even in a quasi-static rock mass.

The hydro-mechanically coupled fracture propagation model is used to examine the role of inertia and turbulence in the propagation of planar KGD-like and axisymmetric radial hydraulic fractures with constant fluid injection rates. In KGD-like fracture, inertial effects are negligible at flow rates that could be expected in practice. If the injection rate is large enough to invoke turbulence, then significantly different fracture propagation behaviour is observed. Turbulence in KGD-like fractures leads to shorter fractures with larger apertures due to the increased fluid resistance. In radial fractures, the effects of inertia and turbulence only manifest near the wellbore and lead to changes in fracture shape, but have little impact on tip behaviour or fracture length. Turbulence creates increased wellbore pressures and apertures while inertial effects decrease the wellbore pressure and aperture. Turbulent and inertial effects near the wellbore account for the majority of the pressure loss along the fracture and provide a potential explanation for the empirically observed phenomenon of entrance losses. Turbulent and inertial forces have significant effects on injection pressure predictions, and predictions which neglect these phenomena are likely to exhibit significant deviations from the true pressure behaviour. Using water as the injection fluid, turbulence is the dominant mechanism that leads to departures from the Poiseuille flow solution at high Re. The solution departs immediately upon the manifestation of turbulence ($Re \geq 2\times10^3$), while inertial effects manifest at higher flow rates ($Re \geq 2 \times 10^4$). Using slickwater as the injection fluid, the opposite trend is observed: inertial effects manifest first at modest flow rates ($Re \geq 10^4$), while turbulent effects are delayed to higher flow rates ($Re \geq 2 \times 10^4$).

In general, high Reynolds number flow is more common in industrial fracture flow applications than considered by current models. The threshold for departure from the Poiseuille flow solution is low and the differences in the solutions are large. This thesis provides a new model to bridge the gap between the physically restrictive Poiseuille flow model and the computationally prohibitive Navier-Stokes equations for the simulation of coupled flow processes in fractures. This new model provides a resource for the analysis and viability of many different applications including geothermal energy, carbon storage, seismic analysis, and contaminant transport among many others. It is recommended that the GG22 model be adopted for the modelling of fracture flow applications in all cases.

Acknowledgements

I would like to thank everyone who supported me through my studies and made this thesis possible. I would first like to thank the members of my committee for reviewing my work providing thoughts and feedback. I would also like to thank the Natural Sciences and Engineering Research Council of Canada for providing the funding for my research.

I would like to express my sincere gratitude to Dr. Robert Gracie for his council, motivation, mentorship throughout my studies. He has provided me with invaluable technical knowledge and opportunities to travel and interact with other researchers in my field.

I would like to extend a special thanks to Dr. Thomas-Peter Fries for hosting me at TU Graz for the short time I was there, and Dr. Richard Schussnig who saved me countless hours of computation by introducing me to the Aitken relaxation method. I would also like to thank my colleagues past and present in the Computational Mechanics research group for their discussions and feedback.

Lastly, I would like to thank all my friends for keeping me grounded and sane throughout this process, and my loving family for their tireless support.

Table of Contents

List of Figures

List of Tables

Chapter 1

Introduction

1.1 Flow Through Fractures

Fractures are mechanical separations in a rock mass that divide the matrix into smaller pieces. The flow of fluid through fractures is an important aspect of many natural and industrial processes. In contaminant transport and groundwater flow, fractures form the primary pathway for flow through low permeability rock masses [1, 2]. Flow in fractures is known to enhance the permeability of porous media under seismic loads [3, 4]. In engineered processes like hydraulic stimulation and geothermal heat extraction, large volumes of fluid are rapidly forced through thin fractures and fracture networks [5, 6, 7], as illustrated in Figure 1.1.

Models and simulations of flow in fractures, be they deformable or rigid, are almost exclusively based on Poiseuille flow – the analytical solution to the incompressible Navier-Stokes equations for steady flow between rigid parallel plates. It states that the pressure gradient is related to the mean velocity by

$$\nabla p = -\frac{12\mu}{w^2}\overline{\boldsymbol{v}} = -\frac{12\mu}{w^3}\boldsymbol{q} \tag{1.1}$$

in which w is the aperture between the plates, μ is the kinematic viscosity, $\overline{\boldsymbol{v}}$ is the mean velocity, and ∇p is the pressure gradient [8, 9]. Equation (1.1) is often presented in terms of the fluid flux, $\boldsymbol{q}$, where it has earned the name "the cubic law" due to its ubiquity in modelling fracture flow. Throughout this thesis, the terms "Poiseuille flow" and "the cubic law" will be used interchangeably.

In simulations involving deformable fractures, conservation of mass is derived at the fracture scale using a control volume, such that

$$\dot{w} = -\nabla \cdot \boldsymbol{q} \tag{1.2}$$

in which $\boldsymbol{q}$ is the fluid flux given by the cubic law in equation (1.1). This upscaled statement of conservation of mass admits both time and spatially varying aperture, in contrast to

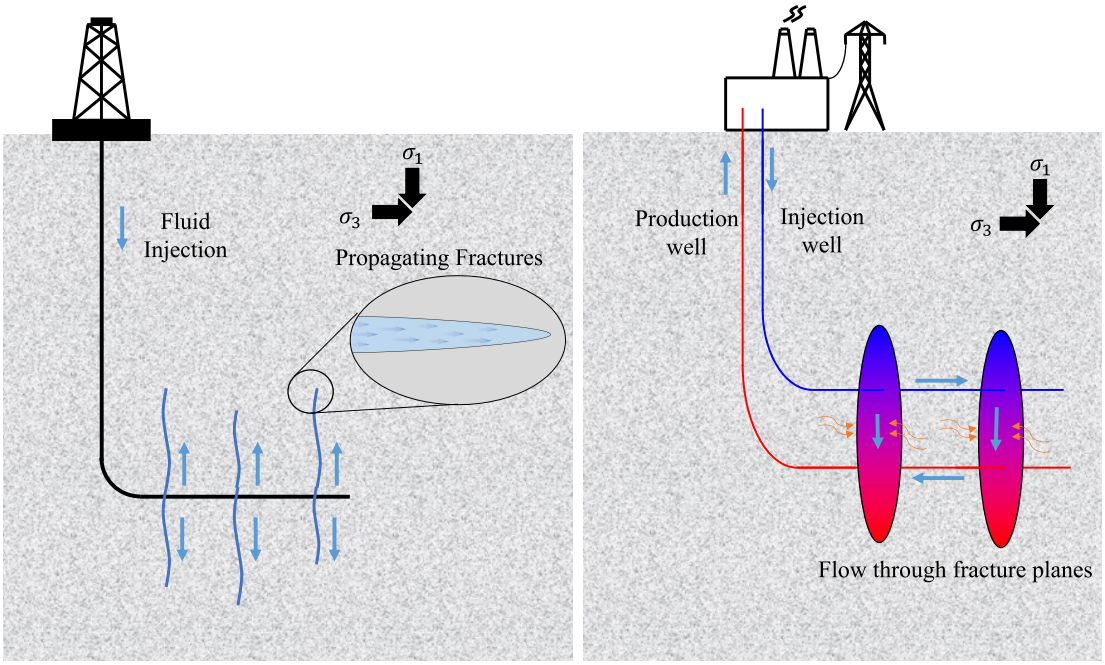

(a) Hydraulic Stimulation (b) Enhanced Geothermal System

Figure 1.1: Engineered fracture flow applications

the assumptions underpinning Poiseuille flow. Equation (1.1) and (1.2) are widely used in fracture flow modelling and have been extended to many applications, including two-phase flow [10], non-wetting fluid flow [11], and hydraulic stimulation with proppant transport [12, 13] to name a few.

Computationally, Poiseuille flow is advantageous for modelling fractures at the reservoir scale. At the scale of an individual fracture, it is more common to use the full Navier-Stokes equations to model flow behaviour in the viscous flow regime through non-parallel fracture geometries, and to model the non-linear flow behaviour that arises at higher flow rates [14, 15, 16]. At the reservoir scale, the width of a single fracture is many orders of magnitude smaller than the reservoir, and so it often computationally prohibitive to use the full Navier-Stokes equations to model flow behaviour. Hence the development of reduced-dimension flow models, like Poiseuille flow (among others [17, 18]), which decrease the computational burden. Especially in multiphysics problems like hydraulic stimulation [7, 12, 13, 19] or enhanced geothermal energy production [6, 20, 21], the computational cost of coupling the full Navier-Stokes equations with other processes like rock mass deformation, heat transfer, or crack propagation is often prohibitive. The standard unmodified cubic law model is ubiquitous for modelling flow behaviour in these problems.

Despite its widespread use, fracture flow models based on Poiseuille flow have a number of limitations. The underpinning assumptions are often violated, including: a) that flow is steady, b) that the aperture can be locally approximated by parallel plates (even beyond consideration for surface roughness), c) that inertial forces are negligible, d) that flow is laminar, and e) that the rock matrix is impermeable. The assumption of impermeable walls is often violated when Poiseuille flow is applied to modelling flow through fractured

porous media, but this issue has previously been addressed by modifying Poiseuille flow to account for the fluid leak-off through permeable fracture walls [22, 23, 24]. Previous works which have examined fluid-driven crack propagation with alternative flow assumptions like turbulent flow [25, 26] or non-Newtonian fluids [27, 28], have shown that laminar flow conditions occur in a majority of industrial cases, and suggest that inertial terms are only important at very early times when the injection rate is constant. However, these analyses do not address the inertial effects from non-parallel plate geometries, or the complex transient effects that arise from new hydraulic stimulation techniques like pressure pulsing [29] or dynamic stress effects induced by seismicity [3, 4].

There is therefore a need for a new model of fracture flow that is capable of capturing the transient and inertial physics of flow through non-parallel apertures at moderate to large Reynolds numbers. It would also be advantageous if such a model is not burdened by the same computational expense that accompanies the full Navier-Stokes equations. In this thesis, the derivation of such a model is presented and verified against numerical and analytical solutions. It is applied to common industrial fracture flow scenarios to examine the behaviour of inertial, transient, and turbulent fluid physics.

1.2 The Applicability of Poiseuille Flow

Poiseuille flow has been extensively studied analytically, numerically, and experimentally. Much of the work has focused on the validity of Poiseuille flow as it applies to surface roughness and tortuosity, and modifications to Poiseuille flow have been proposed to address these factors [14, 30, 31, 32]. Several studies of Poiseuille flow have devised criteria for when Poiseuille flow-based models are appropriate [9, 33]. These recommendations on the range of applicability of Poiseuille flow for fractures are often violated in modern modelling works. For example, in Rivas & Gracie [13] and Gee & Gracie [34], flow rates are applied in excess of the limits on the range of applicability. In Parchei-Esfahani *et al.* [29] hydraulic stimulation via pressure pulsing was modeled, but transient effects in the fluid were neglected by adopting the quasi-static Poiseuille flow, despite the dynamic nature of the problem.

The range of applicability of Poiseuille flow must be $Re \leq 1$ for the flow to be in the laminar regime in non-parallel fractures. Poiseuille flow departs significantly from the true fluid behaviour in fractures of varying aperture at even moderate Reynolds numbers ($Re \geq 1$). Experimental results of fracture flow have shown that Poiseuille flow using the average aperture of the fracture produces relatively accurate results up to a Reynolds number $Re \leq 10$, after which flow becomes non-linear [8, 35, 36, 37]. More recent reviews have shown that the onset of non-linear flow behaviour can range from $0.1 \leq Re \leq 60$, depending on mechanical factors such as shear dilation, confining stresses, and surface roughness [38]. The only flow model which has attempted to account for the inertial non-linear flow behaviour observed at higher Reynolds numbers is Forchheimer flow, a non-linear extension originally developed for non-Darcian flow through porous media and adapted to fracture flow [39]. Forchheimer flow relies on an empirical coefficient to capture the nonlinear behaviour, and while there have been attempts to calibrate this empirical

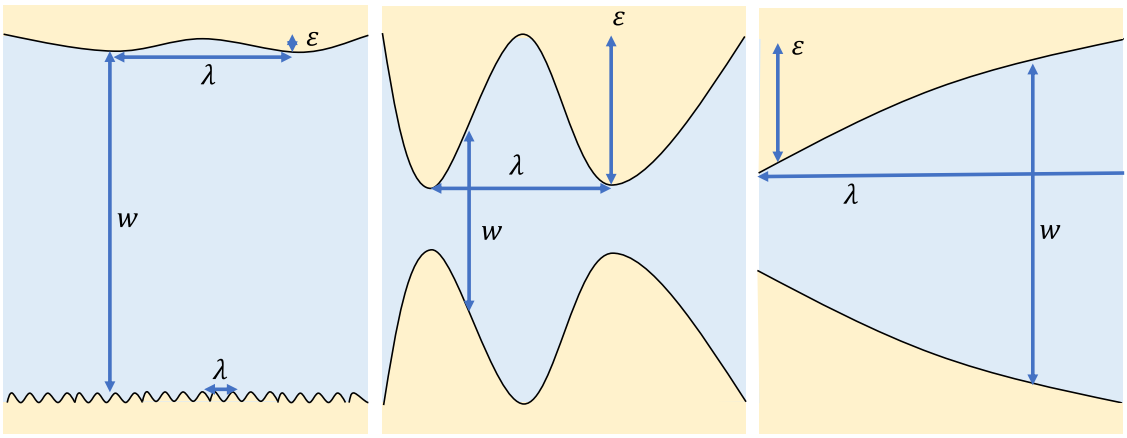

(a) $\varepsilon << w$ (b) $\varepsilon \sim \lambda \sim w$ (c) $\varepsilon \sim w, \lambda > w$

Figure 1.2: Different classes of fractures based on the ratios of surface roughness, aperture, and wavelength.

coefficient [35, 36], Forchheimer flow rarely sees any use in modern fracture flow simulations. In practice, the flow rates of interest in industrial applications regularly exceed $Re \geq 100$. For example, in a wellbore with a diameter of $15cm$, a flow rate of $1L/s$ generates Reynolds numbers in excess of $Re > 2000$ assuming water as the injection fluid. Thus, industrial applications regularly exceed even the most generous upper bounds on the applicability of Poiseuille flow.

1.3 Conceptual Fracture Models

There are numerous ways to conceptually conceive of a rock mass fracture. At its core, the conceptual model adopted by most modelling works is to consider a fracture as a fluid filled volume between the rock mass in which flow is unobstructed. Figure 1.2 illustrates three different theoretical classes of fractures which are described by combinations of hydraulic aperture, w, surface asperities, ε, and wavelength, λ.

The first class, illustrated in Figure 1.2a, is the case where the asperities are small compared to the aperture. In this class, the fracture is conceptually a pipe or channel with some surface roughness – fluid flow transverse to the axis of the fracture is relatively minimal. This class of fracture is reasonably well approximated by the cubic law, except at high Reynolds numbers when the flow becomes turbulent.

The second class, illustrated in Figure 1.2b, is the case in which the asperities, wavelength, and aperture are all approximately the same order. Most natural fractures fall within this second class. Asperities of this order are often lumped together with the first class and called "surface roughness". There have been many efforts to modify the cubic law to account for the deviations caused by these asperities by introducing factors and correlations with the surface roughness [14, 30, 31]. However, the transverse component of flow in this second class of fractures is significant, especially at higher Reynolds numbers, and can never

be adequately described by a reduced dimension model which removes the transverse flow component.

The third class of fractures, illustrated in Figure 1.2c, is the conceptual model adopted throughout this thesis. Asperities and aperture may be of similar order, and consequently the change in aperture is large and important, but the wavelength over which the aperture changes is large and the transverse component of flow is small. The walls of the fracture are typically considered smooth, but small surface roughness (akin to the first class of fracture) may exist such that it does not significantly impact the flow in the middle of the channel. This class of fracture is the standard idealized geometry adopted for fractures in most modern fracture flow modelling works [5, 6, 7, 40] as it permits models to neglect the transverse flow component.

1.4 Purpose and Objectives

Thus, given the need for a new fracture flow model to balance the needs of physical accuracy with computational expense, the objectives of this thesis are presented in this section.

1.4.1 Objective 1: Develop a new reduced-dimension model for fracture flow that captures inertial, transient, and turbulent behaviours

The first objective is to develop a mathematical model for fracture flow that is capable of capturing inertial, transient, and turbulent flow behaviours in fractures without the computational expense that accompanies the full Navier-Stokes equations. The developed mathematical model consists of a set of partial differential equations which govern the conservation of fluid mass and the conservation of fluid momentum in a deformable, propagating fracture. This new model is labeled the "GG22 flow model" after its publication reference [41]. The new model is derived from the higher-dimension Navier-Stokes equations by integrating over the fracture aperture and making simplifying assumptions to generate a reduced-dimension model. The model is then verified against analytical and numerical solutions. It is shown that the GG22 model recovers the Poiseuille flow model under Poiseuille flow conditions and performs no worse than Poiseuille flow in all tested fracture flow situations [41]. Furthermore, the GG22 model conserves energy in non-parallel plate geometries where Poiseuille flow does not. This objective is completed in Chapter 2 which is based on the article:

B. Gee and R. Gracie, "Beyond Poiseuille flow: A transient energy-conserving model for flow through fractures of varying aperture," *Advances in Water Resources*, vol. 164, p. 104192, 2022.

1.4.2 Objective 2: Develop a simulator for fluid flow in rigid fractures

Following the derivation of the new model, the second objective is to develop a simulator to solve non-trivial fracture flow problems in rigid fractures. The increased physical accuracy of the GG22 model comes at the cost of increased complexity, albeit much less than the full Navier-Stokes equations. The single constitutive equation of Poiseuille flow is replaced with a set of two coupled partial differential equations. Consequently, novel numerical methods are required to solve the equations and simulate the flow behaviour. Luckily, the Navier-Stokes equations and GG22 model share similarities in form, so existing numerical methods from computational fluid dynamics may be adopted. However, the GG22 model contains several idiosyncrasies which must be addressed. This objective is completed by developing an explicit multi-step finite volume method for the GG22 model. The algorithm involves the derivation of a Poisson equation for pressure, and the introduction of a continuity correction to overcome numerical instabilities. The method is then verified against analytical solutions and then applied to non-trivial boundary value problems. This objective is described in Chapter 3 which is based on the article:

B. Gee and R. Gracie, "Beyond the cubic law: A finite volume method for convective and transient fracture flow," *International journal for numerical methods in fluids*, vol. 94, no. 11, pp. 1841–1862, 2022.

1.4.3 Objective 3: Develop a multi-physics simulator for fluid flow coupled with rock mass deformation and fracture propagation

Next, the third objective is to develop a multi-physics simulator that couples the numerical model with mechanical rock mass deformation and fracture propagation. A mixed finite element - finite volume model is developed to solve the coupled hydro-mechanical GG22 equations. Finite elements are used for the rock mass under in-situ stresses, and a cohesive zone model with a cubic traction-separation law is introduced to model the quasi-brittle crack propagation behaviour. A monolithic numerical method is derived and numerical convergence issues are addressed. The model is applied to sample problems and compared against the Poiseuille flow and analytical solutions, as well as the propagation of KGD-like planar fractures. This objective is completed in Chapter 4 which is based on the article:

B. Gee and R. Gracie, "Inertial and turbulent flow in hydro-mechanically coupled planar fractures," Submitted to *International Journal for Numerical and Analytical Methods in Geomechanics*, February 2023.

1.4.4 Objective 4: Investigate the role of inertia and turbulence encountered in hydraulic stimulation and fracture propagation

The final objective was to apply the coupled hydro-mechanical model to hydraulic stimulation and examine how the phenomena of inertia and turbulence manifest during fracture propagation. The model is applied to fracture propagation of an axisymmetric/radial fracture from a wellbore. A single sample problem setup is considered and the various layers of physics are applied one at a time to isolate their contribution. The problem is investigated with both water and slickwater as the fracturing fluid. It is shown that these phenomena have significant effects on the near-wellbore behaviour of the system and significantly impact both pressure and aperture. It is observed that turbulence manifests at lower flow rates than inertia in water, but the opposite trend is observed in slickwater. This objective is described in Chapter 5 which is based on the article:

B. Gee and R. Gracie, "The Influence of Turbulence and Inertia in Radial Fracture Flow," Submitted for publication, April 2023.

Chapter 2

The GG22 Fracture Flow Model

2.1 Introduction

In this chapter, an improved fracture flow model, labeled the GG22 flow model, is derived and verified. It overcomes many of the limitations of the Poiseuille flow model by capturing the inertial and transient behaviour of fluid flow through fractures of varying and deformable aperture in inertia dominant flow ($Re > 1$). Whereas previous modelling efforts have focused on modifying Poiseuille flow [14, 30, 31], we start from the full set of Navier-Stokes equations and make simplifying assumptions, thereby deriving a reduced dimension flow model which simplifies the fracture volume into a fracture plane. The new reduced dimension model is verified against the full Navier-Stokes solution and compared to Poiseuille flow in the cases of transient flow, and spatially and temporally varying aperture fields. The new proposed model captures inertial behaviour previously neglected, conserves energy in fractures where Poiseuille flow does not, and more accurately models transient and steady-state flows through fractures with spatially varying aperture.

In Section 2.2, a reduced dimension formulation for flow through fractures of deformable aperture is developed, and the cases of laminar and turbulent flow are discussed. Section 2.3 provides a physical interpretation of each term in the reduced dimension model and examines a number of corollaries which can be derived from the reduced dimension model. Next, Section 2.4 verifies the model with several analytical and numerical problems in which the reduced dimension model is compared against both Poiseuille flow and the full Navier-Stokes solutions. The models are compared both qualitatively and quantitatively.

2.2 Model Derivation

This section develops a reduced dimension set of governing equations for flow through deformable thin varying channels starting from the two-dimensional Navier-Stokes equations. The methodology is adapted from the models for flow through an elastic artery set out by Olufsen *et al.* [42] and Smith *et al.* [43].

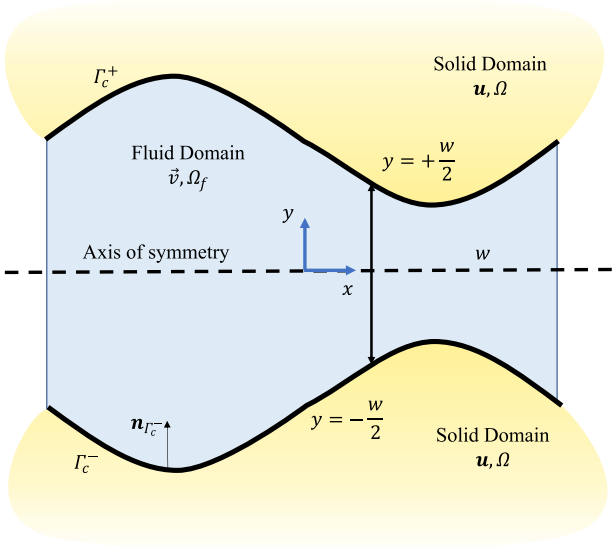

Figure 2.1: Symmetrical fluid-solid domain.

2.2.1 Derivation of the reduced dimensions governing equations

Consider the flow of fluid through a thin fracture that is wide in the z-direction. The flow of fluid is governed by the two-dimensional Navier-Stokes equations. The problem domain is illustrated in Figure 2.1. Let x and $v_x(x, y, t)$ be the coordinate and velocity along the longitudinal axis. Let y and $v_y(x, y, t)$ be the transverse coordinate and velocity. The fracture is characterized by a scalar aperture, $w(x, t)$, which is positive and non-zero at all points in the domain. Flow in the out-of-plane direction is negligible, $v_z \approx 0$.

Assumption 1 *The flow is assumed to be symmetrical across the longitudinal centerline of the fracture.*

Assumption 2 *The fluid is incompressible and Newtonian.*

Assumption 3 *The rock mass is an impermeable solid, such that no fluid leak-off occurs through the fracture walls.*

The two-dimensional Navier-Stokes equations for an incompressible Newtonian fluid are given as

$$\nabla \cdot \vec{v} = 0 \tag{2.1}$$

$$\rho_f \left(\frac{\partial \vec{v}}{\partial t} + \vec{v} \cdot \nabla \vec{v} \right) = -\nabla p + \mu \nabla^2 \vec{v} \tag{2.2}$$

in which $\nabla p = \nabla P - \rho_f g \vec{k}$ is the modified pressure which includes gravity effects. Next, we will non-dimensionalize all quantities such that $y = \frac{\overline{w}}{2} y^*$, $x = \lambda x^*$, $v_x = V v_x^*$, $v_y = U v_y^*$, $t = \frac{\lambda}{V} t^*$, $p = \rho_f V^2 p^*$ in which $\overline{w}$ is a characteristic aperture, V is a characteristic velocity in the longitudinal direction, and U is a characteristic velocity in the transverse direction. Let λ be a characteristic length defined as $\lambda = \frac{\overline{w}}{2} \frac{V}{U}$. Expanding the non-dimensionalized

equations, we find

$$\frac{\partial v_x^*}{\partial x^*} + \frac{\partial v_y^*}{\partial y^*} = 0 \tag{2.3}$$

$$\frac{\partial v_x^*}{\partial t^*} + v_x^* \frac{\partial v_x^*}{\partial x^*} + v_y^* \frac{\partial v_x^*}{\partial y^*} = -\frac{\partial p^*}{\partial x^*} + \frac{4\mu\lambda}{\rho_f V \overline{w}^2} \left(\frac{U^2}{V^2} \frac{\partial^2 v_x^*}{\partial x^{*2}} + \frac{\partial^2 v_x^*}{\partial y^{*2}} \right) \tag{2.4}$$

$$\frac{U^2}{V^2} \left(\frac{\partial v_y^*}{\partial t^*} + v_x^* \frac{\partial v_y^*}{\partial x^*} + v_y^* \frac{\partial v_y^*}{\partial y^*} \right) = -\frac{\partial p^*}{\partial y^*} + \frac{U^2}{V^2} \frac{2\mu}{\rho_f \overline{w} U} \left(\frac{U^2}{V^2} \frac{\partial^2 v_y^*}{\partial x^{*2}} + \frac{\partial v_y^*}{\partial y^{*2}} \right) \tag{2.5}$$

Assumption 4 *The transverse velocity is much smaller than the longitudinal velocity, $v_x >> v_y$, $V >> U$. Therefore, this derivation is not applicable to flows which have a significant transverse flow component.*

Assuming the transverse velocity is small compared to the longitudinal velocity allows us to state that $\frac{U^2}{V^2} \approx 0$. This implies that the longitudinal viscous forces are negligible, and that $\frac{\partial p^*}{\partial y^*} = 0$, such that the pressure is constant across the aperture. The equations are reduced to

$$\frac{\partial v_x^*}{\partial x^*} + \frac{\partial v_y^*}{\partial y^*} = 0 \tag{2.6}$$

$$\frac{\partial v_x^*}{\partial t^*} + v_x^* \frac{\partial v_x^*}{\partial x^*} + v_y^* \frac{\partial v_x^*}{\partial y^*} = -\frac{\partial p^*}{\partial x^*} + \frac{4\mu\lambda}{\rho_f V \overline{w}^2} \frac{\partial^2 v_x^*}{\partial y^{*2}} \tag{2.7}$$

Equations (2.6) and (2.7) contain three unknowns in two equations, so we will make further assumptions and manipulations to remove v_y^* from these equations. Next, we will integrate equations (2.6) and (2.7) over the aperture. Let $\overline{w} w^* = w$ be the non-dimensionalized fracture aperture. We will first examine the integration of equation (2.6). Since x^* is independent from y^*, the integral may be written as

$$2\frac{\partial}{\partial x^*} \int_0^{w^*/2} v_x^* dy^* - \frac{\partial w^*}{\partial x^*} (v_x^*)\Big|_{w^*/2} + 2\int_0^{w^*/2} \frac{\partial v_y^*}{\partial y^*} dy^* = 0 \tag{2.8}$$

$$2\frac{\partial}{\partial x^*} \int_0^{w^*/2} v_x^* dy^* - \frac{\partial w^*}{\partial x^*} (v_x^*)\Big|_{w^*/2} + 2(v_y^*)\Big|_0^{w^*/2} = 0 \tag{2.9}$$

Assumption 5 *No-slip conditions are assumed at the fracture surface, and the shear displacement of the fracture surface is assumed to be small compared to its transverse movement, such that $v_x\Big|_{w/2} = \dot{u}_x\Big|_{w/2} \approx 0$, in which $\dot{u}_x$ is the longitudinal rock mass velocity. Therefore, this derivation is not applicable to flows in which the longitudinal movement/shear displacement of the fracture surfaces is large.*

No-slip conditions are assumed at the fracture surface, which implies that the fluid velocity at the wall is equal to the velocity of the wall. The shear velocity of the wall is then assumed to be small compared to its transverse movement, such that it is negligible. The boundary condition is therefore stated as

$$v_x^*\Big|_{w^*/2} = 0 \tag{2.10}$$

While longitudinal movement of the rock mass is assumed to be small, transverse movement is not neglected. The rate of aperture change, $\dot{w^*}$, is equal to the sum of the transverse velocity of each fracture surface. Therefore, due to symmetry and the no-slip boundary condition, the transverse velocity at the fracture surface is

$$v_y^*\Big|_{w^*/2} = \frac{1}{2}\frac{\partial w^*}{\partial t^*} \tag{2.11}$$

Next, let the non-dimensional fluid flux through the fracture be defined as

$$q^* = 2\int_0^{w^*/2} v_x^* dy^* = w^*\overline{v_x^*} \tag{2.12}$$

in which $\overline{v_x^*}$ is the mean velocity over the aperture. Simplifying equation (2.9) with equations (2.10), (2.11), and (2.12), the continuity equation is given as

$$\frac{\partial q^*}{\partial x^*} + \frac{\partial w^*}{\partial t^*} = 0 \tag{2.13}$$

Next, we will examine the conservation of momentum given by equation (2.7). Integrating the equation over the aperture gives

$$\begin{aligned}\frac{\partial}{\partial t^*}\left(2\int_0^{w^*/2} v_x^* dy^*\right) - \frac{\partial w^*}{\partial t}v_x^*\Big|_{w^*/2} + 2\int_0^{w^*/2}\left(v_x^*\frac{\partial v_x^*}{\partial x^*} + v_y^*\frac{\partial v_x^*}{\partial y^*}\right)dy^* \\ = -w\frac{\partial p^*}{\partial x^*} + \frac{4\mu\lambda}{\rho_f V w^2}\left[2\int_0^{\overline{w}^*/2}\frac{\partial^2 v_x^*}{\partial y^{*2}}dy^*\right]\end{aligned} \tag{2.14}$$

The first term in equation (2.14) may be simplified using equation (2.12), such that

$$\frac{\partial}{\partial t^*}\left(2\int_0^{w^*/2} v_x^* dy^*\right) = \frac{\partial q^*}{\partial t^*} \tag{2.15}$$

while the second term disappears through the no-slip boundary condition (2.10). The third term in (2.14) can be simplified through the continuity equation (2.6) and integration by parts. This operation is the one-dimensional equivalent to inversing the simplification of the convective term in the incompressible Navier-Stokes equation, where $\nabla\cdot(\vec{v}\vec{v}) = \vec{v}\nabla\cdot\vec{v} + \vec{v}\cdot\nabla\vec{v}$, and $\nabla\cdot\vec{v} = 0$ from continuity.

$$2\int_0^{w^*/2}\left(v_x^*\frac{\partial v_x^*}{\partial x^*} + v_y^*\frac{\partial v_x^*}{\partial y^*}\right)dy^* = 2\int_0^{w^*/2}\left(v_x^*\frac{\partial v_x^*}{\partial x^*} - v_x^*\frac{\partial v_y^*}{\partial y^*}\right)dy^* \tag{2.16}$$

From equation (2.6), $\frac{\partial v_x^*}{\partial x^*} = -\frac{\partial v_y^*}{\partial y^*}$,

$$= 2\int_0^{w^*/2}\left(v_x^*\frac{\partial v_x^*}{\partial x^*} - v_x^*\left(-\frac{\partial v_x^*}{\partial x^*}\right)\right)dy^* \tag{2.17}$$

$$= \frac{\partial}{\partial x^*}\left(2\int_0^{w^*/2}(v_x^*)^2 dy^*\right) \tag{2.18}$$

We can further simplify this term by assuming that we know something about the shape of the velocity profile across the aperture.

Assumption 6 *Let the velocity $v_x^*(x^*, y^*, t^*)$ be expressed as $v_x^*(x^*, y^*, t^*) = \overline{v_x^*}(x^*, t^*) \cdot N\left(\frac{y^*}{w^*}, x^*\right)$, in which N is a shape function describing the velocity profile over the aperture. N is expressed as a function of the position along the aperture, y^*/w^*.*

We will introduce a momentum correction factor, α, which will allow us to express (2.18) as a function of the dimensionless fluid flux and aperture. The momentum correction factor is determined as

$$2\int_0^{w^*/2}(v_x^*)^2 dy^* = 2\int_0^{w^*/2}\left(\overline{v_x^*}N\right)^2 dy^* = \alpha\frac{(q^*)^2}{w^*} \tag{2.19}$$

$$\alpha(x^*) = \frac{2}{w^*}\int_0^{w^*/2}\left(N\left(\frac{y^*}{w^*}, x^*\right)\right)^2 dy^* \tag{2.20}$$

Thus, assuming we know the velocity profile across the aperture, we can determine the momentum correction factor. The momentum correction factor can be interpreted as a measure of how much more momentum is forced into a control volume by the non-constant velocity profile compared to a uniform velocity profile. $\alpha = 1$ would indicate a perfectly uniform velocity profile, which would be physically inadmissible due to the no-slip boundary conditions, therefore $\alpha > 1$ for all physically admissible velocity profiles. In plug flow conditions, where $v_{xmax}^* \approx \overline{v_x^*}$, $\alpha \to 1$. For fully developed duct flow with a parabolic velocity profile in which $v_{xmax}^* = 1.5\overline{v_x^*}$, $\alpha = 1.2$. $\alpha > 1.2$ indicates a sharper velocity profile than parabolic, in which the maximum velocity is greater than $1.5\overline{v_x^*}$. The momentum correction factor is a unitless scalar but is not necessarily a constant if the velocity profile changes along the fracture.

Last, consider the shear stress term from equation (2.14).

$$\kappa\left[2\int_0^{w^*/2}\frac{\partial^2 v_x^*}{\partial y^{*2}}dy^*\right] = 2\kappa\frac{\partial v_x^*}{\partial y^*}\bigg|_0^{w^*/2}, \quad \kappa = \frac{4\mu\lambda}{\rho_f V\overline{w}^2} \tag{2.21}$$

From the symmetry condition at the centerline, the shear stress is subject to the boundary condition

$$\frac{\partial v_x^*}{\partial y^*}\bigg|_0 = 0 \tag{2.22}$$

So that the shear stress term becomes

$$f^{v*} = 2\kappa\frac{\partial v_x^*}{\partial y^*}\bigg|_{w^*/2} \tag{2.23}$$

and is therefore a body force term equal to the shear stress that is exerted on the fracture walls by the fluid. Combining the various terms, the conservation of momentum is therefore given as

$$\frac{\partial q^*}{\partial t^*} + \frac{\partial}{\partial x^*}\left(\alpha\frac{(q^*)^2}{w^*}\right) = -w^*\frac{\partial p^*}{\partial x^*} + f^{v*} \tag{2.24}$$

2.2.2 Dimensional form of the governing equations

The parameter $\kappa = \kappa(\lambda), \lambda = \lambda(U)$ is the only part of the formulation that is dependent on the transverse velocity, U. We can remove this dependence by transferring the system of equations back to dimensional form.

$$\frac{\partial q}{\partial x} + \frac{\partial w}{\partial t} = 0 \tag{2.25}$$

$$\frac{\partial q}{\partial t} + \frac{\partial}{\partial x}\left(\alpha \frac{q^2}{w}\right) = -\frac{w}{\rho_f}\frac{\partial p}{\partial x} + f^v \tag{2.26}$$

$$\alpha = \frac{2}{w}\int_0^{w/2} N^2 dy \tag{2.27}$$

$$f^v = \frac{2\mu}{\rho_f}\frac{\partial v_x}{\partial y}\bigg|_{w/2} \tag{2.28}$$

2.2.3 Flow cases - fully laminar and turbulent flow

To calculate the friction force and momentum correction factor, there must be an assumption about the shape of the velocity profile. In this section, we will examine the cases of fully developed laminar and turbulent flow through parallel plates.

Fully developed laminar flow

In fully developed laminar flow through parallel plates, the velocity profile is parabolic, such that

$$v_x = v_{max}\left(1 - \left(\frac{2y}{w}\right)^2\right), \quad \{-\frac{w}{2} \le y \le \frac{w}{2}\}, \quad \overline{v_x} = \frac{2}{3}v_{max} \tag{2.29}$$

Thus, we can calculate the momentum correction factor and the dissipation force.

$$\alpha = \frac{6}{5} \tag{2.30}$$

$$f^v = -\frac{12\mu}{\rho_f}\frac{q}{w^2} \tag{2.31}$$

In laminar flow, we expect that the friction term will take the general form of (2.31) with respect to the flow and geometry parameters, but that the numerical coefficient will change depending on the velocity profile. We therefore introduce the viscous friction coefficient, β, where

$$f^v = -\beta\frac{\mu}{\rho_f}\frac{q}{w^2} \tag{2.32}$$

$$\beta = -2\frac{w^2}{q}\frac{\partial v_x}{\partial y}\bigg|_{w/2} \tag{2.33}$$

in which $\beta = 12$ for the aforementioned parabolic velocity profile. For apertures that are not uniform and flow that is not fully-developed, the parameters α and β would not be constants and would instead take a general form $\alpha = \alpha(Re, \nabla w)$, $\beta = \beta(Re, \nabla w)$. It is not possible to derive an analytical expression for α and β, as the velocity profiles are in general a function of both the upstream and downstream flow conditions and geometries. Therefore we will assume that all laminar flow follows a parabolic velocity profile and use constant coefficients and check the validity of that assumption later.

Fully turbulent flow

Turbulent flow is a phenomenon that occurs at high Reynolds numbers in which random violent eddies form and dissipate due to the instability of the velocity profile to minor perturbations at high flow rates. This is a different phenomenon from the fundamentally two-dimensional behaviour of stable eddy formation around surface asperities, and is instead a stochastic and chaotic phenomenon. In pipe flow, the laminar regime tends to break down around $Re \approx 2 \times 10^3$, which equates to an equivalent Reynolds number of 1400 based on the equivalent hydraulic diameter of a fracture [26].

For turbulent flow, we can apply the same derivation to the time-averaged Navier-Stokes equations [44]. Repeating the non-dimensionalization, we again recover that $\frac{\partial p}{\partial y} = 0$. The equation governing the conservation of momentum therefore becomes

$$\frac{\partial q'}{\partial t} + \frac{\partial}{\partial x}\left(\alpha \frac{q'^2}{w}\right) = -\frac{w}{\rho_f}\frac{\partial p'}{\partial x} + f^v - f^t \tag{2.34}$$

$$f^t = \int_{-w/2}^{w/2} \left(\frac{\partial}{\partial x}(\mathfrak{v}_x^2) + \frac{\partial}{\partial y}(\mathfrak{v}_x \mathfrak{v}_y)\right) dy \tag{2.35}$$

in which i' denotes the time averaged flow variables, and $\mathfrak{i}$ denotes the random fluctuations of the flow variables. f^v now represents the momentum dissipation due to viscous forces, while f^t represents the momentum dissipation due to turbulent eddy motion. The turbulent force can be simplified using the no-slip boundary condition, (2.10), such that

$$f^t = \frac{\partial}{\partial x}\left(\int_{-w/2}^{w/2} (\mathfrak{v}_x^2) dy\right) \tag{2.36}$$

It is difficult to say anything more about the velocity fluctuations from an analytical standpoint. They cannot be evaluated without an empirical correlation or full CFD solution. Fractures and ducts share similarities in their geometry, although fractures contain much higher surface roughness and aperture variations. For simplicity, we will assume that fractures and ducts have similar behaviour, which will let us combine the viscous and turbulent forces into a single dissipation force and adopt the form of the Darcy-Weisbach equation:

$$f = f^v + f^t = \frac{1}{2}\frac{f_D}{w^2} q^2 \tag{2.37}$$

in which f_D is the Darcy friction factor. We can now make use of the many empirical friction models that have been proposed over the years to capture friction losses in turbulent duct

flow. Here we will propose adopting the phenomenological Colebrook-White equation for duct flow [45],

$$\frac{1}{\sqrt{f_D}} = -2\log\left(\frac{\epsilon}{3.7D_h} + \frac{2.51}{Re\sqrt{f_D}}\right) \quad \text{if } Re > 4000 \tag{2.38}$$

in which the hydraulic diameter, D_h, can be expressed in terms of the aperture as $D_h = 2w$ and linearly interpolating the friction factor in the transitional regime ($2000 < Re < 4000$). More complex friction laws which more accurately capture the complete transition between laminar and turbulent flow, for example the Yang-Dou model [46], could easily be adopted instead. The Colebrook-White equation is based on steady-state turbulent flow through pipes and is suggested for simplicity. It should be replaced with a more appropriate model in cases where unsteady turbulent flow is important.

Lastly, to calculate the momentum correction factor, α, the velocity profile in turbulent flow may be roughly approximated using a power law expression [44]:

$$v'_x \approx \frac{8}{7}\overline{v}'_x \left(1 - \frac{2y}{w}\right)^{\frac{1}{7}}, \{0 \leq y \leq \frac{w}{2}\} \tag{2.39}$$

This approximate profile fails close to the walls as the velocity gradient is asymptotic, but since we have incorporated the viscous force into the Darcy-Weisbach friction force, the approximate profile is sufficient to calculate the momentum correction factor. We find that $\alpha = \frac{64}{63}$ — the plug flow velocity profile characteristic of turbulent flow results in a momentum correction factor much closer to 1 than the parabolic laminar profile.

2.2.4 General case

The governing set of equations in fracture flow may be summarized as follows:

$$\frac{\partial w}{\partial t} + \frac{\partial q}{\partial x} = 0 \tag{2.40}$$

$$\frac{\partial q}{\partial t} + \frac{\partial}{\partial x}\left(\alpha\frac{q^2}{w}\right) = -\frac{w}{\rho_f}\frac{\partial p}{\partial x} - \frac{1}{2}\frac{f_D}{w^2}q|q| \tag{2.41}$$

$$\alpha = \alpha(Re, \nabla w) \approx \begin{cases} \frac{6}{5} & \text{if } Re < 2000 \\ \frac{64}{63} & \text{if } Re > 4000 \end{cases} \tag{2.42}$$

$$f_D = \begin{cases} \frac{2\beta}{Re}, \quad \beta = \beta(Re, \nabla w) \approx 12 & \text{if } Re < 2000 \\ \frac{1}{\sqrt{f_D}} = -2\log(\frac{\epsilon}{7.4w} + \frac{2.51}{Re\sqrt{f_D}}) & \text{if } Re > 4000 \end{cases} \tag{2.43}$$

$$Re = \frac{\rho_f \overline{v_x} w}{\mu} = \frac{q}{\nu} \tag{2.44}$$

The model summarized in this section will be refered to as the GG22 Fracture Flow Model [41]. In general, one additional governing equation (typically the equilibrium of forces) is required to describe the relationship between the deformation of the aperture and the fluid pressure, $w = w(p)$. The GG22 model is more complex than Poiseuille flow, as it is

described by two fields instead of one and requires solving a second non-linear differential equation. However, it does not come with the same computational burden as the full Navier-Stokes equations, as the assumptions about the behaviour over the cross section allow us to reduce the fracture volumes to fracture planes.

2.2.5 Extension to planes

Consider the case of a two-dimensional plane with deformable aperture which lies upon the $x-z$ cartesian plane. The same set of assumptions can be made and the same derivation can be followed for a domain in which $v_z \neq 0$ to derive a planar version of the general GG22 equations. The velocity components are non-dimensionalized according to $v_x = Vv_x^*, v_z = Vv_z^*$ and $v_y = Uv_y^*$. The coordinate systems are non-dimensionalized according to $x = \lambda x^*, z = \lambda z^*$ and $y = \frac{\overline{w}}{2}y^*$, in which $\lambda = \frac{\overline{w}}{2}\frac{V}{U}$. Following the same procedure as before, the governing set of equations is given by

$$\frac{\partial w}{\partial t} + \nabla \cdot \boldsymbol{q} = 0 \tag{2.45}$$

$$\frac{\partial \boldsymbol{q}}{\partial t} + \nabla \cdot \left(\frac{\boldsymbol{\alpha}}{w} \cdot \boldsymbol{q}\boldsymbol{q}\right) = -\frac{w}{\rho_f}\nabla p - \frac{1}{2}\frac{f_D}{w^2}\{\boldsymbol{q}\} \cdot |\{\boldsymbol{q}\}| \tag{2.46}$$

$$Re = \frac{||\boldsymbol{q}||}{\nu} \tag{2.47}$$

$$\boldsymbol{q} = \begin{bmatrix} q_x \\ q_z \end{bmatrix} \tag{2.48}$$

$$\{\boldsymbol{q}\} = \begin{bmatrix} q_x & 0 \\ 0 & q_z \end{bmatrix} \tag{2.49}$$

$$\boldsymbol{\alpha} = \begin{bmatrix} \alpha_x & 0 \\ 0 & \alpha_z \end{bmatrix} \tag{2.50}$$

2.3 Physical Interpretations and Implications of the Model

In this section, the physical interpretation and implications of each term in the new formulation will be explored, the cases under which we can recover Poiseuille and Forchheimer flows will be examined, and conservation of energy in the fluid will be discussed.

2.3.1 Physical interpretation of each term

Consider the derived equation for conservation of momentum in fully developed laminar flow, which can be expanded and rearranged as

$$\frac{\partial p}{\partial x} = -\frac{\rho_f}{w}\frac{\partial q}{\partial t} - \frac{\rho_f q^2}{w^2}\frac{\partial \alpha}{\partial x} - \alpha\frac{2\rho_f q}{w^2}\frac{\partial q}{\partial x} + \alpha\frac{\rho_f q^2}{w^3}\frac{\partial w}{\partial x} - \beta\mu\frac{q}{w^3} \tag{2.51}$$

Let us examine the physical interpretation of each term in the equation of motion:

Term 1 *Transient flux term,* $-\frac{\rho_f}{w}\frac{\partial q}{\partial t}$

This term relates a component of the pressure gradient to changes in fluid flux over time. If the fluid flux is not constant over time, then there is an additional component to the pressure gradient that is required to overcome the fluid inertia and change the fluid flux. This temporal component of the flux is not captured by Poiseuille flow, which assumes steady state flow.

Term 2 *Velocity profile term,* $-\frac{\rho_f q^2}{w^2}\frac{\partial \alpha}{\partial x}$

This term relates a component of the pressure gradient to the change in the velocity profile along the length of the fracture and is associated with inertial convective forces. In fully-developed parallel plate flow, the velocity profile does not change along the length of the fracture, and so this term disappears. Factored by q^2, this term becomes more important in high Re flows, and less important in viscous flows. If α is increasing along the fracture, it indicates that the velocity profile is becoming sharper - i.e the maximum velocity is increasing relative to the average velocity. If α is decreasing along the fracture, then the velocity profile is becoming blunter — moving towards a plug flow profile with the maximum velocity decreasing relative to the average velocity. The negative sign indicates that an increase in maximum velocity results in a decrease in pressure, and a decrease in the maximum velocity results in an increase of pressure. This term therefore enables a transfer of energy from kinetic energy in the form of velocity to potential energy in the form of pressure (further discussion on the conservation of energy in Section 2.3.3).

Term 3 *Spatial flux/moving boundary term,* $-\alpha\frac{2\rho_f q}{w^2}\frac{\partial q}{\partial x}$

This term relates a component of the pressure gradient to the flux gradient and is associated with convective forces. This term determines how much the momentum must change due to expansion and contraction of the fracture aperture. From continuity, this term can also be written as

$$-\alpha\frac{2\rho_f q}{w^2}\frac{\partial q}{\partial x} = \alpha\frac{2\rho_f q}{w^2}\frac{\partial w}{\partial t} \tag{2.52}$$

such that if the aperture exists in a perfectly rigid and static domain ($\dot{w} = 0$), the flux must be constant along the length of the fracture and this term disappears.

Term 4 *Aperture gradient term,* $\alpha\frac{\rho_f q^2}{w^3}\frac{\partial w}{\partial x}$

This term relates a component of the pressure gradient to the aperture gradient, as the change in aperture will create a change in velocity. This term means that the formulation is not restricted to the assumption of parallel plate flows and is a major improvement over Poiseuille flow. Factored by q^2, this term becomes more important in high Re flows, and less important in viscous flows. Like the velocity profile term, this term enables a transfer between kinetic energy and fluid pressure.

The aperture term is interesting because it allows for a positive pressure gradient to develop in a diverging flow field (aperture increasing in the direction of flow) in which friction losses are small. Such behaviour is impossible under the Poiseuille flow model but can be shown to occur in reality at even moderate Reynolds number flows in varying aperture, such as

those considered later in Section 2.4.3. Figure 2.2 plots the ratio between the GG22 and Poiseuille flow pressure gradients for steady-state laminar flow between rigid non-parallel plates as a function of aperture gradient and Reynolds number:

$$\frac{\nabla p_{GG22}}{\nabla p_{PF}} = \frac{\alpha \frac{\partial w}{\partial x} - \frac{\beta}{Re}}{\frac{-12}{Re}}, \quad \alpha = 1.2, \quad \beta = 12 \tag{2.53}$$

A ratio of 1 indicates that the pressure gradients of both models are identical, while deviations from 1 indicate the relative change caused by the aperture gradient term in the GG22 model. The zero contour indicates where the GG22 model predicts no change in pressure, because pressure increases due to slowing of the fluid at the same rate that pressure is dissipated by friction. The negative contours at positive aperture gradient and high Reynolds number indicate the region in which such positive pressure gradients would be expected.

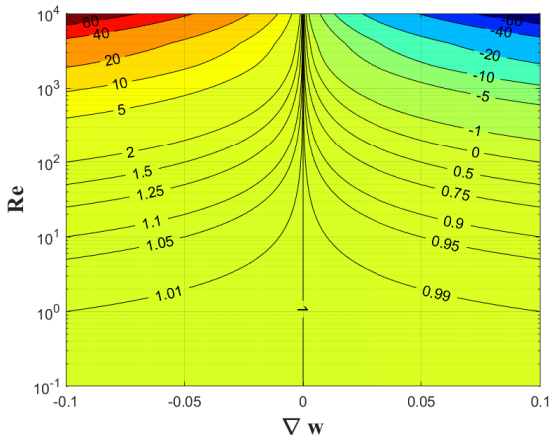

Figure 2.2: Ratio of gradients between the Poiseuille flow and GG22 models assuming steady laminar flow conditions in a rigid aperture with constant $\alpha = 1.2$ and $\beta = 12$. Ratios not equal to one indicate changes in the pressure gradient due to deviations in aperture.

Term 5 *Viscous friction term,* $-\beta\mu\frac{q}{w^3}$

This term relates a component of the pressure gradient to viscous friction dissipation and is the only term to appear in the Poiseuille flow formulation. In steady-state laminar parallel plate flow, all terms except this one disappear and the Poiseuille flow formulation is recovered. The negative sign indicates that, in the absence of other factors, fluid flows in the opposite direction of the pressure gradient. Viscous forces do work on the fluid, dissipating the potential energy that exists in the form of fluid pressure.

2.3.2 Quasi-steady flow conditions

In this section, we will consider what happens to the GG22 model under steady flow conditions and show that previously proposed flow models exist within the solution space of the GG22 model.

Poiseuille flow

Consider the case of steady laminar flow through rigid parallel plates, such that $\dot{q} = 0, \dot{w} = 0, q_{,x} = 0, w_{,x} = 0$, and $\alpha_{,x} = 0$. In this case, we can reduce the governing equations (2.40) and (2.41) to

$$-\frac{w}{\rho_f}\frac{\partial p}{\partial x} - \frac{12\mu}{\rho_f}\frac{q}{w^2} = 0 \tag{2.54}$$

which we can rearrange to find

$$\frac{\partial p}{\partial x} = -\frac{12\mu}{w^3}q \tag{2.55}$$

thus recovering the Poiseuille flow constitutive relationship between pressure and fluid flux. Therefore, we can conclude that Poiseuille flow exists within the solution space of the GG22 model.

Forchheimer Flow

Forchheimer flow is a non-linear extension to Darcy flow through porous media [39]. In fracture flow, this relationship takes the form

$$\frac{\partial p}{\partial x} = -\frac{12\mu}{w^3}q + \gamma q^2 \tag{2.56}$$

in which γ is an empirical coefficient. While Forchheimer flow does not see much use in modern models, there have been efforts to determine the value of the empirical coefficient γ for fracture flow [35, 36]. Forchheimer flow offers the advantage of being a two-field model $(u - p)$, as opposed to the three-fields required by the GG22 model $(u - q - p)$. In this section, we will recast the GG22 model as a two-field model to derive an analytical expression for the previously empirical coefficient.

If we assume that the flow is steady, $\dot{q} = 0$, and the aperture is rigid, $\dot{w} = 0, \frac{\partial q}{\partial x} = 0$, then we can express the pressure gradient as

$$\frac{\partial p}{\partial x} = -\frac{12\mu}{w^3}q + \left(\alpha\frac{\rho_f}{w^3}\frac{\partial w}{\partial x} - \frac{\rho_f}{w^2}\frac{\partial \alpha}{\partial x}\right)q^2 \tag{2.57}$$

Comparing (2.56) and (2.57), the empirical coefficient can be expressed as

$$\gamma = \alpha\frac{\rho_f}{w^3}\frac{\partial w}{\partial x} - \frac{\rho_f}{w^2}\frac{\partial \alpha}{\partial x} \tag{2.58}$$

so that the constitutive relationship between pressure and fluid flux can be expressed as

$$\frac{\partial p}{\partial x} = -\frac{12\mu}{w^3}(1 - F_0)q \tag{2.59}$$

$$F_0 = \left(\alpha\frac{\rho_f}{12\mu}\frac{\partial w}{\partial x} - \frac{\rho_f w}{12\mu}\frac{\partial \alpha}{\partial x}\right)q \tag{2.60}$$

in which F_0 is the nonlinear coefficient known as the Forchheimer number. The Forchheimer number is a function of the flow rate, q, the fracture geometry, $w, \nabla w$, and the distribution of fluid velocity across the aperture, α. As the fluid flux goes to zero, so too does the Forchheimer number, and the standard Poiseuille flow formulation is recovered.

Forchheimer flow offers the advantage of being a two-field model, but this advantage is accompanied by physical restrictions, albeit fewer restrictions than Poiseuille flow. This formulation for Forchheimer flow is only applicable to rigid fractures and quasi-steady state flow conditions.

2.3.3 Conservation of energy

Consider Bernoulli's principle between points A and B along a rigid fracture of varying aperture in steady-state laminar flow. The total energy of the fluid at each point is the sum of potential energy and kinetic energy, which are functions of the fluid pressure and fluid velocity, respectively. The points are assumed to be at the same elevation. We will integrate over the cross sections A and B to examine the conservation of energy of the bulk fluid. We can therefore state the conservation of energy over the cross section as

$$\frac{1}{2}\rho_f \int_{-w_A/2}^{w_A/2} v^2 dy + \int_{-w_A/2}^{w_A/2} p dy = \frac{1}{2}\rho_f \int_{-w_B/2}^{w_B/2} v^2 dy + \int_{-w_A/2}^{w_A/2} p dy + f \tag{2.61}$$

in which $f > 0$ is the energy dissipated by viscous forces. Assuming the velocity profile does not change between cross sections A and B (constant α), we can rearrange this expression to determine that the pressure difference between any two points in a fracture is equal to the energy dissipated by viscous friction, plus an additional transfer of energy between kinetic energy and fluid pressure.

$$\Delta p = p_B - p_A = \frac{1}{2}\alpha\rho_f q^2 \left(\frac{1}{w_A^2} - \frac{1}{w_B^2}\right) - f \tag{2.62}$$

When Poiseuille flow is adopted, we can integrate the constitutive equation between points A and B to find that the pressure difference is

$$\Delta p = \left(p_A + \int_A^B \frac{\partial p}{\partial x} dx\right) - p_A \tag{2.63}$$

$$\Delta p = -12\mu q \xi, \quad \xi = \int_A^B w^{-3} dx > 0 \tag{2.64}$$

Comparing the terms in (2.62) and (2.64), it is clear that Poiseuille flow only contains a single term to describe the dissipation by viscous friction, such that $f = 12\mu q\xi$. There is no additional term to transfer energy between kinetic and potential energy, and therefore the Poiseuille flow constitutive model does not conserve energy when applied to flow through varying aperture fields. The lost energy may be small if the difference in aperture is small, but it is still non-zero.

Next, consider the case of adopting the GG22 model, assuming constant α and β. The pressure difference between any two points can be determined as

$$\Delta p = \left(p_A + \int_A^B \frac{\partial p}{\partial x} dx \right) - p_A \tag{2.65}$$

$$\Delta p = \alpha \rho_f q^2 \xi_2 - \beta \mu q \xi \tag{2.66}$$

$$\xi_2 = \int_A^B w^{-3} \frac{\partial w}{\partial x} dx = \frac{1}{2} \left(\frac{1}{w_A^2} - \frac{1}{w_B^2} \right) \tag{2.67}$$

$$\Delta p = \alpha \rho_f q^2 \frac{1}{2} \left(\frac{1}{w_A^2} - \frac{1}{w_B^2} \right) - \beta \mu q \xi \tag{2.68}$$

Comparing (2.62) and (2.68), it can be observed that the GG22 model contains the additional term to transfer energy between kinetic energy and fluid pressure. Therefore, the GG22 model conserves energy in non-uniform aperture fields, while the Poiseuille flow model does not. The assumption of constant α is made to simplify the presentation of the analysis, and energy is still conserved in the case of non-constant α.

2.4 Comparisons of Navier-Stokes, GG22, and Poiseuille Flow Models

In this section, we will examine the solutions of the full Navier-Stokes, the GG22, and the Poiseuille flow models in three different simple flow problems in which closed-form solutions to the Poiseuille and GG22 models are readily derived. These comparisons will demonstrate the shortcomings of the Poiseuille flow model and quantitatively measure the error in adopting the GG22 and Poiseuille flow models.

2.4.1 Transient fluid flow between parallel plates

Consider the flow through a channel of length L that is defined by rigid static parallel plates with aperture w_0, as illustrated in Figure 2.3. The pressure at the outlet is fixed at $p_{out} = p_0$, while the pressure at the inlet oscillates such that $p_{in} = p_0 + \sin \Omega t$. The resulting flow rate between the inlet and outlet, q, is then a function of time. This example demonstrates that the transient inertial behaviour of the fluid is important.

Assuming that the flow is laminar, this problem may be solved analytically for all three flow models. The solution is expressed in terms of the dimensionless flux, q^*, defined as

$$q^*(t) = \frac{12 \mu L}{w_0^3} q(t) \tag{2.69}$$

The solution to the Navier-Stokes model and the GG22 model are identical and given by

$$q^* = \frac{-\phi}{\Omega^2 + \phi^2} \left(\Omega \cos \Omega t - \phi \sin \Omega t - \Omega e^{-\phi t} \right), \quad \phi = \frac{12 \mu}{\rho_f w_0^2} \tag{2.70}$$

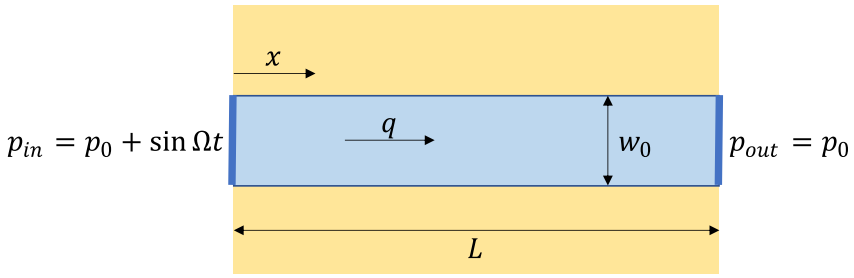

Figure 2.3: Domain for oscillating pressure inlet condition between parallel plates

in which ϕ is the fundamental frequency of the fluid-fracture system. The Poiseuille flow solution is given by

$$q^* = \sin \Omega t \tag{2.71}$$

The Navier-Stokes and GG22 solution is a function of the fundamental frequency of the fluid, ϕ, and the excitation frequency, Ω. The Poiseuille flow solution, as it assumes quasi-steady state conditions, is only a function of the excitation frequency.

The solutions for different ratios of excitation frequency compared to natural frequency are illustrated in Figure 2.4. When the excitation frequency is small compared to the fundamental frequency ($\Omega << \phi$), the GG22 and Navier-Stokes solutions converge to the quasi-steady state Poiseuille flow solution and the flow rate changes synchronously with the inlet pressure. When the excitation frequency is large compared to the fundamental frequency ($\Omega >> \phi$), the inertial forces are large and very little flow occurs. When the excitation and fundamental frequency are similar ($\Omega \sim \phi$), there is strong coupling behaviour in the response of the fluid which affects the magnitude of the flow rate and causes the flow rate to lag the boundary condition.

The expected range of the fundamental frequency ϕ is large due to the variability of aperture in rock mass systems. Assuming the properties of water, ϕ ranges from $\sim$12 MHz for apertures of 1 μm to 0.12 Hz for apertures of 1 cm. Consider for example the range of excitation frequencies associated with seismic waves, ranging from 10-150 Hz [4]. Coupling effects are thus expected in fractures with apertures greater than 100 μm ($\phi = 1200Hz, \Omega/\phi = 0.125$). This example demonstrates how transient inertial fluid forces can affect the flow rate, and how the Poiseuille flow model is incapable of capturing this behaviour.

2.4.2 Transient fluid flow between oscillating parallel plates

Consider the flow through a submerged channel of length $2L$ in which the aperture is defined by parallel plates that oscillate at a fixed amplitude, A, and frequency, Ω, such that $w = w_0(1 + A \sin \Omega t)$, as illustrated in Figure 2.5. The pressure at the outlets is fixed at $p_{out} = p_0$, and the flux q must be zero at the center of the channel due to symmetry. This problem captures both inertial transient and inertial convective effects since the flux is not constant along the length of the domain.

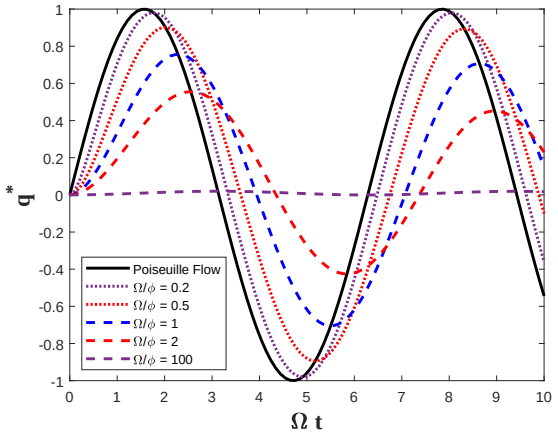

Figure 2.4: Dimensionless flow rate through parallel plates with oscillating inlet pressure

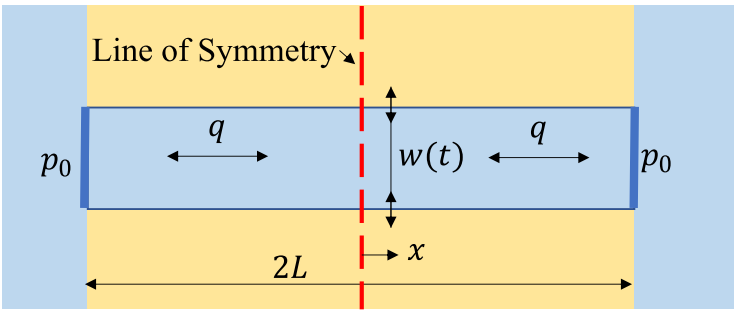

Figure 2.5: Domain for flow in and out of submerged channel with oscillating parallel plates

While the GG22 and Poiseuille flow solutions may be solved analytically by assuming laminar flow, the Navier-Stokes solution for this problem is non-trivial both analytically and numerically due to the moving boundaries. This example will therefore only compare the results of the GG22 and Poiseuille flow solutions.

For both flow models, the fluid flux is given by the continuity equation, such that

$$q = -\dot{w}x \tag{2.72}$$

The pressure profile along the channel for the Poiseuille flow solution is

$$p = p_0 + \frac{12\mu\dot{w}}{w^3}\frac{L^2}{2}\left[\left(\frac{x}{L}\right)^2 - 1\right] \tag{2.73}$$

The pressure profile along the channel for the GG22 solution, assuming constant α and β, is

$$p = p_0 + \left(\rho_f\left(\frac{\ddot{w}}{w} - 2\alpha\left(\frac{\dot{w}}{w}\right)^2\right) + \frac{\beta\mu}{w^3}\dot{w}\right)\frac{L^2}{2}\left[\left(\frac{x}{L}\right)^2 - 1\right] \tag{2.74}$$

To compare the models, we can examine the dimensionless pressure at the centerline ($x = 0$),

$$p^* = \frac{p(0,t) - p_0}{6\Omega\mu}\left(\frac{w_0}{L}\right)^2 \tag{2.75}$$

The dimensionless pressure at the centerline, p^*, for each model can then be simplified to

$$\text{Poiseuille} \quad p^* = \frac{-A\cos\Omega t}{(1 + A\sin\Omega t)^3} \tag{2.76}$$

$$\text{GG22} \quad p^* = \frac{\Omega}{\phi}\left(\frac{A\sin\Omega t}{1 + A\sin\Omega t} + 2\alpha\left(\frac{A\cos\Omega t}{1 + A\sin\Omega t}\right)^2\right) - \frac{A\cos\Omega t}{(1 + A\sin\Omega t)^3}, \quad \phi = \frac{12\mu}{\rho_f w_0^2} \tag{2.77}$$

The dimensionless pressure at the centerline for an amplitude of $A = 0.25$ is plotted as a function of time in Figure 2.6. Changing the amplitude of the oscillations increases the peak pressures but does not otherwise change the behaviour of the solutions.

First consider the behaviour of the quasi-steady Poiseuille flow model. In the Poiseuille flow model, flow only ever moves due to the presence of a pressure gradient. Since the conservation of mass forces fluid in and out of the channel, the pressure gradient develops to accommodate this flow. When the aperture reaches a peak or a trough, there is a zero-pressure gradient at that instant as the fluid momentarily stops before reversing direction. The time history for pressure incurs a phase shift towards the aperture troughs because the smaller apertures require larger gradients to move the fluid.

Next, consider the behaviour of the GG22 model which depends on the fundamental frequency of the fluid, ϕ. When the oscillation frequency is small compared to the fundamental

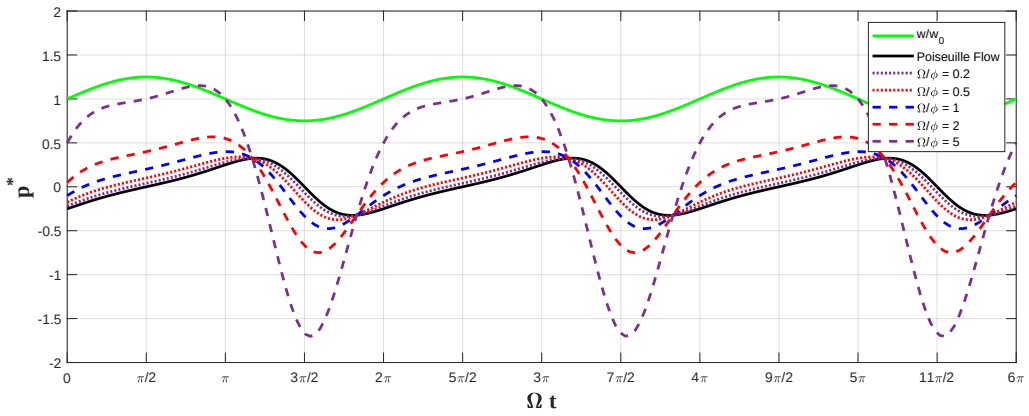

Figure 2.6: Dimensionless pressure at the centerline of parallel plates oscillating with an amplitude of $A = 0.25$.

frequency ($\Omega < \phi$), the behaviour trends towards the quasi-static Poiseuille solution. When the oscillation frequency is large compared to the fundamental frequency ($\Omega > \phi$), inertial effects dominate the response and the solution deviates significantly from Poiseuille flow. Conservation of mass forces fluid in and out of the channel very quickly, but the inertial forces try to resist this motion. The pressure gradient thus becomes synchronized with the aperture oscillations but in the opposite direction to the Poiseuille flow gradient. When fluid is being forced into the channel, the pressure increases at the centerline, to try and push the fluid back out. When fluid is being forced out of the channel, the pressure decreases at the centerline, forming a large negative backpressure which sucks the fluid back in.

This example illustrates the complex inertial convective behaviours that arise in problems in which fracture aperture varies in time and which the Poiseuille flow model is incapable of capturing.

2.4.3 Steady state fluid flow in channels of varying aperture

Consider the steady state flow through a rigid fracture of varying aperture, as shown in Figure 2.7. The domain is defined by a periodic aperture, such that $w(x) = w_0 \left(1 - \varepsilon \cos\left(\frac{2\pi x}{\lambda w_0}\right)\right)$, in which $0 \leq \varepsilon < 1$ is the characteristic amplitude, and λ is the characteristic wavelength relative to the aperture. The sinusoidal aperture adopted here represents an anti-mated fracture and is not necessarily representative of natural fracture geometry. It is instead adopted due to its convenient mathematical properties. Fluid flows through the fracture at a constant rate of $\overline{q}$. The pressure at the outlet is fixed at a constant pressure $\overline{p}$.

The GG22 and Poiseuille flow solutions can be solved analytically. The solution is expressed in terms of the dimensionless pressure distribution, p^*, as a function of the non-

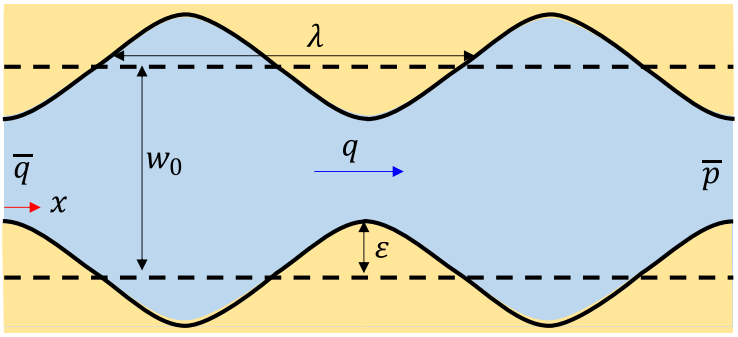

Figure 2.7: Domain for steady state flow through a fracture of varying aperture

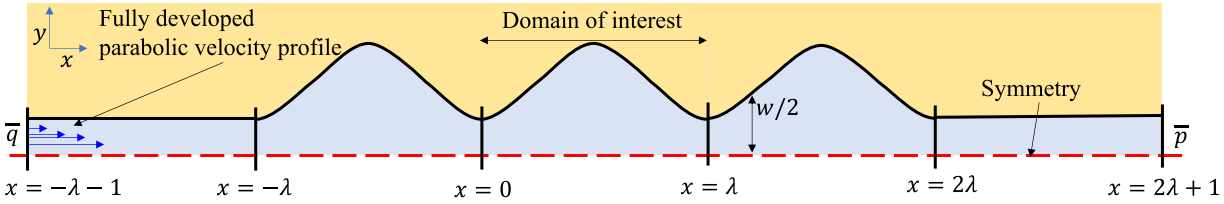

Figure 2.8: Computational Domain for CFD simulation of steady-state flow through a fracture of varying aperture.

dimensionalized coordinate $\lambda x^* = x$.

$$p^* = \frac{w_0^2}{\rho_f \overline{q}^2}(p - \overline{p}) = -\xi^*(1) + \xi^*(x^*), \quad 0 \le x^* \le 1 \tag{2.78}$$

$$\xi(x^*) = \int_0^{x^*} \frac{\partial p^*}{\partial x^*} dx^* \tag{2.79}$$

$$\text{Poiseuille} \quad \frac{\partial p^*}{\partial x^*} = -\lambda \frac{12}{Re} \frac{1}{(1 - \varepsilon \cos(2\pi x^*))^3} \tag{2.80}$$

$$\text{GG22} \quad \frac{\partial p^*}{\partial x^*} = 2\pi\alpha\varepsilon \frac{\sin(2\pi x^*)}{(1 - \varepsilon \cos(2\pi x^*))^3} - \lambda \frac{12}{Re} \frac{1}{(1 - \varepsilon \cos(2\pi x^*))^3} \tag{2.81}$$

The solution to the Navier-Stokes equations for this problem is approximated using ANSYS FLUENT CFD software. The computational domain is illustrated in Figure 2.8. Pressure is prescribed at the outlet while the fluid flux is prescribed at the inlet using a fully developed parabolic velocity profile. The computational domain contains an inlet and outlet section with constant aperture. Symmetry is assumed along the centerline of the model. The range of tested Reynolds number is limited to ensure that the flow remains within the laminar regime, such that unsymmetric phenomena like turbulence and vortex shedding are not expected. The interior of the domain is three wavelengths long and whose sinusoidal aperture is defined by piecewise line segments at a resolution of $\lambda/60$. The domain of interest is the central region $0 \le x \le \lambda$, as illustrated in Figure 2.8.

To compare the two-dimensional pressure field obtained from CFD with the one-dimensional models, the average pressure over the aperture for a given position, x, in the two-dimensional model is computed at 61 evenly spaced cross sections along the domain of interest. The

gradient of the extracted average pressures is computed using central differencing, with a second order forward and backward differencing scheme used at each end point. The error between the full Navier-Stokes solution and the reduced dimension models, ϵ, is calculated as

$$\epsilon_i = \sqrt{\frac{\int_0^1 \left(\frac{\partial p^*_{NS}}{\partial x^*} - \frac{\partial p^*_i}{\partial x^*}\right)^2 dx^*}{\int_0^1 \left(\frac{-12\lambda}{Re(1-\varepsilon)^3}\right)^2 dx^*}} \tag{2.82}$$

in which $\frac{\partial p^*_{NS}}{\partial x^*}$ is the gradient of the average pressure from the full CFD model, and $\frac{\partial p^*_i}{\partial x^*}$ from either reduced dimension model. The error is normalized by the pressure gradient through a parallel plate channel of width $w = 1 - \varepsilon$.

The CFD simulations were run using the 3rd order MUSCL flux interpolation scheme and a second order pressure interpolation scheme. The CFD simulations were solved using ANSYS FLUENT's pressure-based coupled solver. A coarser mesh was applied to the inlet and outlet sections while a fine structured mesh was applied to the sinusoidal sections between $-\lambda \leq x \leq 2\lambda$. The mesh was refined for each combination of ε and λ at $Re = 0.01$ until the outputted average pressures converged to a relative change $< 10^{-4}$ from the previous mesh. The number of cells ranged from 8×10^4 in shortest domains, up to 5×10^5 in the longest domains.

The CFD model was run for amplitudes ranging from $\varepsilon = 0$ to $\varepsilon = 0.7$, wavelengths from $\lambda = 1$ to $\lambda = 20$, and Reynolds numbers ranging from $Re = 0.01$ to $Re = 1000$. All cases converged to a steady-state solution. While some cases displayed stable eddy formation, no cases displayed any indication of vortex shedding or developing turbulence. Figure 2.9 shows a selection of pressure contours throughout the fractures in which the GG22 model performs well and performs poorly. Figure 2.10 shows the corresponding transverse velocity contours and streamlines within the fractures. As seen in figures 2.9 and 2.10, the reduced dimension models perform well in cases where the transverse pressure gradients and transverse velocities are small. The reduced dimension models perform poorly in cases where the transverse pressure gradients are not negligible, the transverse velocities are not small, and fundamentally two-dimensional phenomena are observed. Such two-dimensional phenomena include the development of eddies within the aperture peaks, and the longitudinal velocity maintaining its speed as it exits the narrowed aperture regions, demonstrating behaviour akin to a jet rather than fracture flow.

Figure 2.11 shows the distribution of the pressure gradient over a selection of wavelengths and Reynolds number at $\varepsilon = 0.3$. Lastly, Figure 2.12 shows the error curves as a function of Reynolds number for tested wavelengths and amplitudes, while Figure 2.13 shows the relative improvement in error between the GG22 and Poiseuille flow models.

The case of $\varepsilon = 0$ corresponds to parallel plates, which both the Poiseuille and GG22 models capture exactly. This case provides an estimate of the error that results from: the convergence of the non-linear CFD solver, the CFD mesh, the resolution of the extracted average pressure curve, and the calculation of the numerical gradient. This error of 10^{-4} is at least an order of magnitude smaller than the error observed in any of the other cases,

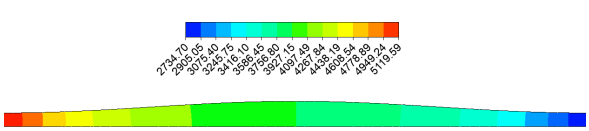

(a) $\varepsilon = 0.3, \lambda = 15, Re = 0.1$

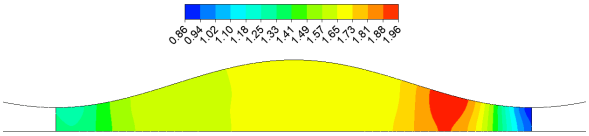

(b) $\varepsilon = 0.5, \lambda = 5, Re = 500$

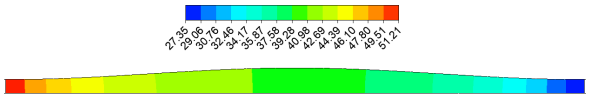

(c) $\varepsilon = 0.3, \lambda = 15, Re = 10$

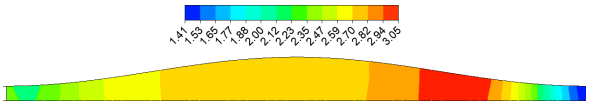

(d) $\varepsilon = 0.5, \lambda = 10, Re = 500$

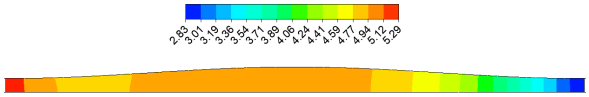

(e) $\varepsilon = 0.3, \lambda = 15, Re = 100$

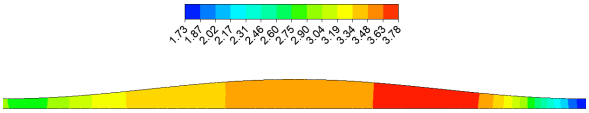

(f) $\varepsilon = 0.5, \lambda = 15, Re = 500$

Figure 2.9: Examples of pressure contours from the CFD cases. Figures 2.9a and 2.9c are examples where the GG22 model performs well and the pressure gradient is negative throughout the fracture. Figure 2.9e is an example where the GG22 model performs well, but a positive pressure gradient develops due to expansion of the fracture and slowing of the fluid velocity. Figures 2.9b, 2.9d, 2.9f are examples where the GG22 model performs poorly, due to significant transverse pressure gradients and positive longitudinal pressure gradients associated with the formation of eddies.

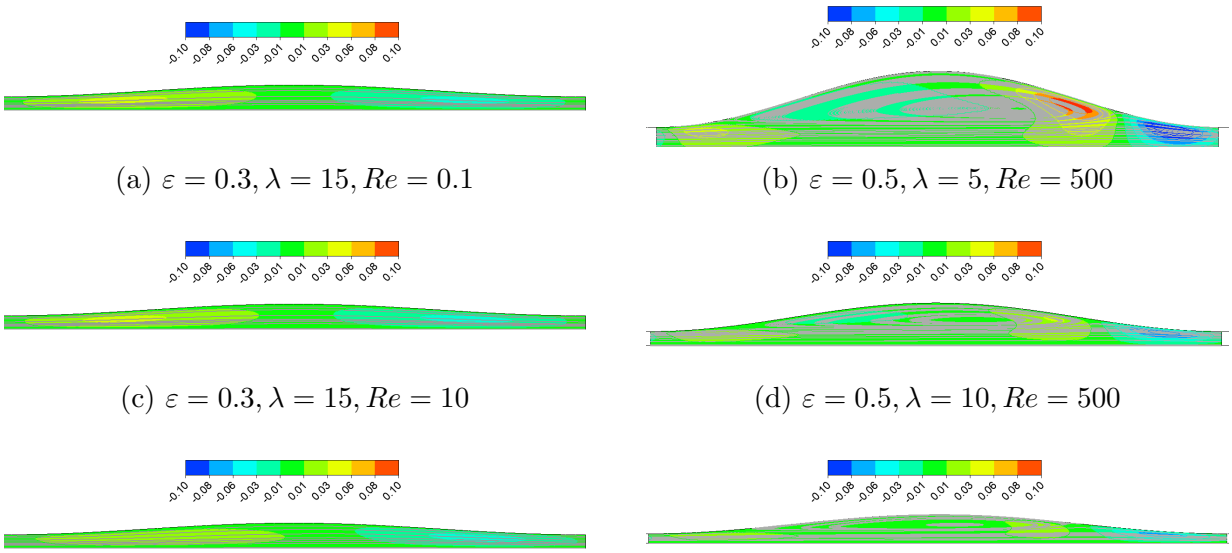

(a) $\varepsilon = 0.3, \lambda = 15, Re = 0.1$

(b) $\varepsilon = 0.5, \lambda = 5, Re = 500$

(c) $\varepsilon = 0.3, \lambda = 15, Re = 10$

(d) $\varepsilon = 0.5, \lambda = 10, Re = 500$

(e) $\varepsilon = 0.3, \lambda = 15, Re = 100$

(f) $\varepsilon = 0.5, \lambda = 15, Re = 500$

Figure 2.10: Examples of transverse velocities and streamlines from the CFD cases. Figures 2.10a, 2.10c, and 2.10e are examples where the GG22 model performs well. Despite the different pressure contours illustrated in Figure 2.9, the transverse velocities are all small, and the streamlines follow the aperture. Figures 2.9b, 2.9d, 2.9f are examples where the GG22 model performs poorly, due to significant transverse velocities and the development of stable eddies within the aperture peaks. Fluid flows out of the aperture troughs like a jet.

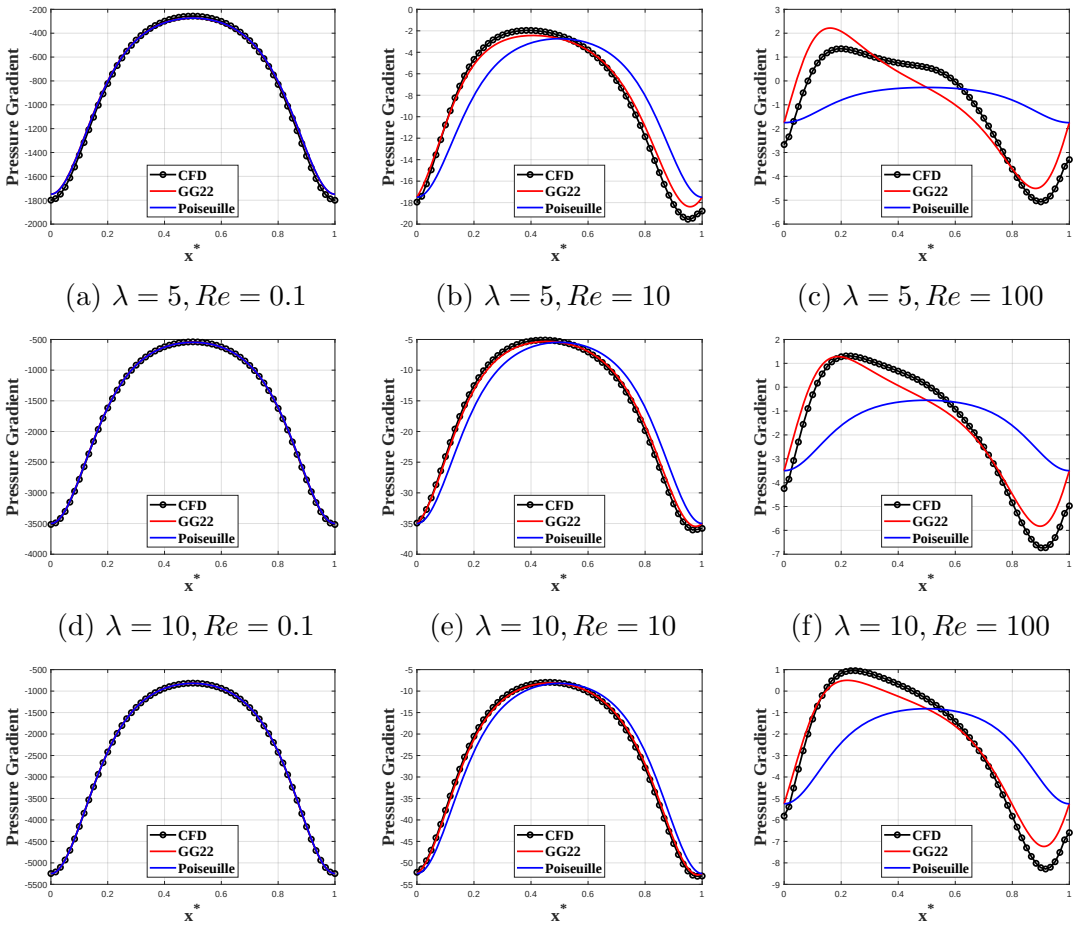

(a) $\lambda = 5, Re = 0.1$ (b) $\lambda = 5, Re = 10$ (c) $\lambda = 5, Re = 100$

(d) $\lambda = 10, Re = 0.1$ (e) $\lambda = 10, Re = 10$ (f) $\lambda = 10, Re = 100$

(g) $\lambda = 15, Re = 0.1$ (h) $\lambda = 15, Re = 10$ (i) $\lambda = 15, Re = 100$

Figure 2.11: Pressure gradients from the reduced dimension models compared with the gradient of the average pressure for selected wavelengths and Reynolds numbers at $\varepsilon = 0.3$. The GG22 model shows the greatest improvements in the weak inertial regime. While error increases with the Reynolds number, it decreases as the wavelength increases and still shows a significant improvement over the Poiseuille flow model.

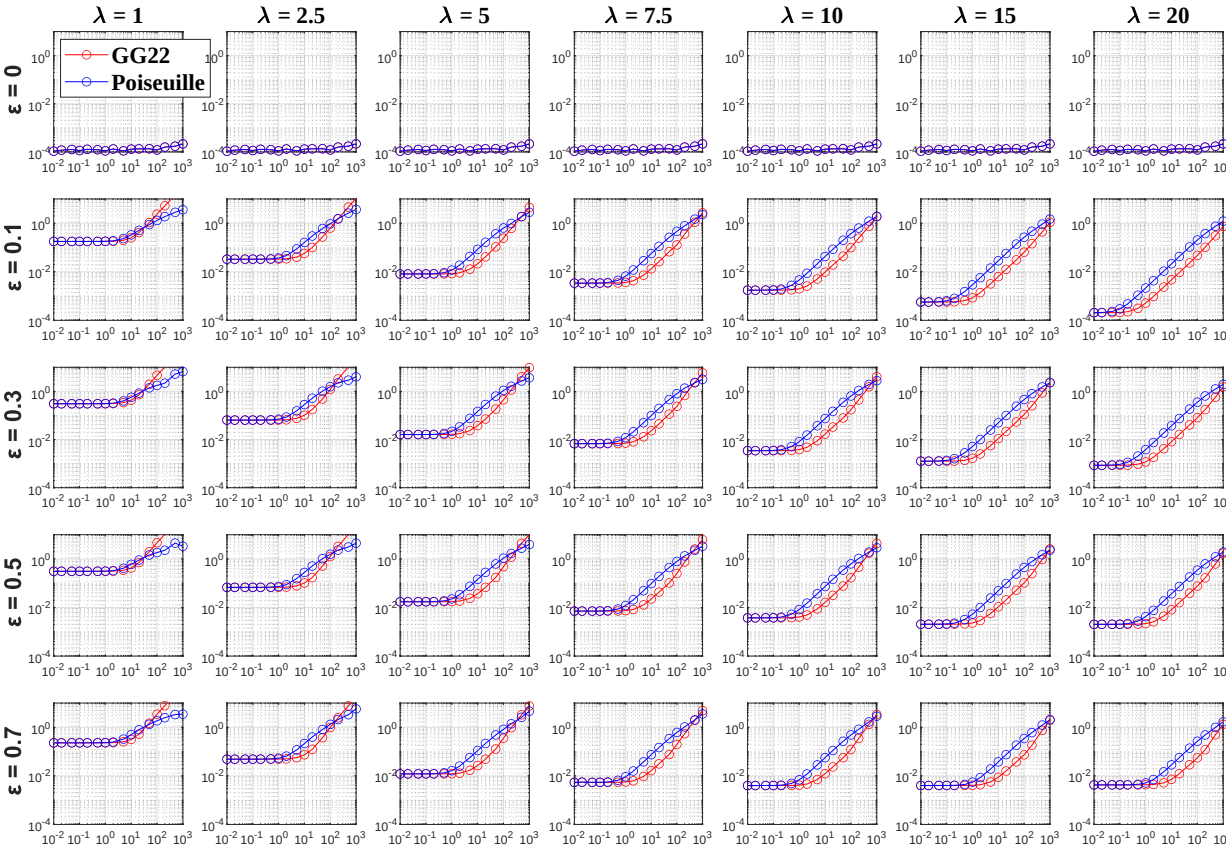

Figure 2.12: Error in the gradient of the average pressure from the full Navier-Stokes simulation compared to the reduced dimension models. Each subplot illustrates the error, ϵ, as a function of Reynolds number, Re, for a corresponding wavelength, λ, and amplitude ε. GG22 always performs at least as well if not better than Poiseuille flow. The exception to this rule is the quadrant with short wavelengths and high Reynolds numbers, in which neither model performs particularly well.

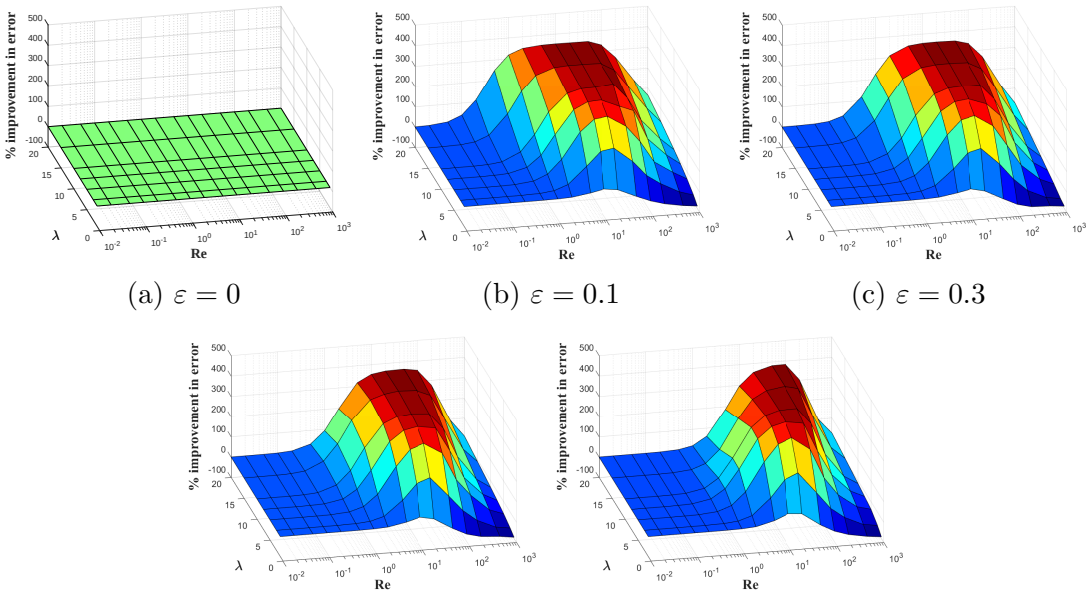

(a) $\varepsilon = 0$ (b) $\varepsilon = 0.1$ (c) $\varepsilon = 0.3$

(d) $\varepsilon = 0.5$ (e) $\varepsilon = 0.7$

Figure 2.13: Improvement in the error of the gradient of the average pressure when using the GG22 model as opposed to Poiseuille flow. In the weak inertial regime, $1 < Re < 100$, improvements of up to 400% are observed.

so the error observed in the other cases is attributed to the differences in the models and not the method by which the error is calculated.

As illustrated in Figure 2.12, the GG22 model always performs at least as well as the Poiseuille flow model. The exception to this trend is the quadrant with high Reynolds numbers and short wavelengths, in which the Poiseuille model has lower error not because it is a better approximation of the physics, but rather because neither model performs well. The error increases with increasing amplitude and decreases with increasing wavelength. As expected, the error for any given wavelength and amplitude are linear piecewise continuous functions of the Reynolds number. At low Reynolds numbers the error is constant and with increasing Reynolds numbers the error increases logarithmically. The transition point between the two behaviours occurs somewhere between $1 < Re < 100$. We therefore define three flow regimes based on the Reynolds number: the viscous regime ($Re < 1$), the weak inertial regime ($1 < Re < 100$), and the strong inertial regime ($Re > 100$).

In the viscous regime ($Re < 1$), where inertial forces are negligible, the solution to the Navier-Stokes equations is not a function of the Reynolds number and is instead only a function of the geometry. Viscous forces dominate over inertial forces, such that the non-linear terms in the GG22 model are small and the GG22 model tends towards the Poiseuille flow model, and hence why no improvement in the error is observed. Error in this regime is generally small ($< 5\%$) and both reduced dimension models are generally good at predicting the pressure profile, though error increases when the wavelength is short. This behaviour is as expected and is consistent with observations from previous studies of

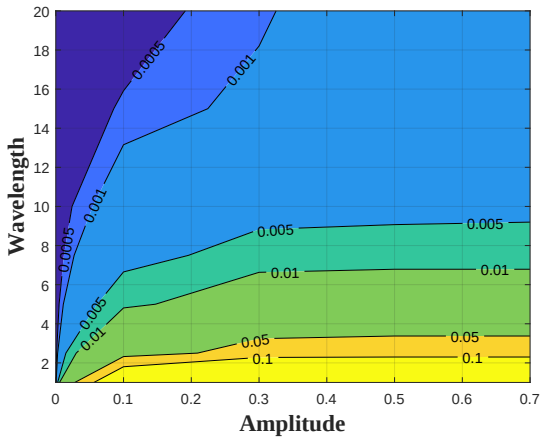

Figure 2.14: Error in the viscous regime as a function of amplitude, ε and wavelength, λ. Error in this regime does not depend on Reynolds number and is only a function of geometry.

Poiseuille flow [8, 9, 38]. Figure 2.14 shows the error in the viscous regime as a function of amplitude and wavelength.

In the weak inertial regime ($1 < Re < 100$), inertial forces start to influence the pressure gradient. The error in the Poiseuille flow model increases logarithmically starting at a Reynolds number of $Re \approx 1$ for all aperture wavelengths and amplitudes. The GG22 model performs much better than Poiseuille flow, showing up to 400% improvements in error. The GG22 model also eventually demonstrates logarithmically increasing error, but the transition point is much later than that of the Poiseuille flow model. As the wavelength increases, so too does the Reynolds number at which the GG22 transitions from constant to logarithmically increasing error.

The comparably poor accuracy of the Poiseuille flow model in the weak inertial regime is noteworthy because fracture flows in this domain are regularly encountered during industrial processes such as hydraulic fracturing but are also possible during natural phenomena like seismic events. Furthermore, the Poiseuille flow model demonstrates significant deviations from the Navier-Stokes behaviour for fractures with even modest deviations from the assumed parallel plate geometry. The errors associated with such modest deviations (as opposed to those from surface roughness) have been presumed to be small in the majority of hydraulic fracture and discrete fracture network analyses. The results here demonstrate that significant deviations between the Poiseuille flow and Navier-Stokes behaviour exists in common scenarios. The GG22 model is significantly more accurate in the weak inertial regime for fractures with modest spatial variations in aperture.

In the strong inertial regime ($Re > 100$), error in both models is generally large as neither model is particularly good at predicting the pressure gradient. The GG22 model still sees improvements in error of at least 10% and up to 300% at long wavelengths. At short wavelengths in this regime, fundamentally two-dimensional phenomena, such as the development of stable eddies, are observed in the Navier-Stokes solution, which is not the kind of behaviour that the reduced dimension models have been developed to capture. The

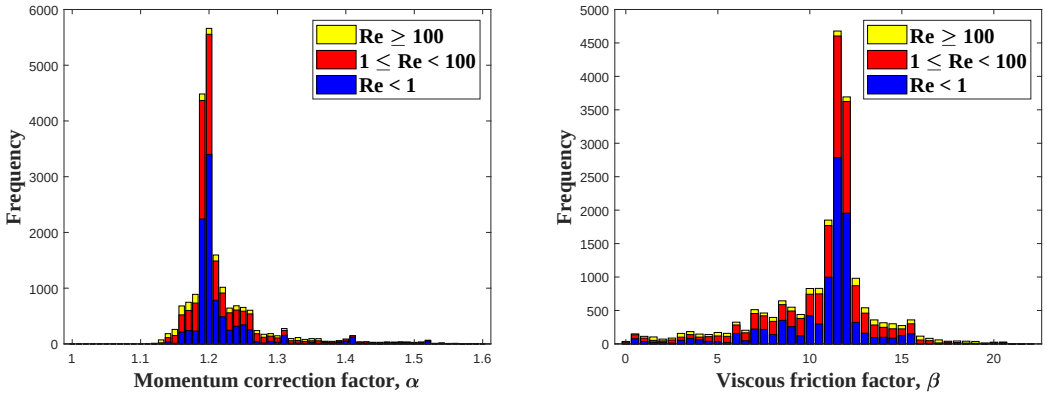

Figure 2.15: Frequency of velocity profile coefficients extracted from Navier-Stokes CFD solutions. Both the momentum correction factor and the viscous friction factor are heavily clustered around the parabolic velocity profile values of $\alpha = 1.2$ and $\beta = 12$.

CFD solutions show that at high Reynolds numbers and larger amplitudes, the velocity profile resembles a jet in which flow is contained to a thin region around the centerline. This suggests that improvements in error may be possible if an effective hydraulic aperture is adopted at high Reynolds number, rather than using the geometric aperture.

Calculating the full Navier-Stokes solution also means that we have access to the velocity profiles throughout each fracture. We can use these velocity profiles to calculate the true values of the momentum correction factor α, and the viscous friction factor, β in each tested case. Figure 2.15 shows the histograms of each factor extracted from the CFD profiles. Any cases which exhibited negative flow in the longitudinal direction are ignored, as they invalidate the assumptions behind these coefficients. Both factors are heavily clustered around the parabolic velocity profile values of $\alpha = 1.2$ and $\beta = 12$. The strong inertial regime shows slightly higher standard deviations, but the mean values remain close to the ideal parabolic profiles. While the pressure gradient predictions may be improved using the calculated values of α and β, it is not possible to determine a general empirical equation for the two factors from these cases. The factors display some correlation with aperture curvature in the viscous regime, but it is not possible to differentiate whether this is a correlation with aperture curvature or simply the aperture due to the cyclical nature of the sinusoidal aperture. The factors also display some correlation to wavelength, λ, and amplitude, ε, but these are parameters specific to the considered domain. Therefore, we recommend that the momentum correction factor, α, and the viscous friction factor, β, be considered as constants within the laminar flow regime, such that the factors only change when the flow transitions into the transitional and turbulent flow regimes. For the remainder of this thesis, β will be taken as $\beta = 12$.

This example shows the quantitative improvement in the ability of the GG22 model to predict the pressure gradient in the case of steady state laminar flow through rigid non-parallel apertures. Error in both models increases with Reynolds number and decreases as the wavelength increases. While the error in the GG22 and Poiseuille models is similar in the viscous regime ($Re < 1$), the GG22 model shows significant improvement in the weak

inertial regime ($1 \leq Re \leq 100$). While the error increases in both models in the strong inertial regime ($Re > 100$), the GG22 model still shows improvements over Poiseuille flow, especially at longer wavelengths.

2.5 Conclusions

In this chapter, a new reduced-dimension model for flow through deformable fractures has been derived and verified. By integrating the higher-order Navier-Stokes equations over the aperture of the fracture and making simplifying assumptions, we can remove the transverse component of flow from these equations. We thereby create a reduced-dimension set of governing equations which do not require discretization across the aperture and thus reducing the computational burden compared to the full Navier-Stokes equations while still capturing inertial, turbulent, and transient flow behaviours.

The GG22 model is demonstrated to capture complex inertial and transient behaviours under transient fluid boundary conditions and moving solid boundary conditions, and conserve energy in non-parallel plate geometries. The GG22 model recovers the Poiseuille flow model under Poiseuille flow conditions, and the non-linear extension to Forchheimer flow is explored. The error between the full Navier-Stokes solution and reduced-dimension models is quantified for steady-state laminar flow through sinusoidally varying aperture fields. The GG22 model demonstrates up to 400% improvements in error over the Poiseuille flow model. The error in the GG22 model increases at higher Reynolds numbers, but decreases with increased wavelength.

At the cost of increased complexity, the GG22 model is demonstrated to be superior to the Poiseuille flow model in all tested conditions. The next step in our investigation of inertial, turbulent, and transient behaviours in fracture flow is to develop a mathematical method to solve non-trivial boundary value problems and explore how fluid behaviour changes as a result of these phenomena.

Chapter 3

Numerical Methods for Solving the GG22 Model

3.1 Introduction

Having derived the GG22 model governing equations, we need a method to obtain solutions for non-trivial boundary value problems. The purpose of this chapter is to develop and verify a novel numerical method to solve the governing equations of the GG22 model subject to a given time and space varying aperture field that is uncoupled from the fluid behaviour.

The GG22 and Navier-Stokes models share many similarities. Both models: are two-field models; are governed by the conservation of mass and momentum; and do not have an equation that directly governs the fluid pressure. This is fortunate, as it allows the GG22 model to make use of the abundance of literature on numerical methods for solving the incompressible Navier-Stokes equations. To name a few, these methods include the fractional step method [47, 48], the pressure Poisson equation [49, 50], pressure-velocity coupling algorithms like SIMPLE [51] and PISO [52] among others [53, 54], and artificial compressibility [55] among many others. However, the GG22 model has several idiosyncrasies which must also be addressed: the GG22 model does not include diffusion, which makes the conservation of momentum an advective equation; the conservation of momentum contains an additional non-linear body force term which accounts for momentum dissipated by both viscous forces and turbulent eddy motion; and the GG22 model contains integrated mechanical coupling terms which govern how the fluid responds to changes in the aperture. The lack of diffusion and the non-linear body force term lead to unstable simulations, so additional corrective measures must be developed to adapt existing numerical methods for the GG22 model.

It is popular to solve Poiseuille flow equations using implicit finite element methods [7, 13, 29, 56], as the governing equation simplifies to a parabolic diffusion equation. Due to the advective nature of the GG22 equations, the finite volume method is instead adopted due to its relative ease of handling advective equations compared to the finite element method [57, 58, 59]. Implicit methods are popular for both Poiseuille flow and the Navier-

Stokes models, as the diffusive terms in both models lead to an undesirable restriction in explicit methods between the critical timestep, Δt^{crit}, and the characteristic mesh size, Δx, in which $\Delta t^{crit} \propto \Delta x^2$ [59]. As the GG22 model does not contain diffusive terms, it avoids this undesirable restriction, and allows for the use of fast, low-cost explicit methods. Furthermore, many applications of the GG22 model (such as pressure pulsing) are fast processes which naturally require small timesteps, providing synergy to the use of an explicit solution scheme.

In Section 3.3, an explicit finite volume method is presented. Next, Section 3.4 discusses the stability of the numerical scheme through a perturbation analysis and methods to address the instabilities are discussed. Section 3.5 and 3.6 verify the method against known analytical solutions, and examine the convergence properties of the method. Last, the response of the GG22 model to a travelling aperture wave is solved and explored for the first time using the developed method in Section 3.8.

3.2 Governing Equations

This section summarizes the GG22 governing equations derived in Chapter 2. The equations governing the GG22 model are [41]

$$\frac{\partial w}{\partial t} + \frac{\partial q}{\partial x} = 0 \tag{3.1}$$

$$\frac{\partial q}{\partial t} + \frac{\partial}{\partial x}\left(\alpha \frac{q^2}{w}\right) = -\frac{w}{\rho_f}\frac{\partial p}{\partial x} - \frac{1}{2}\frac{f_D}{w^2} q|q| \tag{3.2}$$

in which equation (3.1) represents the conservation of fluid mass, and equation (3.2) represents the conservation of fluid momentum through a fracture of varying aperture. They are functions of the primary variables, fluid flux $q(x,t)$ $[m^2/s]$, and fluid pressure $p(x,t)$ $[Pa]$. The fracture aperture is denoted by $w(x,t)$ $[m]$ and in this chapter is considered a given field.

The equation of momentum is supplemented by two dimensionless coefficients which depend upon the fluid flow regime and Reynolds number. The first coefficient, α, is the momentum correction factor. The momentum correction factor is a function of the shape of the fluid velocity profile across the aperture. The momentum correction factor is defined as

$$\alpha = \alpha(Re, \nabla w) \approx \begin{cases} \frac{6}{5} & \text{if } Re \leq 2000 \\ \frac{64}{63} & \text{if } Re \geq 4000 \end{cases} \tag{3.3}$$

$$Re = \frac{\rho_f \bar{v} w}{\mu} = \frac{\rho_f |q|}{\mu} \tag{3.4}$$

in which $Re \leq 2000$ defines the laminar flow regime and $Re \geq 4000$ defines the turbulent flow regime. The momentum correction factor is calculated assuming a parabolic velocity profile in the laminar regime, and assuming a power law velocity profile in the turbulent regime.

The second coefficient, f_D, is the Darcy friction factor, defined as

$$f_D = \begin{cases} \frac{24}{Re} & \text{if } Re \leq 2000 \\ \frac{1}{\sqrt{f_D}} = -2\log(\frac{\epsilon}{7.4w} + \frac{2.51}{Re\sqrt{f_D}}) & \text{if } Re \geq 4000 \end{cases} \tag{3.5}$$

in which ϵ/w $[m/m]$ is the relative roughness of the fracture. In the laminar regime, the friction factor is determined analytically and accounts for viscous dissipation by a steady-state parabolic velocity profile. In the turbulent regime the friction factor is approximated by adopting phenomenological the Colebrook-White equation [45]. In the transitional regime, $2000 < Re < 4000$, the momentum correction and Darcy friction factors are linearly interpolated.

3.3 Numerical Formulation

In this section, an explicit finite volume method for the GG22 equations is developed. Like the Navier-Stokes equations, the GG22 model has no equation which governs the pressure. Due to the similarities, explicit techniques developed for the Navier-Stokes equations can be applied to the GG22 model. Unlike the Navier-Stokes equations, there is no diffusion in the GG22 model, which means that the explicit formulation is not plagued by the timestep restriction $t^{crit} \propto \Delta x^2$ of explicit Navier-Stokes formulations. However, additional special treatment is required to address the unique instabilities that arise in the GG22 equations. The result is a fast and computationally efficient numerical formulation.

3.3.1 Pressure Poisson equation

The primary issue with the explicit formulation is that the governing equations do not contain an equation to explicitly update the pressure. The second issue is that while the momentum equation can update the fluxes, there is no guarantee that the updated fluxes will satisfy continuity. A common technique, adopted here, is to create a new equation which may be used to explicitly update the pressure and also ensures that the updated pressure field enforces continuity on the updated fluxes. This new equation is known as the Pressure Poisson Equation (PPE) [49, 50, 57].

To derive the PPE for the GG22 model, the transient terms in the momentum equation are first discretized in time. A two-level backwards Euler method is adopted. On the right-hand side of the equation, the friction and convective terms are lagged and evaluated at timestep $n-1$, while the pressure term is evaluated at the current timestep n.

$$\frac{1}{\Delta t}(q^n - q^{n-1}) = -(H^{n-1}) - \left(\frac{w}{\rho_f}\frac{\partial p}{\partial x}\right)^n \tag{3.6}$$

$$H = \frac{\partial}{\partial x}\left(\alpha\frac{q^2}{w}\right) + \frac{1}{2}\frac{f_D}{w^2}q|q| \tag{3.7}$$

Next, the spatial derivative (divergence) of the momentum equation is taken, giving

$$\frac{1}{\Delta t}\frac{\partial}{\partial x}(q^n - q^{n-1}) = -\frac{\partial}{\partial x}(H^{n-1}) - \frac{\partial}{\partial x}\left(\frac{w}{\rho_f}\frac{\partial p}{\partial x}\right)^n \tag{3.8}$$

Using the continuity equation, (3.1), the divergence of q is replaced by the time derivative of w in equation (3.8). Thus, the PPE can be used to update the pressures at timestep n based on the fluxes at timestep $n-1$, and on the rate of aperture change at timesteps n and $n-1$:

$$\frac{\partial}{\partial x}\left(\frac{w}{\rho_f}\frac{\partial p}{\partial x}\right)^n = -\frac{\partial}{\partial x}(H^{n-1}) - \frac{1}{\Delta t}\left(-\frac{\partial w}{\partial t}^n + \frac{\partial w}{\partial t}^{n-1}\right) \tag{3.9}$$

Pressure boundaries, Γ_p, are Dirichlet conditions on the PPE. Flux boundaries, Γ_q, act as Neumann boundary conditions on the PPE. An appropriate Neumann boundary condition may be derived from the governing equations [49, 50]. By evaluating the momentum equation at the flux boundary, we find

$$\left.\frac{w}{\rho_f}\frac{\partial p}{\partial x}\right|_{\Gamma_q} = -\left.\frac{\partial \overline{q}}{\partial t}\right|_{\Gamma_q} - \left.\frac{\partial}{\partial x}\left(\alpha\frac{\overline{q}^2}{w}\right)\right|_{\Gamma_q} - \left.\frac{1}{2}\frac{f_D}{w^2}\overline{q}|\overline{q}|\right|_{\Gamma_q} \tag{3.10}$$

in which $\overline{q}$ is the prescribed flux at the boundary.

3.3.2 Flux update and continuity correction

Once the pressures at timestep n have been determined, the fluxes can be easily updated using the momentum equation, according to

$$q^{n*} = q^{n-1} - \Delta t\left(H^{n-1} + \frac{w}{\rho_f}\frac{\partial p^n}{\partial x}\right) \tag{3.11}$$

in which q^{n*} is the uncorrected flux.

Here the derivation of the GG22 finite volume method deviates from the Navier-Stokes methods. The developed PPE is supposed to enforce continuity in the fluxes when updated, but there are two issues that arise. First, in the derivation of equation (3.9), we made use of the relationship $q_{,x} = -\dot{w}$. However the combined flux and friction term, H, when expanded by the divergence operator, also contains the divergence of the flux. The continuity equation has not been directly substituted into these terms, and thus continuity was not rigorously enforced in the derivation of the PPE. The resulting fluxes therefore only satisfy continuity if the previous fluxes exactly satisfy continuity. The second issue is that small errors (such as round-off) arise in the fluxes. The fluxes at timestep $n-1$ may satisfy continuity to numerical precision, but they do not satisfy continuity exactly. Experience has demonstrated that the formulation is susceptible to small perturbations which will accumulate and propagate in an unbounded fashion (explored further in section 3.4). The solution proposed in this article is to introduce an additional step to the explicit scheme, which corrects the fluxes such that continuity is satisfied.

The fluxes are corrected by minimizing the differences between the new corrected fluxes, q^n, from the current fluxes, q^{n*}, while constraining the new fluxes to enforce continuity. This problem can be addressed by introducing a Lagrange multiplier [57]. The problem is therefore to find the saddle point of the Lagrangian

$$\mathcal{L} = \frac{1}{2}\int_0^L (q^n - q^{n*})^2\,dx - \int_0^L \lambda\left(\frac{\partial}{\partial x}(q^n) + \frac{\partial}{\partial t}(w^n)\right)dx \tag{3.12}$$

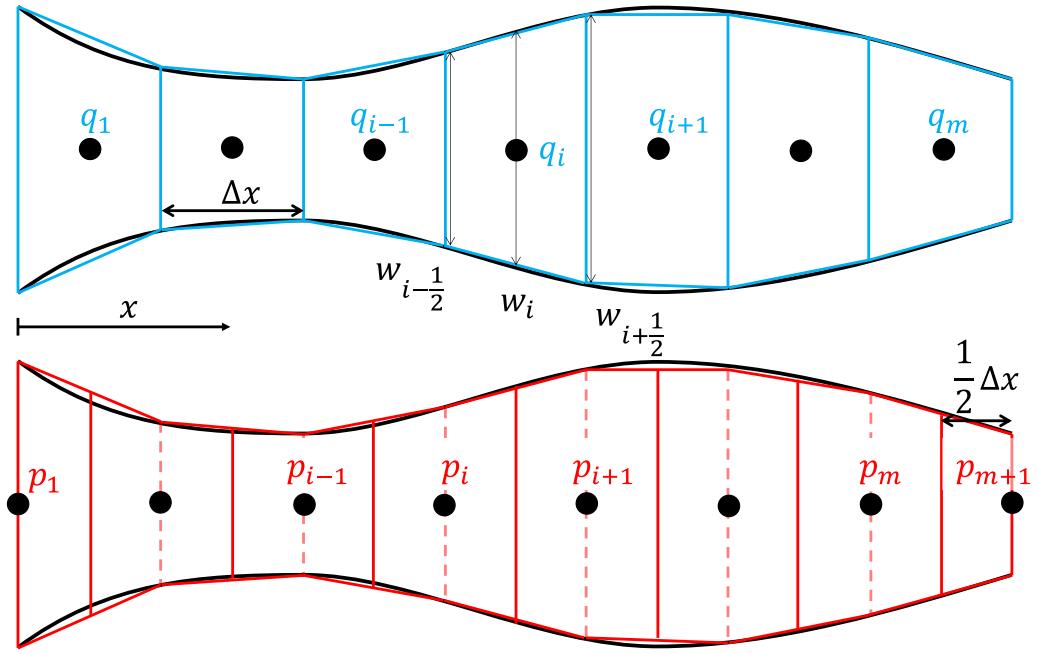

Figure 3.1: Staggered finite volume mesh. The top row shows the domain of non-uniform aperture divided into m uniform flux cells, while the bottom row shows the domain divided into $m+1$ pressure cells. Aperture is taken at the interfaces of the flux cells and is assumed to be linear over the cell.

in which $\lambda = \lambda(x)$ is the Lagrange multiplier. This process yields an additional equation for the Lagrange multiplier:

$$\frac{\partial^2 \lambda}{\partial x^2} = \frac{\partial}{\partial t}(w^n) + \frac{\partial}{\partial x}(q^{n*}) \tag{3.13}$$

subject to the boundary conditions $\lambda = 0$ on Γ_p, and $\lambda_{,x} = 0$ on Γ_q. Full details of the derivation are available in Appendix A. After solving for λ, the fluxes can then be corrected according to

$$q^n = q^{n*} - \frac{\partial \lambda}{\partial x} \tag{3.14}$$

3.3.3 Finite volume discretization

The governing equations are discretized in space using the finite volume method. A staggered grid method is adopted [57, 59], and the domain is discretized into two meshes — one for the fluxes, and an offset grid for the pressures. The finite volume mesh discretization is illustrated in Figure 3.1.

The domain is discretized into m uniform flux cells of length Δx. The aperture field is discretized into $m + 1$ points taken at the flux cell faces, such that the aperture at the cell faces is continuous. q_i denotes the flux in each cell while $w_{i-\frac{1}{2}}$ denotes the aperture at the left face while $w_{i+\frac{1}{2}}$ denotes the aperture at the right face. The aperture is assumed

to vary linearly over each cell, such that $w_i = \overline{w} = \frac{1}{2}\left(w_{i-\frac{1}{2}} + w_{1+\frac{1}{2}}\right)$. The domain is discretized into $m+1$ pressure cells, which are offset from the flux cells, such that nodes of the pressure cells are aligned with the faces of the flux cells. The pressure cells at the ends of the domain are of length $\frac{1}{2}\Delta x$. The nodes of the cells at the beginning and end of the domain are placed at $x = 0$ and $x = L$, rather than being placed at the centroid of the cell, to ensure the pressure cell nodes remain aligned with the flux cell faces.

The finite volume method yields a system of discrete equations from the semi-discrete equations (3.9), (3.11), and (3.13). Starting with the pressure cells, the PPE is integrated over each cell from the starting position $x = x_1^e$ to the end position $x = x_2^e$.

$$\int_{x_1^e}^{x_2^e} \frac{\partial}{\partial x}\left(\frac{w}{\rho_f}\frac{\partial p}{\partial x}\right)^n dx = -\int_{x_1^e}^{x_2^e} \frac{\partial}{\partial x}\left(H\right)^{n-1} dx - \int_{x_1^e}^{x_2^e} \frac{1}{\Delta t}\left(-\dot{w}^n + \dot{w}^{n-1}\right) dx \tag{3.15}$$

$$\frac{w^n}{\rho_f}\frac{\partial p^n}{\partial x}\bigg|_{x_1^e}^{x_2^e} = -H^{n-1}\bigg|_{x_1^e}^{x_2^e} - \frac{1}{\Delta t}\left(-\dot{w}^n + \dot{w}^{n-1}\right)\bigg|_{x_1^e}^{x_2^e} \tag{3.16}$$

The pressure gradient is discretized using a central difference scheme. Special considerations are necessary in the end cells to account for boundary conditions, which are documented in Appendix B. The left-hand side simplifies to

$$\frac{w^n}{\rho_f}\frac{\partial p^n}{\partial x}\bigg|_{x_1^e}^{x_2^e} = \frac{1}{\rho_f \Delta x}\left[w_{i-1}p_{i-1} - (w_i + w_{i-1})p_i + w_i p_{i+1}\right]^n \tag{3.17}$$

The right-hand side consists of the convective term, the friction term, and the continuity terms. The convection term expands and requires that the derivatives of α, q, and w be evaluated at each face of the cell. All three of these derivatives are determined numerically using central difference. All the terms on the right-hand side are combined into a single source term,

$$S_{pi}\left(q_i^{n-1}, \dot{w}_i{}^n, \dot{w}_i{}^{n-1}\right) = -H^{n-1}\bigg|_{x_1^e}^{x_2^e} - \frac{1}{\Delta t}\left(-\dot{w}^n + \dot{w}^{n-1}\right)\bigg|_{x_1^e}^{x_2^e} \tag{3.18}$$

which is detailed in Appendix B. The result is a system of discrete equations for the pressure at timestep n:

$$w_{i-1}p_{i-1}^n - (w_i + w_{i-1})p_i^n + w_i p_{i+1}^n = \rho_f \Delta x \cdot S_{pi} \tag{3.19}$$

Next, the time-discretized equation of momentum (3.6) is integrated over the flux cells.

$$\begin{aligned}\int_{x_1^e}^{x_2^e} q^n dx = &\int_{x_1^e}^{x_2^e} q^{n-1} dx - \Delta t \int_{x_1^e}^{x_2^e} \frac{\partial}{\partial x}\left(\alpha \frac{(q^{n-1})^2}{w^{n-1}}\right) dx \\ &- \Delta t \int_{x_1^e}^{x_2^e} \frac{1}{2}\frac{f_D}{(w^{n-1})^2}(q^{n-1})|q^{n-1}| dx - \Delta t \int_{x_1^e}^{x_2^e} \frac{w^n}{\rho_f}\frac{\partial p^n}{\partial x} dx\end{aligned} \tag{3.20}$$

$$q_i^n = q_i^{n-1} - \frac{\Delta t}{\Delta x}\left(\alpha \frac{(q^{n-1})^2}{w^{n-1}}\right)\bigg|_{x_1^e}^{x_2^e} - \frac{\Delta t}{2}\frac{f_D}{(w_i^{n-1})^2}(q_i^{n-1})|q_i^{n-1}| - \frac{\Delta t}{\Delta x \rho_f}(wp)^n\bigg|_{x_1^e}^{x_2^e} \tag{3.21}$$

To interpolate the fluxes at the cell faces for the convection term, the quadratic QUICK scheme is used. Let the fluxes at each cell face be denoted as $q(x_1^e) = q_{i,1}$ and $q(x_2^e) = q_{i,2}$. Thus, the fluxes are updated according to

$$\begin{aligned} q_i^n = q_i^{n-1} &- \frac{\Delta t}{\Delta x}\left[\frac{\alpha(q_{i,2})}{w_{i+\frac{1}{2}}}(q_{i,2}^{n-1})^2 - \frac{\alpha(q_{i,1})}{w_{i-\frac{1}{2}}}(q_{i,1}^{n-1})^2\right] \\ &- \frac{\Delta t f_D(q_i)}{2(w_i^{n-1})^2}(q_i^{n-1})|q_i^{n-1}| \\ &- \frac{\Delta t}{\Delta x \rho_f}(w_{i+\frac{1}{2}}^n p_{i+1}^n - w_{i-\frac{1}{2}}^n p_i^n) \end{aligned} \tag{3.22}$$

While the PPE yields a set of discrete equations which must be solved simultaneously, the flux update is performed based on the local flux and pressure balance.

Last, the continuity correction is also discretized using the finite volume method over the flux cells.

$$\int_{x_1^e}^{x_2^e} \frac{\partial^2 \lambda_i}{\partial x^2} dx = \int_{x_1^e}^{x_2^e} \frac{\partial}{\partial t}(w_i^n) dx + \int_{x_1^e}^{x_2^e} \frac{\partial}{\partial x}(q^{n*}) dx \tag{3.23}$$

$$\left.\frac{\partial \lambda_i}{\partial x}\right|_{x_1^e}^{x_2^e} = \Delta x \dot{w_i}^n + \left(q_{i,2}^{n*} - q_{i,1}^{n*}\right) \tag{3.24}$$

The left hand side is discretized using central differencing, with special considerations in the end cells for boundary conditions provided in Appendix A. The following discrete set of equations for λ are obtained.

$$\lambda_{i-1} - 2\lambda_i + \lambda_{i+1} = (\Delta x)^2 \dot{w_i}^n + \Delta x \left(q_{i,2}^{n*} - q_{i,1}^{n*}\right) \tag{3.25}$$

The continuity correction (3.14) requires the gradient of λ, so the gradient is then reconstructed from the discretized values of λ using central differencing.

3.3.4 Summary of the explicit algorithm

For each timestep, n,

- Start with known fields $w(x,t)$ and $q^{n-1}(x)$ which satisfy the continuity equation.
- Determine the pressures, p^n, by solving the global system of equations (3.19) given inputs $w^n, w^{n-1}, \dot{w}^n, \dot{w}^{n-1}, q^{n-1}$.
- Determine the uncorrected fluxes, q^{n*}, using equation (3.22) given inputs $w^n, w^{n-1}, q^{n-1}, p^n$.
- Determine the Lagrange multipliers, λ, by solving the global system of equations (3.25) given inputs $\dot{w}^n, q^{n*}$.
- Determine the corrected fluxes, q^n, using equation (3.14) given inputs q^{n*}, λ.
- Set $n = n - 1$ and proceed to the next timestep.

The resulting explicit algorithm is fast and low-cost. The global system of equations to solve for pressure and the continuity correction are both banded matrices which provide favourable inversion properties. The computational time is governed primarily by the number of timesteps rather than the cost of each timestep.

3.3.5 Critical timestep

It has been shown that one of the conditions to ensure boundedness of the solution is that all flux coefficients in the discretized flux update (3.22) have the same sign [59]. For the purpose of approximating the critical timestep, the QUICK interpolation scheme is replaced with the Upwind Differencing Scheme (UDS), which removes the contribution of the cells q_{i+2} and q_{i-2}. Ensuring that all coefficients have the same sign yields the approximated critical timestep,

$$\Delta t_i^{crit} \leq \left(\frac{v_{\max}}{\Delta x} + \phi\right)^{-1}, \; v_{\max} = \frac{\alpha q_i^{n-1}}{w_i^{n-1}}, \; \phi = \frac{f_D q_i^{n-1}}{2(w_i^{n-1})^2} \tag{3.26}$$

The first term of the critical timestep comes from the convection term, in which v_{max} is the maximum longitudinal fluid velocity. This term is standard to other explicit critical timesteps in that the maximum timestep is limited to the rate at which information can propagate through the mesh. The second term is related to the friction body source term. ϕ is the fundamental frequency of the fracture-fluid system, thus the maximum timestep is also limited by the fundamental period of the system.

3.4 Perturbation Analysis

In this section, we show that the explicit finite volume formulation without the continuity correction is unstable due to the amplification of small errors.

Consider the case of steady-state flow in a rigid channel of uniform aperture, subject to a constant pressure gradient of $\Delta p/L$. Assume the system is at steady-state so that the flux in all cells is equal to the steady-state flux q_{ss} while the algorithm continues to march forward in time. The flow is assumed to be in the fully laminar regime, such that $q_{ss} = -\frac{w_0^3}{12\mu}\frac{\Delta p}{L}$. For simplicity, convective terms are neglected.

Let there be a small error introduced in each flux volume, such that $q_i^n = q_{ss} + b_i^n \epsilon$, in which $b_i^n \in \mathbb{R}$ is a random multiplier of the small error ϵ. The error ϵ is very small, $\epsilon << q_{ss}$, arising for example from round-off error. Furthermore, $b_{i-1}^n \neq b_i^n \neq b_{i+1}^n$, so that continuity is no longer exactly satisfied, although it may still be satisfied to numerical tolerance.

While the flux is updated based on the local flux and pressure balance, the pressure Poisson equation requires solving a global set of equations and is therefore difficult to generalize. We will consider a domain discretized into only two flux volumes, as shown in Figure 3.2. This is the simplest possible system which contains both free pressure and flux degrees of freedom (two free fluxes and one free pressure). We will now march the algorithm forward in time and examine the behaviour of these random errors.

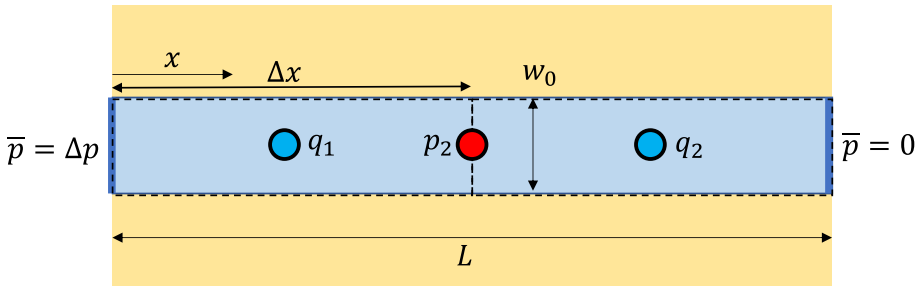

Figure 3.2: Rigid channel of uniform aperture discretized into two flux volumes for perturbation analysis.

Starting with the pressure, the source term and the single free pressure at timestep $n+1$ are

$$S_{p2}^{n+1} = \frac{-12\Delta x\mu}{w_0^2}(b_2^n - b_1^n)\epsilon \tag{3.27}$$

$$p_2^{n+1} = \frac{1}{2}\Delta p + \frac{24\Delta x\mu}{w_0^3}(b_2^n - b_1^n)\epsilon \tag{3.28}$$

The fluxes at the following timestep are

$$q_1^{n+1} = q_{ss} + \big((1-\zeta)b_1^n - 2\zeta(b_2^n - b_1^n)\big)\epsilon = q_{ss} + b_1^{n+1}\epsilon \tag{3.29}$$

$$q_2^{n+1} = q_{ss} + \big((1-\zeta)b_2^n + 2\zeta(b_2^n - b_1^n)\big)\epsilon = q_{ss} + b_2^{n+1}\epsilon \tag{3.30}$$

$$\zeta = \frac{12\mu\Delta t}{\rho_f w_0^2} = \phi\Delta t \tag{3.31}$$

in which $\zeta > 0$ is a dimensionless viscous friction parameter of the discretized system. We now have an iterative sequence for the growth of the error multipliers b_i which depend on the errors at the previous timestep and the parameters of the system. For the errors to diminish over time, the following condition must be satisfied:

$$\left|\frac{b_i^{n+1}}{b_i^n}\right| < 1 \tag{3.32}$$

Using the iterative sequence (3.29), the stability condition for cell 1 is

$$-1 < \frac{b_1^{n+1}}{b_1^n} < 1 \tag{3.33}$$

$$-1 < \frac{(1-\zeta)b_1^n - 2\zeta(b_2^n - b_1^n)}{b_1^n} < 1 \tag{3.34}$$

$$\left(\frac{1}{\zeta} + \frac{1}{2}\right) > C > \frac{1}{2}, \quad C = \frac{b_2^n}{b_1^n} \tag{3.35}$$

Likewise, the stability condition for cell 2 is

$$\left(\frac{1}{\zeta} + \frac{1}{2}\right) > \frac{1}{C} > \frac{1}{2} \tag{3.36}$$

and thus both the ratio $\frac{b_1^n}{b_2^n}$ and its reciprocal must fall within the same positive range.

The first requirement of these stability conditions is the timestep restriction, $\zeta < 2$ to ensure that $\left(\frac{1}{2} + \frac{1}{\zeta}\right) > 1$, otherwise one of the reciprocals must always be outside the acceptable range. Second, these conditions can only be met if both b_1^n and b_2^n have the same sign. As the error multipliers are random real numbers arising from uncontrollable errors, it is impossible to guarantee that the error multipliers meet these conditions. Therefore, in general, the algorithm is not stable as small random errors introduced by for example round-off error will always grow.

3.4.1 Perturbation analysis with artificial diffusion

In this section, artificial diffusion is introduced as a means to control the perturbations. The momentum equation becomes

$$\frac{\partial q}{\partial t} + \frac{\partial}{\partial x}\left(\alpha \frac{q^2}{w}\right) = -\frac{w}{\rho_f}\frac{\partial p}{\partial x} - \frac{1}{2}\frac{f_D}{w^2} q|q| - \beta \frac{\partial^2 q}{\partial x^2} \tag{3.37}$$

in which β is the artificial diffusion coefficient. The diffusion term is discretized using central differencing. Repeating the perturbation analysis, it is found that the parameters which satisfy the stability condition (3.32) are given by

$$\frac{9\gamma - \zeta - 2}{9\gamma - 2\zeta} < C_i < \frac{9\gamma - \zeta}{9\gamma - 2\zeta}, \quad (9\gamma - 2\zeta) > 0 \tag{3.38}$$

$$\frac{9\gamma - \zeta - 2}{9\gamma - 2\zeta} > C_i > \frac{9\gamma - \zeta}{9\gamma - 2\zeta}, \quad (9\gamma - 2\zeta) < 0 \tag{3.39}$$

in which $C_1 = \frac{b_2^n}{b_1^n}$, and $C_2 = \frac{b_1^n}{b_2^n} = \frac{1}{C_1}$. $\gamma = \frac{\beta \Delta t}{\Delta x^2} > 0$ is the diffusion parameter of the discretized system.

Artificial diffusion provides conditional stability. By choosing parameters $\frac{\gamma}{\zeta} = \frac{2}{9}$ and $\zeta < 2$, the stability condition becomes $-\infty < C_i < \infty$ and the error will always decrease over time. For all other ratios of $\frac{\gamma}{\zeta}$, the bounds are finite and therefore dependent on the magnitude of C. The primary disadvantage of artificial diffusion is that it introduces the undesirable $\Delta t^{crit} \propto \Delta x^2$ correlation, which imposes harsh restrictions on the timestep size. Therefore, we will instead examine the alternative proposed solution of introducing a continuity correction.

3.4.2 Perturbation analysis with continuity correction

Applying the continuity correction to the previous perturbation analyses, the Lagrange multipliers are found to be

$$\begin{bmatrix} \lambda_1 \\ \lambda_2 \end{bmatrix} = -\frac{\Delta x}{8} \begin{bmatrix} 1 \\ 3 \end{bmatrix} (b_2^{n+1} - b_1^{n+1})\epsilon \tag{3.40}$$

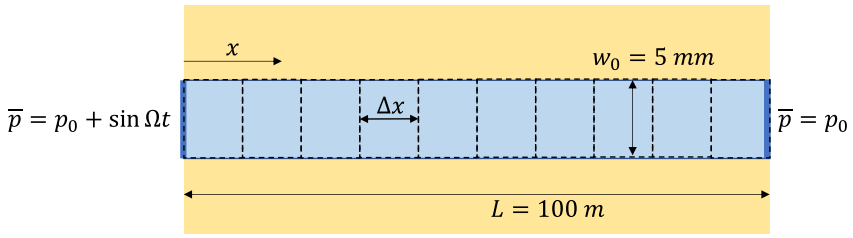

Figure 3.3: Domain for time convergence of flux with oscillating pressure inlet condition between parallel plates.

along with the boundary conditions $\lambda\big|_{x=0,L} = 0$. The gradient of the Lagrange multiplier is reconstructed using λ_1, λ_2, and the boundary conditions, such that

$$\left.\frac{\partial \lambda}{\partial x}\right|_{i=1} = \frac{1}{2}\left(\frac{\lambda_1 - \lambda|_{x=0}}{\frac{1}{2}\Delta x} + \frac{\lambda_2 - \lambda_1}{\Delta x}\right) \tag{3.41}$$

$$\left.\frac{\partial \lambda}{\partial x}\right|_{i=2} = \frac{1}{2}\left(\frac{\lambda_2 - \lambda_1}{\Delta x} + \frac{\lambda|_{x=L} - \lambda_2}{\frac{1}{2}\Delta x}\right) \tag{3.42}$$

The continuity corrected flux field is

$$(q_1)^{n+1} = (q_2)^{n+1} = q_{ss} + \frac{1}{2}\left(b_1^{n+1} + b_2^{n+1}\right)\epsilon \tag{3.43}$$

When the time-stepping algorithm is propagated forward, we find

$$q_i^{n+2} = q_{ss} + (1-\zeta)(b_i)^{n+1}\epsilon \tag{3.44}$$

so that the error will decrease in an exponential manner by a factor of $(1-\zeta)$ with each subsequent timestep. ζ is subject to the restriction that $\zeta < 2$, which introduces a timestep restriction that $\Delta t < \frac{2}{\phi}$. Satisfying the critical timestep (3.26) implicitly satisfies this condition, as $\Delta t^{crit} \leq \frac{1}{\phi}$, neglecting the convection term.

3.5 Convergence Analysis: Time-varying Flow Through a Channel

In this section, the temporal convergence of flux is investigated by simulating flow through a rigid channel of length L with uniform aperture w_0 and oscillating inlet pressure. The problem domain is illustrated in Figure 3.3.

The outlet pressure is fixed at p_0, while the inlet pressure oscillates at $p(x = 0, t) = p_0 + \sin \Omega t$, in which Ω is the excitation frequency. The resulting flux in the channel is constant along the channel but varies with time. In the laminar regime ($Re < 2000$), the exact flux, q^{ex}, is given by

$$\frac{12\mu L}{w_0^3} q^{ex} = \frac{-\phi}{\Omega^2 + \phi^2}\left(\Omega \cos \Omega t - \phi \sin \Omega t - \Omega e^{-\phi t}\right), \quad \phi = \frac{12\mu}{\rho_f w_0^2} \tag{3.45}$$

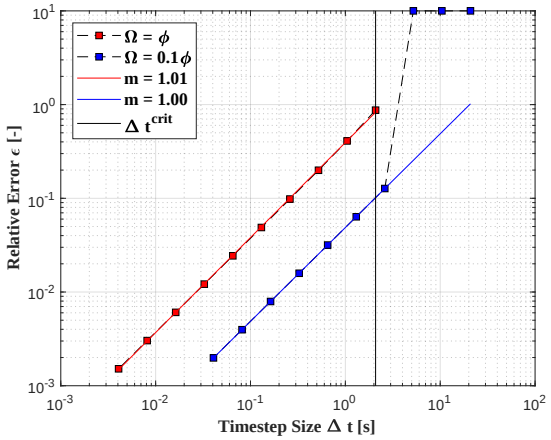

Figure 3.4: Flux convergence rates with respect to time for two different excitation frequencies with oscillating pressure boundary conditions. m is the rate of convergence, such that the algorithm displays $O(\Delta t^m)$ convergence with timestep refinement.

in which ϕ is the fundamental frequency of the channel. In this example, the dimensions of the domain are selected as $L = 100m$, $w_0 = 5mm$, and $\phi = 0.48s^{-1}$. Excitation frequencies of $\Omega = \phi$ and $\Omega = 0.1\phi$ are considered for a time of $t^{end} = 20/\Omega$. While a single flux cell is sufficient to exactly represent the linear pressure and constant flux distributions, a single cell is not susceptible to perturbations, so 10 flux cells are used to test the continuity correction. The error is taken as the normalized root-mean-square error between the numerical and exact solutions over time.

The convergence rates of the two different excitation frequencies are illustrated in Figure 3.4. While the error is greater with higher excitation frequencies, the numerical method displays an ideal $O(\Delta t^1)$ rate of convergence for both frequencies, which is expected with the two-level backwards Euler method.

Figure 3.4 also illustrates the ideal critical timestep. The critical timestep provides a guideline for the maximum stable timestep, but the continuity correction provides additional stability that may allow the solution to proceed, as shown by the datapoint at $\Delta t = 2.6s = 1.25\Delta t^{crit}$. If the spurious oscillations created by exceeding the critical timestep are small, then the continuity correction dampens any oscillations to acceptable numerical accuracy. However, timesteps that are too large will still cause instabilities, as shown by the datapoints at $\Delta t > 2.6s$.

3.6 Convergence Analysis: Steady-state Flow Through a Non-uniform Fracture

In this section, the spatial convergence of pressure is investigated. The problem domain is illustrated in Figure 3.5. The pressure at the outlet of a rigid channel of length L is fixed at $\overline{p} = 0$. The flux at the inlet is fixed at a constant $\overline{q}$. The domain is defined by a sinusoidal aperture, such that $w(x) = w_0\left(1 - \varepsilon\cos\left(\frac{2\pi x}{L}\right)\right)$, in which $0 \leq \varepsilon < 1$. The steady-

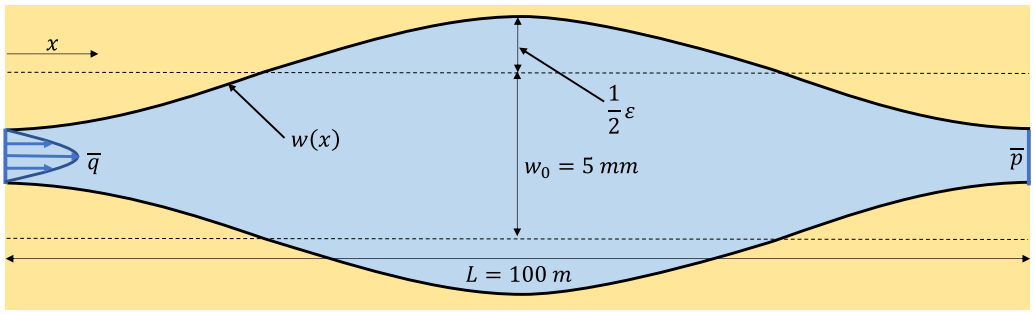

Figure 3.5: Domain for spatial convergence of pressure for steady state flow through a channel with sinusoidal aperture.

state pressure gradient is given analytically, and the pressure distribution is determined by numerically integrating the pressure gradient. The exact pressure and pressure gradients are

$$p = -\xi(L) + \xi(x) \tag{3.46}$$

$$\xi(x) = \int_0^x \frac{\partial p}{\partial x} dx \tag{3.47}$$

$$\frac{\partial p}{\partial x} = \frac{\rho_f \overline{q}^2}{w_0^2} \left(\frac{2\pi\alpha\varepsilon \sin\left(\frac{2\pi x}{L}\right)}{L\left(1 - \varepsilon\cos\left(\frac{2\pi x}{L}\right)\right)^3} - \frac{f_D}{2w_0\left(1 - \varepsilon\cos\left(\frac{2\pi x}{L}\right)\right)^3} \right) \tag{3.48}$$

The dimensions of the domain are selected as $L = 100m$, $w_0 = 5mm$, $\varepsilon = 0.5$, $\rho_f = 1000kg/m^3$, $\mu = 10^{-3}Pa \cdot s$, and the boundary condition $\overline{q}$ is adjusted to give the desired Reynolds number. Reynolds numbers of $Re = 0.1$, 100, 3000, 5000 are considered. These correspond respectively to: the viscous regime, in which inertial forces are negligible; the weak inertial regime, in which flow is laminar but inertial forces are not negligible; the transitional regime, in which flow is transitioning between laminar and turbulent flows; and the turbulent regime in which flow is fully turbulent [41]. As the PPE is independent of time, only a single timestep is necessary to solve the pressure distribution, provided that the steady-state flux distribution is prescribed as the initial condition. The pressure distribution is determined with increasingly refined mesh size and the normalized root mean square error between the numerical and analytical pressures are calculated.

The convergence rates of the pressure and pressure gradient in the different regimes are illustrated in Figure 3.6. The pressure displays $O(\Delta x^2)$ convergence in all regimes, which is expected given the second-order accurate central differencing scheme that was used to discretize the PPE. The pressure gradient, which is reconstructed from the pressure using central differencing, displays an $O(\Delta x^{1.5})$ rate of convergence in all regimes except for the viscous regime, in which it exhibits an $O(\Delta x^2)$ rate of convergence. The linear viscous friction term dominates in the viscous regime, which may explain the higher rate of convergence, while the non-linear convection term dominates at higher Re.

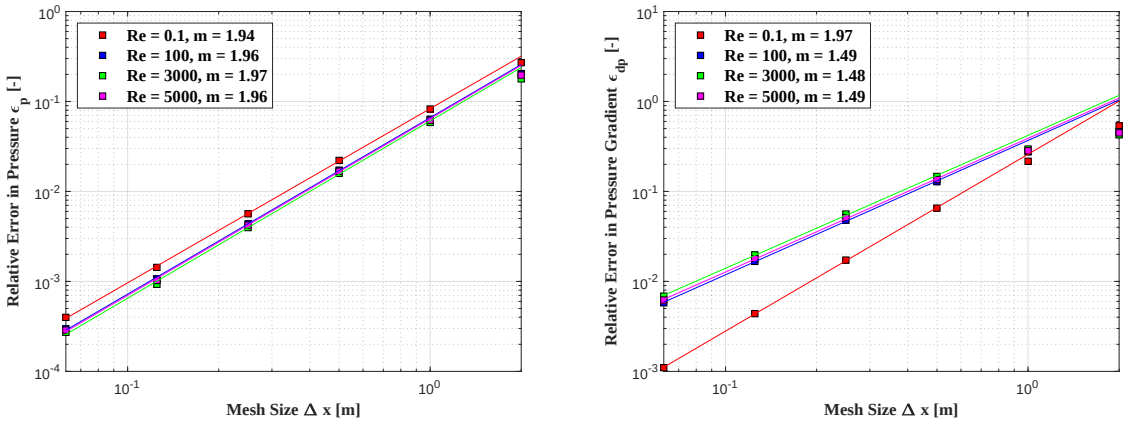

Figure 3.6: Convergence rates of pressure and pressure gradient with respect to space in four flow regimes. m is the rate of convergence, such that the algorithm displays $O(\Delta x^m)$ convergence with mesh refinement.

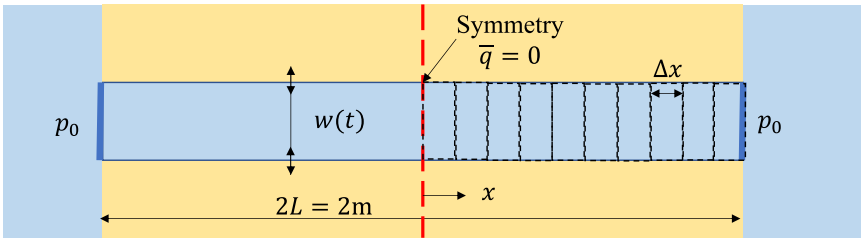

Figure 3.7: Domain for flow through a submerged channel with oscillating aperture.

3.7 Example: Transient Flow Through Oscillating Channel

Sections 3.5 and 3.6 examine flow cases in which the aperture field is static. This section examines the case of uniform moving aperture. The problem domain is illustrated in Figure 3.7. Consider the flow through a submerged channel of length $2L$ in which the aperture oscillates at a fixed frequency, Ω, and amplitude, ε, such that the aperture is given by $w = w_0(1 + \varepsilon \sin(\Omega t))$. The pressure at the outlets is fixed at $\overline{p} = p_0$ and the flux at the centerline must be zero due to symmetry. Fluid is forced in and out of the channel by continuity, and the pressure profile develops to accommodate the flow. Unlike previous examples, this example captures pressure and flux fields which vary in both time and space. In the laminar regime, the analytical solution to the GG22 model is

$$q(x,t) = -\dot{w}(t)x \quad \{0 \le x \le L\} \tag{3.49}$$

$$p(x,t) = p_0 + \left(\rho_f \left(\frac{\ddot{w}}{w} - 2\alpha\left(\frac{\dot{w}}{w}\right)^2\right) + \frac{12\mu}{w^3}\dot{w}\right)\frac{L^2}{2}\left(\left(\frac{x}{L}\right)^2 - 1\right) \quad \{0 \le x \le L\} \tag{3.50}$$

The properties of the fluid are selected as $\mu = 10^{-3} Pa \cdot s$ and $\rho_f = 1000 kg/m^3$. The properties of the aperture are selected as $w_0 = 10mm$, and $\varepsilon = 0.25$, which correspond to

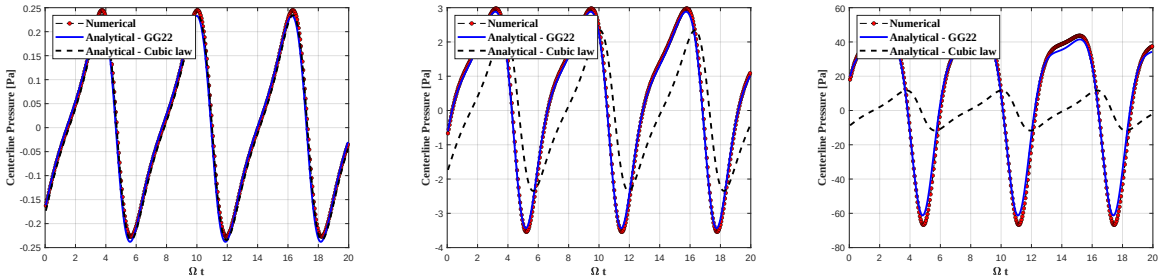

(a) $\Omega = 0.1\phi$ (b) $\Omega = \phi$ (c) $\Omega = 5\phi$

Figure 3.8: Comparison of numerical and exact solutions pressure at the centerline in a submerged channel with oscillating aperture. The numerical and exact solutions show excellent agreement at all three excitation frequencies, though error increases with the excitation frequency. The cubic law solution is also plotted.

a fundamental frequency of $\phi = 0.12s^{-1}$. The length of the domain is set at $1m$ and is chosen to restrict the maximum Reynold's number and ensure that the solution remains in the laminar regime where the analytical solution is valid. The numerical scheme is tested at three different excitation frequencies, $\Omega = 0.1\phi$, ϕ, 5ϕ. The domain is subdivided into 10 flux cells, and 400 timesteps are used in all three cases. The problem is simulated for a total time period of $20/\Omega$.

The pressure at the centerline of the domain for all three excitation frequencies is compared to the analytical solution in Figure 3.8. The numerical scheme shows excellent agreement with the analytical solution in all three regimes. The largest differences are observed in the case of $\Omega = 5\phi$, as the nonlinear convection terms become more important as the excitation frequency increases. Figure 3.8 also illustrates the cubic law analytical solution, showing how the inertial effects in the GG22 model lead to a departure from the cubic law solution as the excitation frequency increases.

3.8 Example: Travelling Aperture Wave

In this final example, a problem with moving non-uniform aperture is examined. The problem domain is illustrated in Figure 3.9.

Consider the flow between two equal head reservoirs which are connected by a fracture of length L. The fluid is initially at rest, at which point a travelling wave propagates along the fracture, as might be induced by a seismic event. The aperture is defined as $w = w_0\left(1 + \varepsilon \sin\left(\frac{2\pi n}{L}x + \Omega t\right)\right)$ in which n is the wave number, Ω is the wave frequency, and ε is the relative amplitude of the wave. The speed of the wave is given by $v = \Omega\lambda$, in which λ is the wavelength given by $\lambda = \frac{L}{n}$. The pressures at both ends of the fracture are fixed at $\overline{p} = p_0$. Unlike previous examples, an analytical solution is not readily available for the chosen boundary conditions.

The properties of the fluid are selected as $\mu = 10^{-3}Pa \cdot s$ and $\rho_f = 1000kg/m^3$. The properties of the aperture are selected as $w_0 = 0.5mm$, and $\varepsilon = 1/2000$, which correspond

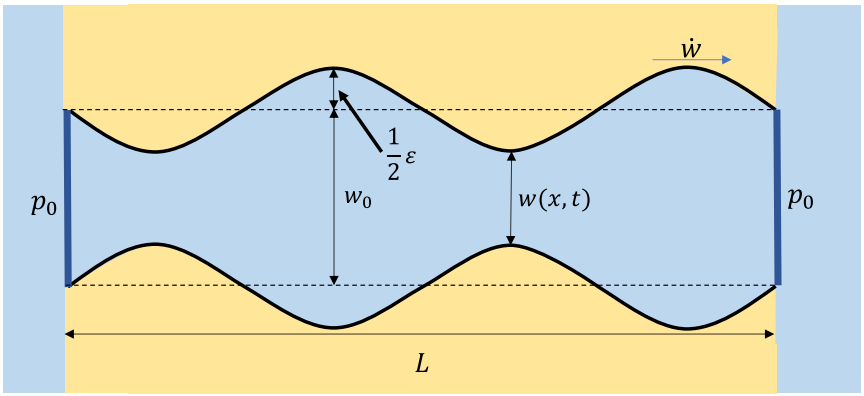

Figure 3.9: Domain for flow through a channel with a travelling aperture wave.

to a fundamental frequency of $\phi = 48s^{-1}$. The length of the domain is set to $1km$. The speed of the travelling wave is fixed at $v = 3km/s$, the approximate speed of a shear wave propagating through a granite rock mass, and wavelengths of $\lambda = 1,\ 0.5,\ 0.33, ..., 0.1km$ are examined ($n = 1,\ 2,\ 3, ..., 10$ respectively). These wavelengths correspond to wave frequencies of $\Omega = 3,\ 6,\ 9, ..., 30s^{-1}$. A mesh of 500 flux cells and 5000 timesteps are used in all cases. The problem is simulated for a total time period of $10\pi/\Omega$.

The results are illustrated in Figures 3.10. Figure 3.10a illustrates the spatial average flux over time and shows that the net fluid flux is in the negative direction, despite the wave travelling in the positive direction. This is attributed to the effects of continuity, as $q_{,x} = -\dot{w}$. The spatially averaged fluid flux demonstrates a dynamic steady-state solution, in which the fluid displays regular dynamic oscillations around a mean steady-state flux. The cubic law solutions do not display any oscillations, and the average flux is constant in time.

Figure 3.10b shows the distribution of aperture and flux for $n = 2$ throughout the fracture at the final timestep. The spatial distribution of flux is governed primarily by the wavelength. Fluid is drawn towards the crest of an aperture wave, creating positive flow through the troughs and negative flow under the peaks. Two stagnation points are created in each wavelength which directly align with the the inflection points of the aperture wave.

Figure 3.10c illustrates the pressure and flux distribution according to both models through the fracture for $n = 2$. The spatial distribution of fluxes is similar between the two models, but there is a small phase-shift which is not visible at the current scale, as the spatial variations in flux are much greater than the spatial average flux. The selected properties lead to a maximum Reynolds number of 750. The maximum flux is proportional to aperture, amplitude, and wave speed, but is independent of wavelength. The GG22 pressures demonstrate larger peak pressures and significant phase shifts due to the inertial effects. The maximum pressure is proportional to the wavelength, wave speed, amplitude, and the inverse square of the aperture.

Figure 3.10d illustrates the relationship between the maximum pressure in the fracture over time and the mean steady-state spatial average flux as functions of the wavelength. While the cubic law predicts that the pressure has a linear relationship with wavelength,

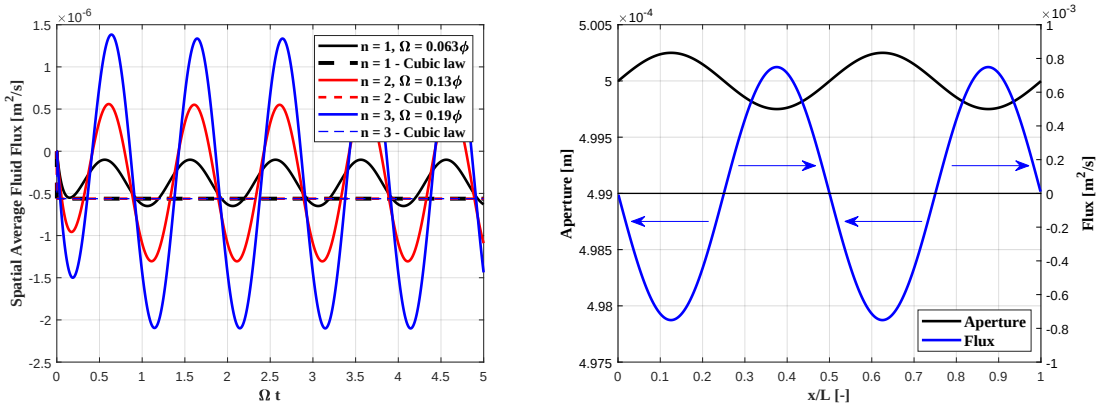

(a) Spatial average fluid flux at different wavelengths

(b) Spatial distribution of aperture and flux for $n = 2$

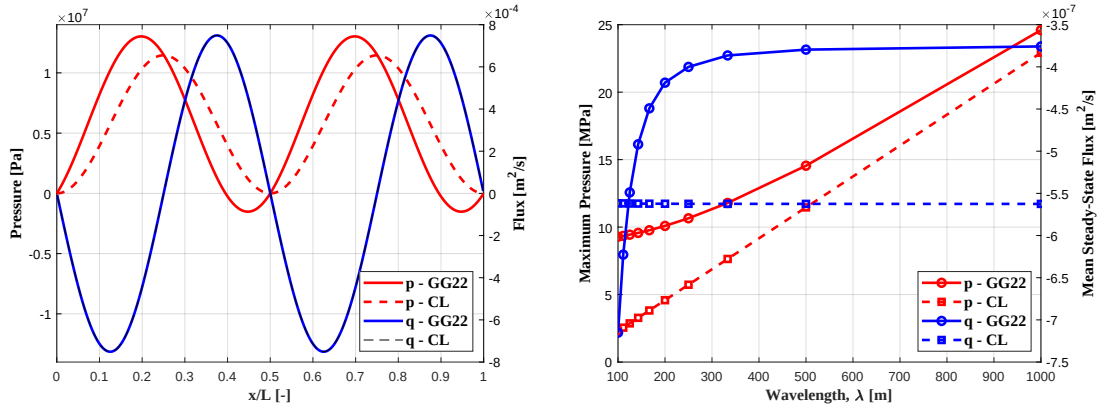

(c) Spatial distribution of pressure and flux for $n = 2$

(d) Mean steady-state spatial average flux and maximum pressure as a function of wavelength

Figure 3.10: Pressure and flux behaviours of the fluid for a travelling aperture wave with fixed velocity but varying wavelengths. In Figure 3.10b, vectors indicate the direction of flow.

and the mean flux is independent of wavelength, the more complex GG22 model shows that both variables have non-linear relationships to wavelength. At long wavelengths, higher pressures are required to overcome inertial forces and on average produce less net fluid movement. At shorter wavelengths, greater mean fluxes are produced than those predicted by the cubic law.

3.9 Conclusions

In this chapter, a multi-step explicit finite volume method to solve the one-dimensional GG22 equations has been developed and verified. The method is based on deriving a Poisson equation for pressure, a technique commonly used in explicit methods for the Navier-Stokes but adapted for the idiosyncrasies of the GG22 model. The method is verified with three examples and demonstrates the expected rates of convergence with timestep and mesh refinement. The numerical method is then applied to a travelling aperture wave problem between two reservoirs which illustrates new fluid phenomena not captured by Poiseuille flow. These phenomena include increased fluid pressures, decreased fluxes, sensitivity to excitation wavelength and frequency, and phase-shifts in the fluid response.

This numerical model illustrates the different fluid behaviours that arise in response to excitation through the aperture or otherwise, but it does not capture the effects that the fluid has on the aperture. The next step in our investigation is thus to develop a hydro-mechanically coupled model to examine the mutual interaction between rock mass deformation and fracture flow.

Chapter 4

Solving the Hydro-Mechanically Coupled GG22 Model

4.1 Introduction

In Chapter 3 we developed a numerical method to solve the GG22 model in which the aperture was uncoupled from the fluid response. In this chapter, we wish to examine the combined hydro-mechanical response of a coupled system. While there are many different physical effects which can influence fracture propagation, the purpose of this model is to examine the influence of a new fluid model. With this context, we focus on developing a simulator with the minimum number of physical effects required to examine the hydro-mechanical response. Thus, this chapter presents the development and verification of a coupled numerical hydro-mechanical model with a cohesive fracture zone and examines the application of this model to the propagation of a planar hydraulic fracture.

There are many hydro-mechanically coupled models for hydraulic fracture propagation based on Poiseuille flow using analytical, semi-analytical, and numerical methods. Analytical methods based on the fracture tip asymptotics typically rely low permeability rock masses with leak-off and linear elastic fracture mechanics [5, 7]. Numerical methods allow for more adaptability in the physics captured and have been extended to include proppant transport [13, 60], porous media [61, 62], and rock mass nonlinearities like nonlocal plasticity [63, 64] among many others. Advancements in hydraulic fracturing simulations have included improvements in the numerical techniques, including eXtended finite element methods (XFEM) [19, 65, 66, 56], boundary integral methods [67, 68], and phase-field models [69, 70] among others. The efforts focused on improving the physics of fluid flow consist primarily of nonlinear fluid rheologies, rather than addressing the underlying issues of Poiseuille flow. There is a limited number of studies which address fluid inertia [27], but they have relied on physically inconsistent approximations, which were the best available options at the time. Turbulent flow is a more common topic than inertia in the context of hydraulic fracture propagation [26, 71, 72, 73]. The treatment of turbulence in the GG22 model is consistent with these studies, in that the laminar linear friction term is

replaced with a nonlinear quadratic friction term, but the interactions of turbulence with fluid inertia have been completely neglected.

In order to develop new numerical methods to solve the GG22 equations, we must consider discretization in space, discretization in time, and solution methodology. Previous hydraulic fracturing studies provide invaluable guidance on which methods have favourable properties, but the GG22 model is accompanied by unique challenges [74]. In terms of spatial discretization, as established in Chapter 3, the GG22 model is similar in form to the Navier-Stokes equations but lacks a diffusive term, thus lending itself naturally to the finite volume method (FVM) [74]. The finite element method (FEM) is the most common method adopted for the equilibrium equation, and is thus adopted here. In terms of discretization in time and solution methodology, it has been well-established that staggered or sequential solution schemes for hydraulic fracturing can be unstable, and the accuracy of the solution is dependent on the order in which the fields are solved [19, 75]. Attempting to add mechanical coupling to the explicit method develop in Chapter 3 yields similar results and the explicit method appears to lack stability. Implicit time integration is more stable than explicit time integration, and monolithic solution algorithms in the context of hydraulic fracturing have been shown to be both more robust and more accurate than their sequential counterparts [13, 19]. Therefore, in this chapter we adopt and develop a monolithic implicit FEM - FVM scheme which couples the GG22 flow model to the mechanical deformation of the rock mass.

Section 4.2 presents the governing equations of the fractured rock mass which are coupled with the GG22 equations. Next, Section 4.3 presents a coupled FEM-FVM discretization scheme for the system. Section 4.4 examines solution methodology and determines how best to solve the system of discretized nonlinear equations. In Section 4.5, the coupled model is applied to the flow problem of a submerged channel between oscillating elastic plates. This example problem serves as verification and illustrates the characteristics types of behaviour which arise from inertia in a hydro-mechanically coupled fracture system. Lastly, in Section 4.6, the GG22 model is applied to one-dimensional planar hydraulic fractures in the viscous- and toughness-dominant fracture regimes, and the relative importance of inertia and turbulence are established in this context.

4.2 Governing Equations of a Rock Mass with Propagating Fractures

Consider an impermeable rock mass under in-situ stresses in which fluid flows through discrete fractures which may propagate, as illustrated in Figure 4.1a. The rock mass domain, Ω_s, is considered as a two-dimensional body. The apertures are small relative to their length, such that the differences in pressure and fluid velocity are small across the fracture aperture, and the fluid domain, Ω_f may be approximated as a lower dimensional body, such that $\Omega_f \equiv \Gamma_c$ in which Γ_c is the solid fracture boundary.

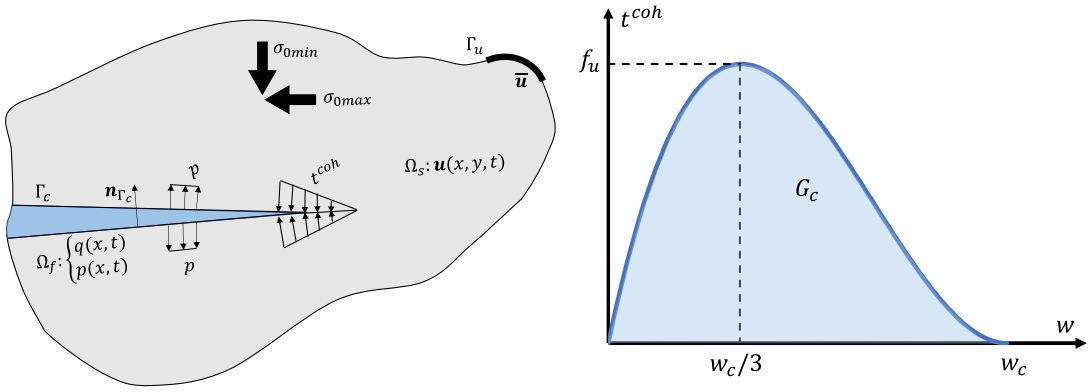

(a) Mathematical Domain. (b) Cubic cohesive traction-separation law.

Figure 4.1: Mathematical domain for an impermeable rock mass under in-situ stress with discrete fluid-filled fractures. Fracture propagation is controlled by the fracture process zone ahead of the fracture tip which follows a cubic traction-separation law.

The rock mass is modeled as a quasi-static impermeable elastic medium. Deformation of the rock mass is governed by the equilibrium equation,

$$0 = \nabla \cdot \boldsymbol{\sigma}(\boldsymbol{u}) \text{ on } \Omega_s \tag{4.1}$$

$$\boldsymbol{\sigma} - \boldsymbol{\sigma}_0 = \mathbb{C} : \varepsilon \tag{4.2}$$

in which $\boldsymbol{u}(x,y,t)$ is the rock mass deformation, $\boldsymbol{\sigma}$ is the Cauchy stress tensor, $\boldsymbol{\sigma}_0$ is the in-situ stress tensor, $\mathbb{C}$ is the elasticity tensor, and ε is the linear strain tensor. Within the rock mass domain are discrete fractures which may propagate. The fractures are defined by an aperture which may change as a result of deformation in the rock mass, such that

$$w = w_0 + \boldsymbol{n}_{\boldsymbol{\Gamma_c}} \cdot \boldsymbol{u}\Big|_{\Gamma_c} \tag{4.3}$$

in which w_0 is some initial residual aperture that might arise from contact between non-uniform fracture faces and asperities. The propagation of the fractures is modelled using a cohesive-zone model. A cubic traction-separation law [76] is adopted, as illustrated in Figure 5.1b. The traction-separation law is defined as a function of the aperture according to

$$t^{coh}(w) = \begin{cases} \frac{27}{4} f_u \Delta(1 - 2\Delta + \Delta^2), & w \leq w_c \\ 0, & w > w_c \end{cases} \quad , \; \Delta = \frac{w}{w_c} \tag{4.4}$$

$$w_c = \frac{48}{27} \frac{G_c}{f_u} \tag{4.5}$$

in which f_u is the cohesive strength of the rock mass, G_c is the fracture energy, and w_c is the critical aperture which defines the boundary between the cohesive zone and the physical fracture tip. Fracture propagation in a cohesive-zone model is significantly influenced by fluid lag and vaporization behind the crack tip [77, 78]. This effect has been neglected in

favour of simplifying the model physics and isolating the effects of the new fluid model but should be otherwise included.

Fluid flows through the fractures, exerting pressure, p on the rock mass, while cohesive tractions, t^{coh} resist fracture opening, such that the rock mass is subjected to the boundary conditions

$$\boldsymbol{\sigma} \cdot \boldsymbol{n}_{\Gamma_c^{\pm}} = (-p + t^{coh})\mathbf{I} \cdot \boldsymbol{n}_{\Gamma_c^{\pm}} \text{ on } \Gamma_c^{\pm} \tag{4.6}$$

in which $\boldsymbol{n}_{\Gamma_c^{\pm}}$ is the corresponding normal to the positive or negative face of the fracture, $\Gamma_c^{\pm}$.

4.3 Discretization

4.3.1 Quasi-static rock mass equilibrium

The rock mass is discretized using the finite element method. The weak form of the equilibrium equation in the rock mass is presented as

$$\int_{\Omega_s} \nabla \delta \boldsymbol{u} : \boldsymbol{\sigma} d\Omega + \int_{\Gamma_c} \delta \mathbf{u} \cdot p\mathbf{I} \cdot \boldsymbol{n}_{\Gamma_c} d\Gamma - \int_{\Gamma_c} \delta \mathbf{u} \cdot t^{coh}\mathbf{I} \cdot \boldsymbol{n}_{\Gamma_c} d\Gamma = 0 \tag{4.7}$$

where the test function, $\delta \boldsymbol{u}$, is subject to the restriction $\delta \boldsymbol{u} = 0$ on Γ_u. To develop a set of discrete equations, we introduce the following finite element approximations.

$$\boldsymbol{u} = \mathbf{N}\mathbf{u} \tag{4.8}$$
$$\{\boldsymbol{\varepsilon}\} = \mathbf{B}\mathbf{u} \tag{4.9}$$
$$\{\boldsymbol{\sigma}\} = \mathbf{D}\mathbf{B}\mathbf{u} \tag{4.10}$$
$$p = \boldsymbol{\psi}\mathbf{p} \tag{4.11}$$

in which $\{\boldsymbol{\varepsilon}\}$ and $\{\boldsymbol{\sigma}\}$ are the strain and stress in Voigt form, and $\mathbf{N}, \mathbf{B}$, and $\mathbf{D}$ are the standard finite element shape function, shape function gradient, and elasticity matrices. $\boldsymbol{\psi}$ is a shape function to map the discretized pressure, $\mathbf{p}$, onto the rock mass. $\mathbf{u}$ and $\mathbf{p}$ are vectors of nodal displacements and pressures respectively. In the following section, fluid pressure is discretized using the finite volume method, creating a piecewise-constant approximation of the pressure field, p. The pressure cell centroids align with the rock mass nodes, therefore a Heaviside approximation is used to project the pressure onto the rock mass.

By substituting the discrete approximations into the weak form of the governing equation, the following residual and forcing vectors can be defined.

$$\mathbf{R}_u = \mathbf{F}_u + \mathbf{F}_p + \mathbf{F}_h = 0 \tag{4.12}$$

$$\mathbf{F}_u = \int_{\Omega_s} \mathbf{B}^\top \mathbf{D}\mathbf{B} d\Omega \mathbf{u} \tag{4.13}$$

$$\mathbf{F}_p = \int_{\Gamma_c} \mathbf{N}^\top \boldsymbol{n}_{\Gamma_c} \boldsymbol{\psi} d\Gamma \mathbf{p} \tag{4.14}$$

$$\mathbf{F}_h = -\int_{\Gamma_c} \mathbf{N}^\top t^{coh}(w) \mathbf{I} \cdot \boldsymbol{n}_{\Gamma_c} d\Gamma \tag{4.15}$$

A discrete form of the aperture can also be defined, such that

$$w = w_0 + \boldsymbol{n}_{\boldsymbol{\Gamma_c}} \cdot \boldsymbol{u}\Big|_{\Gamma_c} \tag{4.16}$$

$$w = w_0 + \boldsymbol{n}_{\boldsymbol{\Gamma_c}} \cdot \left(\mathbf{N}\Big|_{\Gamma_c^+} - \mathbf{N}\Big|_{\Gamma_c^-} \right) \mathbf{u} \tag{4.17}$$

$$w = w_0 + \boldsymbol{n}_{\boldsymbol{\Gamma_c}} \cdot [\![\mathbf{N}]\!] \mathbf{u} \tag{4.18}$$

in which w_0 is an equivalent initial residual aperture which arises from an initial fracture permeability k_0. The initial permeability and residual aperture are related according to the Poiseuille flow relationship, $w_0 = \sqrt{12 k_0}$.

4.3.2 Conservation of fluid momentum

The fluid is discretized with the finite volume method on a staggered grid, as illustrated in Figure 4.2. The conservation of fluid momentum is discretized over the flux cells by integrating across the cell i from local face $x_{i,1}$ to local face $x_{i,2}$. For a discretized field τ in a given cell i, τ_i denotes τ evaluated at the cell centroid, whilst $\tau_{i,j}$ denotes τ interpolated to the face j of cell i.

$$\int_{x_{i,1}}^{x_{i,2}} \frac{\partial q}{\partial t} dx + \int_{x_{i,1}}^{x_{i,2}} \frac{\partial}{\partial x} \left(\alpha \frac{q^2}{w} \right) dx + \int_{x_{i,1}}^{x_{i,2}} \frac{w}{\rho_f} \frac{\partial p}{\partial x} dx + \int_{x_{i,1}}^{x_{i,2}} \frac{1}{2} \frac{f_D}{w^2} q^2 dx = 0 \tag{4.19}$$

Each term is integrated individually. First, the transient term integrates as

$$\int_{x_{i,1}}^{x_{i,2}} \frac{\partial q}{\partial t} dx = \Delta x \dot{q}_i \tag{4.20}$$

$$\dot{q}_i = \frac{1}{2\Delta t} \left(3q_i^n - 4q_i^{n-1} + q_i^{n-2} \right) \tag{4.21}$$

in which (4.21) is a second order backwards Euler approximation of the rate of flux change.

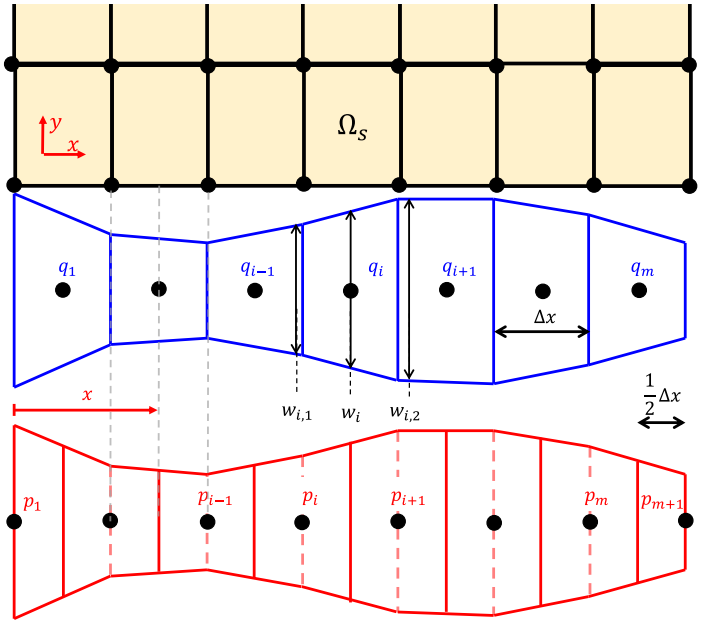

Figure 4.2: Schematic diagram of fluid and solid meshes. The solid mesh (top) consists of two-dimensional finite elements while the fluid mesh consists of one-dimensional staggered finite volumes of non-constant width. The flux cells (middle), q_i, are aligned with the edges of the domain, while the pressure cells (bottom), p_i are staggered with a half-cell at each edge of the domain. The finite volume cells are associated with apertures, w_i, controlled by the deformation of the rock mass.

Next, the convective term integrates as

$$\int_{x_{i,1}}^{x_{i,2}} \frac{\partial}{\partial x}\left(\alpha\frac{q^2}{w}\right)dx = \left(\alpha\frac{q^2}{w}\right)\Bigg|_{x_{i,1}}^{x_{i,2}} \tag{4.22}$$

$$= \left[\frac{\alpha(q_{i,2})}{w_{i,2}}(q_{i,2})^2 - \frac{\alpha(q_{i,1})}{w_{i,1}}(q_{i,1})^2\right] \tag{4.23}$$

The second order QUICK scheme is used to interpolate the fluxes at the cell faces.

Next, the friction term integrates as

$$\int_{x_{i,1}}^{x_{i,2}} \frac{1}{2}\frac{f_D}{w^2}q^2 dx \approx \Delta x \frac{f_D(q_i)}{2(w_i)^2}(q_i)|q_i| \tag{4.24}$$

based on the finite volume assumption that both aperture and flux are approximately constant across the cell.

Last, the pressure term can be approximated as

$$\int_{x_{i,1}}^{x_{i,2}} \frac{w}{\rho_f}\frac{\partial p}{\partial x}dx \approx \frac{1}{\rho_f}\overline{w}\overline{\frac{\partial p}{\partial x}}\Delta x = \frac{w_i}{\rho_f}\frac{p_{i+1}-p_i}{\Delta x}\Delta x = \frac{w_i}{\rho_f}(p_{i+1}-p_i) \tag{4.25}$$

based on the assumption that aperture and pressure gradient are approximately constant across the cell.

Thus the following residual and forcing vectors can be defined for the conservation of fluid momentum.

$$\mathbf{R}_m = 0 = \mathbf{F}_t + \mathbf{F}_c + \mathbf{F}_{mp} + \mathbf{F}_f \tag{4.26}$$

$$(F_t)_i = \frac{\Delta x}{2\Delta t}\left(3q_i^n - 4q_i^{n-1} + q_i^{n-2}\right) \tag{4.27}$$

$$(F_c)_i = \left[\frac{\alpha(q_{i,2})}{w_{i,2}}(q_{i,2})^2 - \frac{\alpha(q_{i,1})}{w_{i,1}}(q_{i,1})^2\right] \tag{4.28}$$

$$(F_{mp})_i = \frac{w_i}{\rho_f}(p_{i+1}-p_i) \tag{4.29}$$

$$(F_f)_i = \Delta x \frac{f_D(q_i)}{2(w_i)^2}(q_i)|q_i| \tag{4.30}$$

4.3.3 Conservation of fluid mass

Last, the conservation equation is discretized over the pressure cells by integrating across the cell from local face $x_{i,1}$ to local face $x_{i,2}$.

$$\int_{x_{i,1}}^{x_{i,2}} \frac{\partial w}{\partial t} dx + \int_{x_{i,1}}^{x_{i,2}} \frac{\partial q}{\partial x} dx = 0 \tag{4.31}$$

$$\Delta x \frac{\partial w_{i,1}}{\partial t} + q \Big|_{x_{i,1}}^{x_{i,2}} = 0 \tag{4.32}$$

$$\Delta x \frac{\partial w_{i,1}}{\partial t} + (q_i - q_{i-1}) = 0 \tag{4.33}$$

$$\dot{w}_{i,1} = \frac{1}{2\Delta t} \left(3w_{i,1}^n - 4w_{i,1}^{n-1} + w_{i,1}^{n-2} \right) \tag{4.34}$$

in which aperture is assumed to be approximately constant over each flux cell for the purposes of integration, and (4.34) is a second order backwards Euler approximation of the rate of flux change.

Thus the following residual and forcing vectors can be defined for the conservation of fluid mass. These forcing vectors are applicable to all interior pressure cells, but special treatment is required for the half-width boundary cells.

$$\mathbf{R}_c = 0 = \mathbf{F}_w + \mathbf{F}_q \tag{4.35}$$

$$(F_w)_i = \frac{\Delta x}{2\Delta t} \left(3w_{i-\frac{1}{2}}^n - 4w_{i-\frac{1}{2}}^{n-1} + w_{i-\frac{1}{2}}^{n-2} \right) \tag{4.36}$$

$$(F_q)_i = (q_i - q_{i-1}) \tag{4.37}$$

4.3.4 Summary of discretized system and residuals

The fully discretized system of equations is thus

$$\mathbf{R} = \begin{bmatrix} \mathbf{R}_u \\ \mathbf{R}_m \\ \mathbf{R}_c \end{bmatrix} = \begin{bmatrix} \mathbf{F}_u + \mathbf{F}_p + \mathbf{F}_h \\ \mathbf{F}_t + \mathbf{F}_c + \mathbf{F}_{mp} + \mathbf{F}_f \\ \mathbf{F}_w + \mathbf{F}_q \end{bmatrix} = \mathbf{0} \tag{4.38}$$

$$\mathbf{F}_u = \int_{\Omega_s} \mathbf{B}^\top \mathbf{D}\mathbf{B} d\Omega \mathbf{u} \tag{4.39}$$

$$\mathbf{F}_p = \int_{\Gamma_c} \mathbf{N}^\top \boldsymbol{n}_{\Gamma_c} \boldsymbol{\psi} d\Gamma \mathbf{p} \tag{4.40}$$

$$\mathbf{F}_h = -\int_{\Gamma_c} \mathbf{N}^\top t^{coh}(w) \mathbf{I} \cdot \boldsymbol{n}_{\Gamma_c} d\Gamma \tag{4.41}$$

$$(F_t)_i = \frac{\Delta x}{2\Delta t}\left(3q_i^n - 4q_i^{n-1} + q_i^{n-2}\right) \tag{4.42}$$

$$(F_c)_i = \left[\frac{\alpha(q_{i,2})}{w_{i,2}}(q_{i,2})^2 - \frac{\alpha(q_{i,1})}{w_{i,1}}(q_{i,1})^2\right] \tag{4.43}$$

$$(F_{mp})_i = \frac{w_i}{\rho_f}(p_{i+1} - p_i) \tag{4.44}$$

$$(F_f)_i = \Delta x \frac{f_D(q_i)}{2(w_i)^2}(q_i)|q_i| \tag{4.45}$$

$$(F_w)_i = \frac{\Delta x}{2\Delta t}\left(3w_{i,1}^n - 4w_{i,1}^{n-1} + w_{i,1}^{n-2}\right) \tag{4.46}$$

$$(F_q)_i = (q_i - q_{i-1}) \tag{4.47}$$

4.4 Solution Methods

In this section, the performance of several different solution methodologies to solve the set of discretized equations are considered.

To solve a set of non-linear coupled discretized equations, one may adopt a staggered approach (in which each field or subset of fields are solved sequentially), or a monolithic approach (in which all fields are solved simultaneously). In both approaches, iteration is required to converge to a solution. Staggered approaches are often considered in multi-physics problems, as they allow a user to take advantage of powerful preexisting solvers for each set of physics. Staggered solutions typically require more iterations to converge than a monolithic solver for the trade-off of easier implementation and adaptability. Monolithic solutions are often more cumbersome to implement and require the derivation and implementation of a large and complex Jacobian matrix that is unique to each coupled problem, but typically converge faster than sequential methods. It has been well-established in the context of porous media [79, 80] and hydraulic fracturing simulation [75, 19] that naive staggering schemes lack robustness and do not converge to a solution. Complex splits are required to overcome the instabilities [19]. Staggering schemes are further complicated in the GG22 model, since much like the Navier-Stokes equations from which it is derived,

there is no governing equation which directly controls the pressure. While techniques do exist to create a governing equation for pressure, such as previously adopted by the authors in developing an explicit finite volume scheme to solve the GG22 model [74], attempts to couple said explicit scheme with rock mass deformation resulted in divergence issues consistent with previous studies of similar problems. The Navier-Stokes equations are regularly solved using sequential schemes, so the difficulty with fracture flow arises from coupling the flow equations with the equilibrium equations and fracture propagation in the rock mass. Monolithic approaches have thus become the method of choice for hydraulic fracturing problems as they are consistently demonstrated to be more robust and converge where staggered solutions diverge, and thus a monolithic method is adopted here.

4.4.1 Newton-Raphson method

Having adopted a monolithic approach, the natural choice of solution method is to adopt the Newton-Raphson method. First, the vector of nodal degrees of freedom $\mathbf{d}$ for iteration k is defined as

$$\mathbf{d}_k = \begin{bmatrix} \mathbf{u} \\ \mathbf{q} \\ \mathbf{p} \end{bmatrix}_k = \mathbf{d}_{k-1} + \Delta\mathbf{d}_k \tag{4.48}$$

in which $\Delta\mathbf{d}_k$ is the solution increment. The solution increment is determined by solving the linearized the system of non-linear equations,

$$\mathbf{J}_k \Delta\mathbf{d}_k + \mathbf{R}_k = \mathbf{0} \tag{4.49}$$

in which $\mathbf{J}_k$ is the Jacobian / tangent matrix. When expanded, the Jacobian takes the form

$$\mathbf{J}_k = \begin{bmatrix} \frac{\partial \mathbf{R}_u}{\partial \mathbf{u}} & \frac{\partial \mathbf{R}_u}{\partial \mathbf{q}} & \frac{\partial \mathbf{R}_u}{\partial \mathbf{p}} \\ \frac{\partial \mathbf{R}_m}{\partial \mathbf{u}} & \frac{\partial \mathbf{R}_m}{\partial \mathbf{q}} & \frac{\partial \mathbf{R}_m}{\partial \mathbf{p}} \\ \frac{\partial \mathbf{R}_c}{\partial \mathbf{u}} & \frac{\partial \mathbf{R}_c}{\partial \mathbf{q}} & \frac{\partial \mathbf{R}_c}{\partial \mathbf{p}} \end{bmatrix}_k = \begin{bmatrix} \mathbf{K}_{uu} & \mathbf{0} & \mathbf{K}_{up} \\ \mathbf{K}_{mu} & \mathbf{K}_{mq} & \mathbf{K}_{mp} \\ \mathbf{K}_{cu} & \mathbf{K}_{cq} & \mathbf{0} \end{bmatrix}_k \tag{4.50}$$

The resulting system Jacobian is non-symmetric and non-positive definite with zeros along its diagonal. The system is still rank-independent and therefore invertable. The definitions of the various component matrices are documented in Appendix C.

The Newton-Raphson method has been shown to work well for the two-field ($u-p$) hydro-mechanical Poiseuille flow problem [19]. The Newton-Raphson method also works well for the three-field ($u-q-p$) hydro-mechanical GG22 model in problems that are not overly stiff (e.g. large initial apertures or cohesionless fractures), and in such problems often demonstrates even better convergence behaviour than the two-field model because the harsh cubic non-linearity is balanced by inertial terms. However, the hydro-mechanical GG22 model becomes problematic for stiff problems, and may encounter severe convergence issues. Whereas in the Poiseuille flow problem there is a direct feedback between pressure and deformation, the three-field model passes that feedback through the flux which must simultaneously satisfy both the conservation of momentum and the conservation of mass. Consider for example, a hydraulic fracturing problem where the solution contains a monotonic positive rate of aperture growth ($\dot{w} > 0, q_{,x} < 0 \forall t$). Suppose that in one iteration,

the unconverged aperture is updated such that $\dot{w}_k < 0$, then in the next iteration the flux is updated to satisfy the the continuity equation, such that $(q_{,x})_{k+1} > 0$. This will then reverberate into the pressure via the momentum equation then back into the rock mass, moving the solution away from the radius of convergence and often causing the solution to diverge. Furthermore, the relationships are strongly two-way coupled, so a positive flux gradient will equally encourage the solution towards a negative rate of aperture change. While these issues can in part be rectified with strategic initialization in each timestep, additional measures to improve robustness are required.

4.4.2 Aitken relaxation

The first measure to adopt is Aitken's Δ^2 relaxation between iterations. Aitken relaxation was originally developed to improve the rate of convergence of a linearly converging series by extrapolating the solution based on the previous two solution steps [81]. It is computationally inexpensive and easy to implement while providing invaluable improvements in robustness and convergence in both staggered and monolithic schemes [34]. Care must be taken when implementing Aitken's relaxation, as the relaxation coefficient, ω, is only meaningful for a field which demonstrates an approximately linear rate of convergence. In our case, ω is only a function of the displacements, $\mathbf{u}$, but the whole solution vector is updated according to ω. Using for example the flux, which may oscillate wildly between iterations especially outside of the radius of convergence, does not improve the rate of convergence nor robustness of the solution scheme. Aitken relaxation is implemented according to:

1. Set $\mathbf{d}'_{k+1} = \mathbf{d}_k + \Delta\mathbf{d}_k$
2. Calculate the relaxation parameter, $\omega_k(\mathbf{u})$ [81]

$$\omega_k = -\omega_{k-1}\frac{\Delta\mathbf{u}_{k-1}^{\top}(\Delta\mathbf{u}_k - \Delta\mathbf{u}_{k-1})}{|\Delta\mathbf{u}_k - \Delta\mathbf{u}_{k-1}|^2} \tag{4.51}$$

3. Update the current solution guess with the relaxation parameter

$$\mathbf{d}_{k+1} = (1-\omega_k)\mathbf{d}_k + \omega_k\mathbf{d}'_{k+1} \tag{4.52}$$

4. Resume the regular Newton-Raphson procedure.

4.4.3 Line Search

The second measure introduced is to replace the Newton-Raphson procedure with a steepest-descent line-search procedure. A step factor $\gamma \leq 1$ is introduced to the update (4.48) in each iteration according to

$$\mathbf{d}_k = \mathbf{d}_{k-1} + \gamma\Delta\mathbf{d}_k \tag{4.53}$$

It is well-known that Newton-Raphson provides a quadratic rate of convergence within the radius of convergence while line-search only provides a linear rate of convergence.

However, the quadratic rate of convergence is not recovered in practice as coupled fracture flow problems are generally non-smooth. Second, although the line-search provides a slower rate of convergence, this is improved by Aitken relaxation and under the theoretical ideal circumstances, the combination of line-search with Aitken relaxation recovers the same quadratic rate of convergence as Newton-Raphson as $\omega = 1/\gamma$ inside the Newton-Raphson radius of convergence. Third is robustness; for a sufficiently stiff non-smooth problem, the differences between each iteration are large. By damping the steps with the step factor γ, the solution is more likely to move monotonically towards a converged solution. Consider for example the one-dimensional root-finding problem for $\ln(x) = 0, x \in \mathbb{R}$. It is easy to show that Newton-Raphson converges to the solution $x = 1$ for an initial guess x_0 in the range $0 < x_0 < e^1$. At $x_0 \geq e^1$, the following iteration $x_1 < 0$ and the solution does not converge. Repeating the problem with a line-search procedure finds that the radius of convergence is $0 < x_0 < e^{1/\gamma}$, where $e^{1/\gamma} > e^1$. Thus, adopting a line-search procedure over a Newton-Raphson procedure can produce large improvements in robustness for non-smooth problems.

4.4.4 Improvement in convergence rate

The combined effectiveness of these measures to improve robustness is illustrated in Figure 4.3. The norm of the residuals are plotted for a typical small timestep in a stiff hydraulic fracturing problem such as considered in Section 4.6. The pure Newton-Raphson method diverges in seven iterations. The addition of Aitken relaxation improves the robustness and allows the timestep to converge in 50 iterations. The use of line search results in significant improvements in the number of iterations required to converge, and the determined optimal step factor of $\gamma = 0.8$ reduces the number of iterations from 50 to 27.

The characteristic residuals curves do not display a constant rate of convergence, instead showing plateaus followed by periods of rapid decrease in the residuals. Figure 4.4 illustrates why this behaviour is observed by examining each of the residuals and the Aitken relaxation parameter for the optimal γ. The plateaus in the residual curves correspond to periods where $\omega = 10^{-3}$, as ω has been limited to the range $10^{-3} \leq \omega \leq 10$. Equation (4.51) is not restricted to producing $\omega > 0$ and a negative Aitken parameter indicates that the solution is moving away from the solution to which the previous iterations had been converging. While allowing a negative Aitken parameter can sometimes improve convergence, in a multi-physics problem where the parameter is based on only a single field, all the fields would take a step in the opposite direction of the steepest descent, and allowing too large a negative parameter may produce poor solution predictions in the other fields which then delay or prevent convergence. How large a negative parameter is too large is not an easy question to answer, and is likely not constant throughout the simulation. Therefore, it is generally advisable to restrict $\omega > 0$. An $\omega > 0$ that is too large produces similar issues, so it is advisable to apply an upper bound. However, applying too small of an upper bound can also delay convergence, so it is more difficult to provide guidance on the upper bound. It can be shown that for a linearly converging series with a steepest descent line search, Aitken relaxation will produce $\omega = 1/\gamma$. However, for non-smooth problems it is very likely to encounter relaxation parameters beyond $1/\gamma$, so an upper

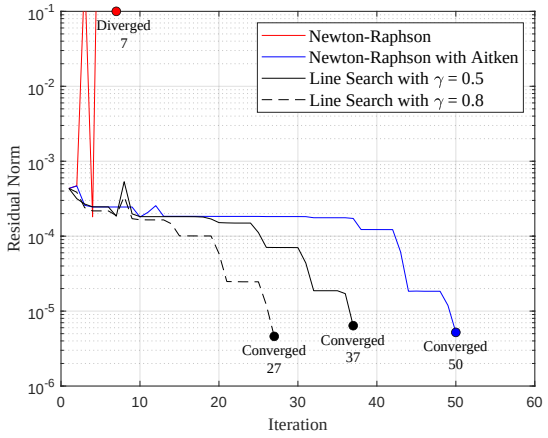

Figure 4.3: Comparison of the convergence behaviour of various solution methods. Convergence of a typical timestep is considered for a viscous-dominant hydraulic fracturing problem as considered in Section 4.6. Methods are compared for a single small timestep of $\Delta t = 0.1s$ at $10s$ into the simulation. Aitken's Δ^2 parameter is limited to the range $10^{-3} \leq \omega \leq 10$. A line search parameter of $\gamma = 0.8$ has been determined to be the optimal step size which for convergence at this time in the simulation.

bound of at least $\omega \geq 1/\gamma$ is recommended. Last, it can be observed that even when the solid and momentum residuals are plateaued, such small increments can still produce orders of magnitude change in the continuity residual $\mathbf{R}_c$, thus demonstrating the stiffness of the problem.

4.4.5 Optimal line search parameter

The Newton-Raphson method is also a steepest-descent line search with $\gamma = 1$. Thus, the three converged residual curves in Figure 4.3 imply the existence of an optimal γ that results in a minimum number of iterations to converge. Figure 4.5 illustrates the relationship between step factor and the number of iterations required to converge for the same timestep illustrated in Figure 4.3. The relationship is non-monotonic and more than one local minimum is observed. Furthermore, while all tested value of γ converged for this particular timestep, it is often the case that many values of γ do not converge. We are able to demonstrate that in practice we can determine a viable γ using an adapative scheme to find the local minimum which produces significant improvements in the convegence behaviour and computation time.

We adopt a simple procedure to experimentally find a local minimum step factor by testing γ in fixed increments (e.g., $\Delta\gamma = 0.05$) in the direction of decreasing iterations until a local minimum (which may or may not also be the global) is found. The optimal γ is reevaluated at set intervals throughout the simulation (e.g. every 50 time steps) and based on performance metrics (e.g., last 4 time steps all took > 50 iterations). Figure 4.6 illustrates the determined optimal step size for a typical hydraulic fracturing simulation and shows the relative improvement in iterations required to converge over the course

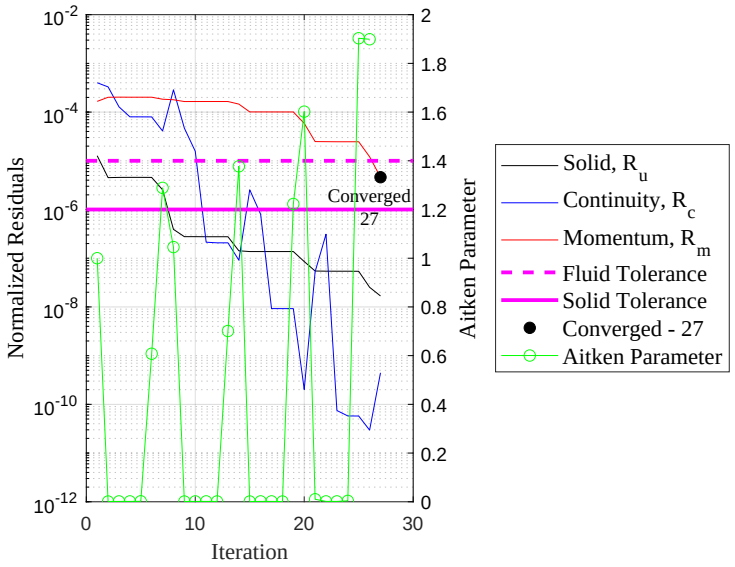

Figure 4.4: The convergence of the various residuals in a typical timestep for a viscous-dominant hydraulic fracturing problem as considered in Section 4.6 with a line search method of $\gamma = 0.8$. Methods are compared for a single small timestep of $\Delta t = 0.1s$ at $10s$ into the simulation. Aitken's Δ^2 parameter is limited to the range $10^{-3} \leq \omega \leq 10$. In this problem, a tolerance of 10^{-5} is specified for the normalized fluid residuals and 10^{-6} is specified for the solid residual. This typical convergence curve illustrates the stiffness of the problem, as even an iteration with minimum Aitken parameter, $\omega = 10^{-3}$, can cause orders of magnitude change in the continuity residual even while the solid and momentum residuals undergo negligible change.

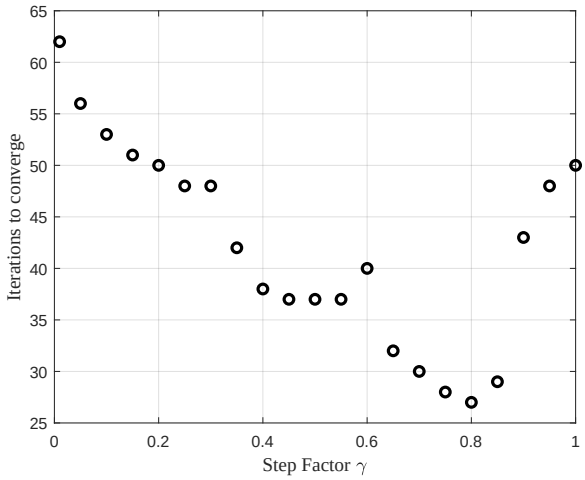

Figure 4.5: The dependence between the line search step factor γ and required iterations to converge for a specific timestep in a viscous-dominant hydraulic fracturing problem as considered in Section 4.6. The relationship is non-monotonic, and more than one local minimum is observed. The optimal step factor requires 46% fewer iterations to converge than a Newton-Raphson scheme. This relationship is unique to this simulation and this timestep, and is not applicable to a general timestep.

of the simulation. The optimal step factor is non-uniform and changes non-monotonically throughout the simulation. Improvements of up to 80% reduction in iterations are observed in single timesteps. The overall performance improvement is more modest, generally in the range of 25-40%, though the authors have observed up to 70% reductions in the number of iterations in exceptional circumstances. More importantly, the resulting algorithm is robust and does not suffer the same convergence issues as the pure Newton-Raphson method.

4.5 Example: Hydro-Mechanical Interactions Arising from Oscillating Quasi-Static Elastic Plates

In this section, we examine the behaviour of a simple hydro-mechanically coupled system for the purpose of verification. In general, verification of the model is difficult as no analytical solutions currently exist for the hydro-mechanically coupled GG22 model. There are however analytical solutions to purely hydraulic GG22 problems and we will demonstrate that the numerical results converge to this solution for sufficiently slow loading rates in which the solid deformations are small. Furthermore, as flow rates decrease, the GG22 model will reproduce the Poiseuille flow response.

Consider the flow through a submerged channel of length $2L$, as illustrated in Figure 4.7. The channel is defined by two elastic plates of thickness H separated by an initial distance of w_0 without cohesive tractions. The exterior edge of the plates oscillate at a fixed frequency Ω according to $\overline{y}(t) = w_0(1 + A\sin(\Omega t)), |A| < 1$ in which A is the relative amplitude of the oscillations. Fluid is permitted to flow in and out of the channel. The pressure at the

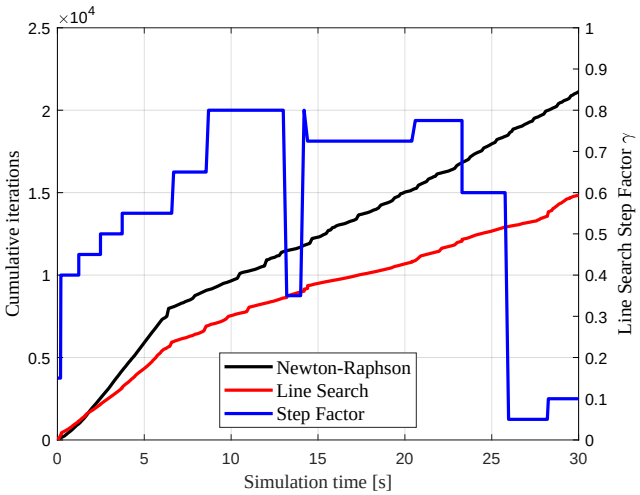

Figure 4.6: The cumulative iterations over 30s simulation time for a a viscous-dominant hydraulic fracturing problem as considered in Section 4.6 with small timesteps. The experimentally determined optimal line-search parameter is shown to be non-constant and change non-monotonically throughout the simulation. The use of line-search over Newton-Raphson reduces the overall number of iterations by 30% for this simulation.

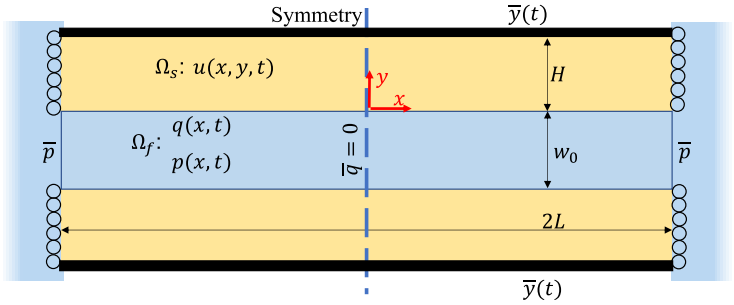

Figure 4.7: Schematic diagram for oscillating elastic plates. The domain is symmetrical along the centerline.

end of the channel is assumed to be fixed at the submerged pressure $p(x = L) = \overline{p}$ and by symmetry the flux at the centerline is $q(x = 0) = 0$.

For sufficiently slow oscillations and laminar flow, the effect of deformation of the rock mass will be negligible and the solution will converge to the rigid plate solution:

$$w(t) = w_0(1 + A\sin(\Omega t)) \tag{4.54}$$

$$q(x,t) = -\dot{w}x \tag{4.55}$$

$$p_{PF}(x,t) = p_0 + \frac{12\mu\dot{w}}{w^2}\frac{L^2}{2}\left(\frac{x^2}{L^2} - 1\right) \tag{4.56}$$

$$p_{GG}(x,t) = p_0 + \left[\rho_f\left(\frac{\ddot{w}}{w} - 2\alpha\left(\frac{\dot{w}}{w}\right)\right) + \frac{12\mu\dot{w}}{w^3}\right]\frac{L^2}{2}\left(\frac{x^2}{L^2} - 1\right) \tag{4.57}$$

Table 4.1: Oscillating Elastic Plate Simulation Parameters

Parameter	Value
L	10 m
H	1 m
w_0	1 mm
ρ_f	1000 kg/m^3
μ	1 $mPa \cdot s$
E	50 GPa
ν	0.25
$\overline{p}$	0 Pa
ϕ	12 s^{-1}
A	0.25

It can be shown that the Poiseuille flow solution, p_{PF}, is only a function of the excitation frequency Ω, while the GG22 solution, p_{GG}, is also a function of the fundamental frequency of the fracture-fluid system, $\phi = \frac{12\mu}{\rho_f w_0^2}$. The fundamental frequency emerges naturally from analytical solutions to the purely hydraulic GG22 model.

The chosen simulation parameters are detailed in Table 4.1. Figure 4.8 illustrates the normalized aperture at the inlet and centerline, the flux at the inlet, and the pressure at the centerline when the elastic plates are oscillated at excitation frequencies of $\Omega = 0.1\phi, 1\phi, 5\phi$. Figure 4.9 illustrates the deformation of the rock mass and fracture as well as the shear forces in the rock mass for the excitation frequency $\Omega = 5\phi$.

At lower excitation frequencies, inertial effects are negligible, and the GG22 solution converges to the Poiseuille flow solution, both of which converge to the rigid plate solution. As the excitation frequency increases, both models depart from the rigid plate solution and each other. At $\Omega = \phi$, the mechanically coupled GG22 models displays larger apertures, pressures, and fluxes than both the rigid plate GG22 solution and the elastic plate Poiseuille flow solution due to the influence of inertial forces. The differences are regular to the oscillation cycle though a phase shift is observed as the solution moves out of sync with the excitation.

At higher excitation frequencies ($\Omega = 5\phi$), the results become chaotic due to the large influence of inertia. The largest apertures are observed, as are the largest raw fluxes and pressures. However the normalized fluxes and pressures decrease relative to $\Omega = \phi$, suggesting a non-linear relationship and the existence of a resonant frequency which produces the largest pressures and fluxes for the least excitation energy. The differences are no longer regular to a single cycle but instead demonstrate regularity to a two-cycle period, suggesting the existence of wave phenomena and interference effects at play. These wave phenomena can be observed in the rock mass as well, despite its quasi-static nature, as Figure 4.9 demonstrates a clear wave in the shear stress that travels down the length of the fracture and reverberate back. Notably, stresses in the rock mass are an order of magnitude greater in the GG22 solution. While the magnitude of stress changes in the

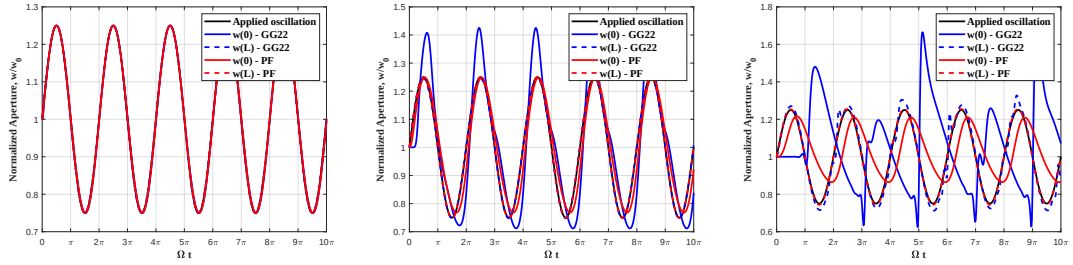

(a) Aperture - $\Omega = 0.1\phi$ (b) Aperture - $\Omega = \phi$ (c) Aperture - $\Omega = 5\phi$

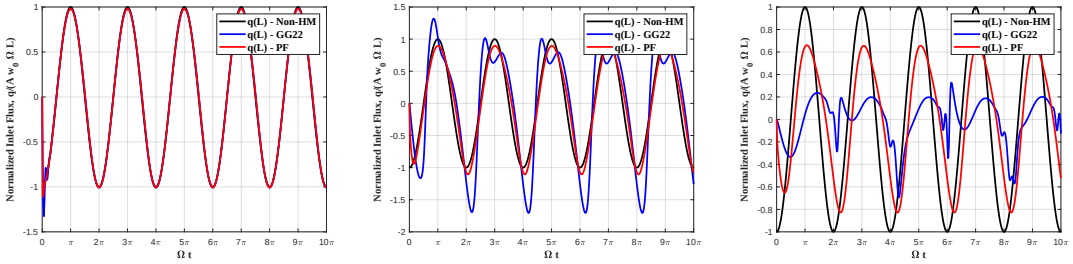

(d) Flux - $\Omega = 0.1\phi$ (e) Flux - $\Omega = \phi$ (f) Flux - $\Omega = 5\phi$

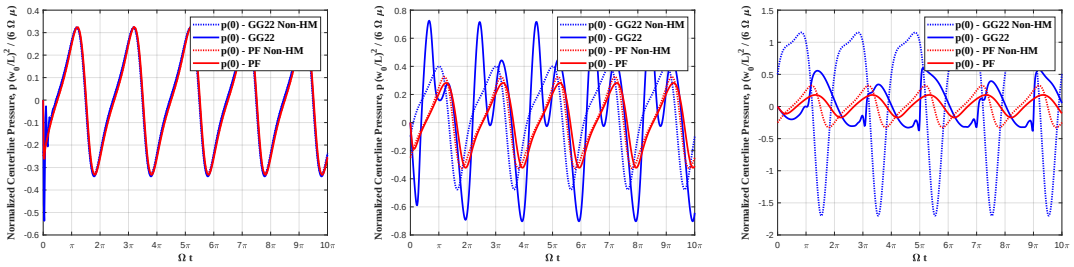

(g) Pressure - $\Omega = 0.1\phi$ (h) Pressure - $\Omega = \phi$ (i) Pressure - $\Omega = 5\phi$

Figure 4.8: The influence of excitation frequency on the fluid response to oscillation of elastic plates. This example problem shows the large departures in behaviour that occur due to fluid inertia in a system at higher excitation frequencies. Furthermore, it validates the numerical model as the coupled hydro-mechanical system matches the analytical solution to a purely hydraulic system at low excitation frequency where the effects of inertia are negligible.

Poiseuille flow solution with excitation frequency, the distribution of stress for the Poiseuille flow solution displays little change with excitation frequency.

This examples not only serves as verification, it also illustrates how the behaviour of the GG22 model departs from the Poiseuille flow model at higher loading frequencies and provides guidance into the unique types of behaviours which might be expected in more traditional fracture flow scenarios at sufficiently high loading rates.

4.6 Application to Planar Hydraulic Fractures

In this section we consider the application of the hydro-mechanical GG22 model to hydraulic fracture propagation of a planar fracture. While previous works have studied turbulence in depth [26], inertia has only briefly been investigated [27]. Furthermore, both of these topics have been primarily studied in the context of tip-asymptotic models. Our study differs in two key ways: a) GG22 model is adopted, which is a mathematically consistent means to consider inertia; and b) fracture propagation is controlled via a cohesive process zone, which is not considered in asymptotic models but is similar to that adopted in Discrete Element models (DEM) [82]. The purpose of this study is not to provide a comprehensive examination on the intricacies and interactions of the fluid physics, but rather to establish the relative importance of fluid inertia and turbulence on fracture propagation within the range of typical hydraulic fracturing scenarios.

Consider the reopening of a cemented KGD-like fracture as illustrated in Figure 4.10. Fluid is injected into the fracture at various flow rates for 60 s. Leak-off is permitted through the fracture tip and pressure at the end of the domain is fixed at the far-field hydrostatic pressure. The injection rate is ramped from zero to the prescribed maximum flow rate over 6 s, then held constant for the remaining 54 s. Two different scenarios are examined, one in which the fracture-fluid system is viscous-dominant, and one in which the fracture-fluid system is toughness-dominant. These two systems are examined with three different layers of fluid physics: a) fluid flows according to Poiseuille flow; b) fluid flows according to the GG22 model, but flow is assumed to be laminar; and c) fluid flows according to the GG22 model, but flow transitions from laminar to turbulent.

The maximum Reynolds number one could reasonably expect to encounter in a planar vertical fracture is estimated based on: a) a formation thickness of $H = 50\ m$, which is relatively small; b) a maximum volumetric flow rate of $Q = 120\ bpm$, which is relatively large; and c) water as the fracturing fluid, which has relatively low viscosity. It is thus estimated that the maximum injection Reynolds encountered in practice might be $Re = \frac{Q}{2H}\frac{\rho_f}{\mu} = 3500$. Injection Reynolds numbers of $Re = 10, 100, 1000, 2000$, and 3500 were tested. The material parameters listed in Table 4.2 are approximately based on a granitic rock mass but were selected such that their theoretical fracture asymptotics as defined in the work of Detournay [40] remain within their respective dominant regimes even at $Re = 3500$. A large surface roughness parameter, ϵ, relative to the aperture is adopted as the fracture surfaces are naturally very rough.

The bounds of the laminar and turbulent regimes are adopted based on the work of Zia and Lecampion [26], such that $Re_L = 1400$ and $Re_T = 5000$ by equating the laminar and

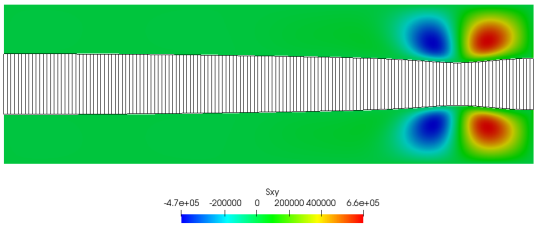

(a) GG22 - $\Omega t = 2\pi$

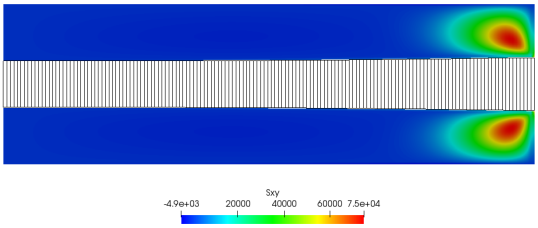

(b) Poiseuille flow - $\Omega t = 2\pi$

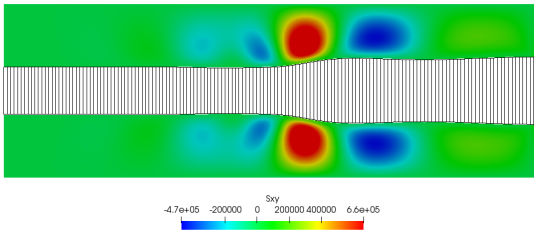

(c) GG22 - $\Omega t = 5\pi/2$

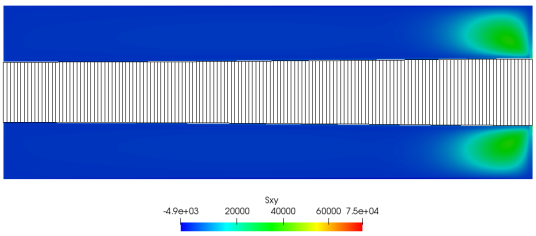

(d) Poiseuille flow - $\Omega t = 5\pi/2$

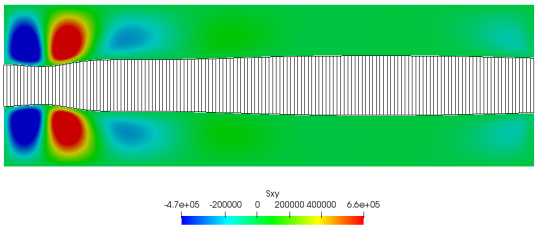

(e) GG22 - $\Omega t = 3\pi$

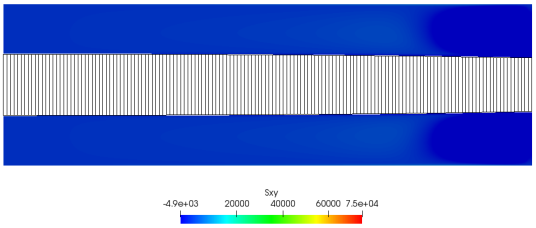

(f) Poiseuille flow - $\Omega t = 3\pi$

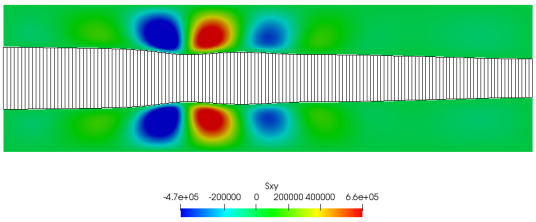

(g) GG22 - $\Omega t = 7\pi/2$

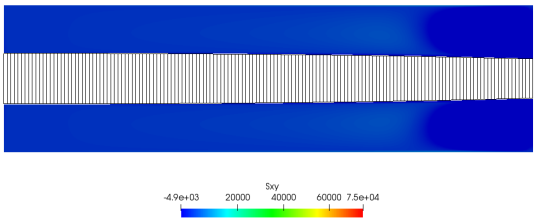

(h) Poiseuille flow - $\Omega t = 7\pi/2$

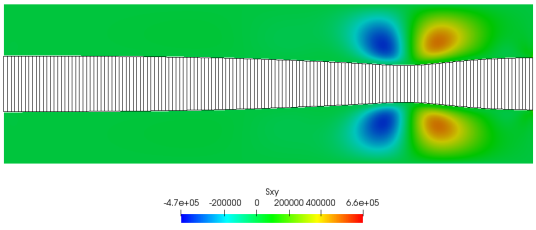

(i) GG22 - $\Omega t = 4\pi$

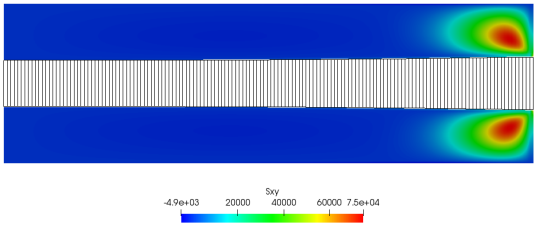

(j) Poiseuille flow - $\Omega t = 4\pi$

Figure 4.9: Shear stress $[Pa]$ in the elastic plates (deformation $\times 1000$) under an excitation frequency of $\Omega = 5\phi$ in the half-domain $0 \leq x \leq L$. Stresses are an order of magnitude larger in the GG22 model and a clear shear wave behaviour is observed in the quasi-static rock mass due to the influence of inertia in the fluid.

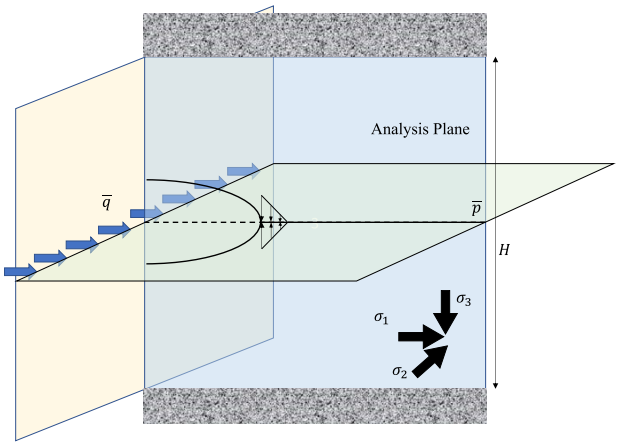

Figure 4.10: Two-dimensional planar hydraulic fracturing domain.

Table 4.2: Hydraulic Fracturing Simulation Parameters

Parameter	Viscous-Dominant	Toughness-Dominant
E	60 GPa	50 GPa
ν	0.25	0.25
G_c	10 J/m^2	100 J/m^2
F_u	4 MPa	10 MPa
ρ_f	1000 kg/m^3	960 kg/m^3
μ	1 $mPa \cdot s$	0.3 $mPa \cdot s$
ϵ	0.5 mm	0.5 mm
w_0	5 μm	5 μm
σ_0	25 MPa	25 MPa
Depth	2000 m	2000 m

turbulent thresholds for pipes with the equivalent hydraulic diameter of the fracture. Thus, the maximum Reynolds number tested in this work falls within the transitional regime and the fluid never enters the fully turbulent regime.

Figure 4.11 illustrates the injection pressure for the GG22 model with and without turbulence over the course of the injection for various flow rates. Negligible differences are observed in the injection pressure between the GG22 and Poiseuille flow models unless turbulence is considered. Higher injection flow rates correlate with higher peak injection pressures. The toughness-dominant fractures produce larger peak pressures than the viscous dominant fractures as the fluid pressure must overcome a larger cohesive force. The toughness-dominant pressures generally decrease over time, as the cohesive forces govern fracture length and thus apertures increase faster than fracture length which reduces the fluid resistance. The viscous-dominant fractures generally see pressures increase over time at higher flow rates, as the pressure at the inlet must increase to compensate for the increased length of the fracture. The largest differences are observed with the inclusion of turbulence, where a sharp departure is observed when the fluid passes the critical Reynolds

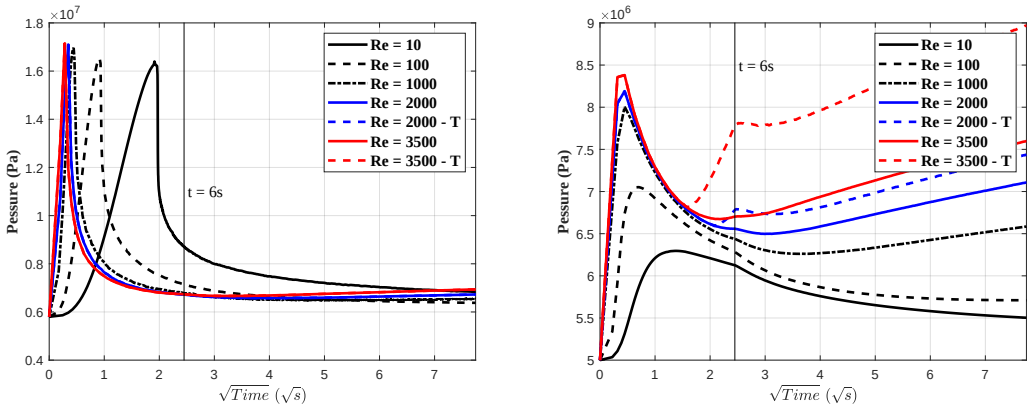

(a) Toughness-Dominant Fracture (b) Viscous-Dominant Fracture

Figure 4.11: Comparison of GG22 injection pressures for various Reynolds numbers over time. Negligible differences are observed between the GG22 and Poiseuille flow models. "T" indicates the inclusion of turbulence. Turbulence causes the injection pressure to increase, as the pressure must overcome larger fluid resistance.

number. Pressure flat-lines when the injection becomes constant then slowly increases over time, as in the case without turbulence.

Figure 4.12 illustrates the fracture lengths and injection point aperture for the toughness dominant fracture after $60s$ for various flow rates. A power-law relationship is observed between injection Reynolds number and fracture length or injection aperture. Minor differences on the order of 10^{-3} are observed between the Poiseuille flow and GG22 models — centimetre differences on decametre fracture lengths. Figure 4.13 illustrates the spatial distribution of aperture, Reynolds number, and pressure for an injection rate of $Re = 2000$ after 60 s of injection. Negative fluxes are observed ahead of the fracture tip within the residual aperture, but they are small compared to flux within the fracture. A sharp pressure front is observed at the fracture tip and the pressure is lower than the far-field pressure. A pressure boundary layer precedes the fracture tip in the cohesive zone which returns to the far-field pressure farther ahead of the fracture. The differences between the GG22 and Poiseuille flow models both spatially and temporally are on the order of 10^{-3} and are practically imperceptible at the plotted scales.

Figure 4.14 illustrates the fracture lengths and injection point aperture for the viscous-dominant fracture after $60s$ for various flow rates both with and without turbulence. The differences between the GG22 and Poiseuille flow models are even less significant in the viscous dominant regime, on the order of 10^{-4} when turbulence is not considered. When turbulence is considered, significant differences are observed. In response to the higher fluid resistance, fracture lengths decrease up to 18%. In order to conserve the injected volume, fracture apertures greatly increase by up to 50%. Figure 4.15 illustrates the spatial distribution of aperture, Reynolds number, and pressure for an injection rate of $Re = 2000$ after 60 s of injection. Within the 90 m fracture, there is a transition at $x = 63$ m such that turbulence develops near the injection point but flow near the tip is laminar. The characteristic shape of the solution also changes and steeper gradients in aperture, flux, and

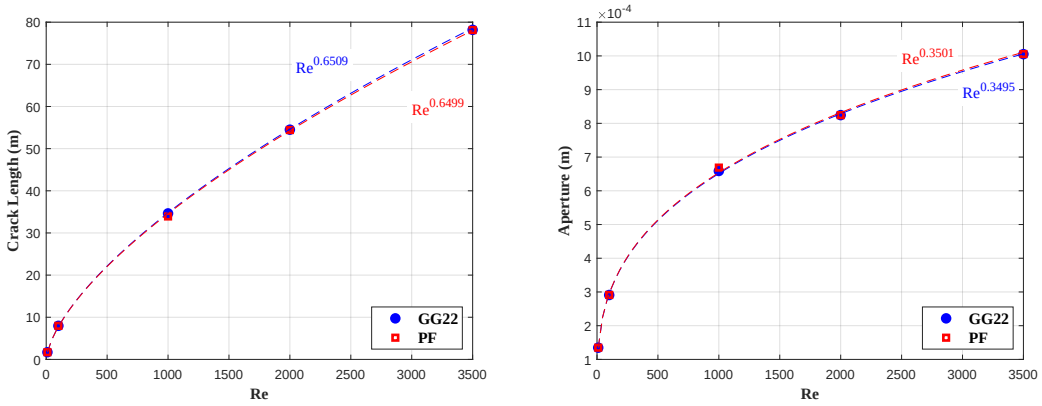

(a) Fracture Lengths (b) Wellbore Aperture

Figure 4.12: Comparison of toughness-dominant fracture lengths and wellbore apertures after 60s of injection. A power-law relationship between the crack length and injection Reynolds number is observed. Minor differences on the order of 10^{-3} are observed between the GG22 and Poiseuille flow solutions when turbulence is not considered.

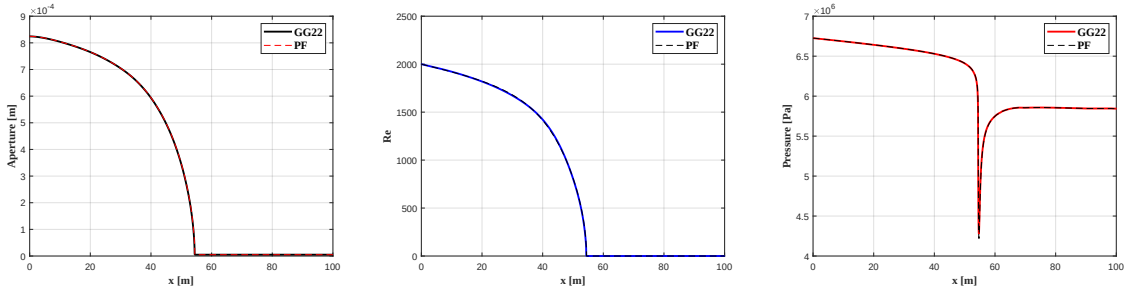

(a) Aperture (b) Reynolds number (c) Pressure

Figure 4.13: Spatial distribution of aperture, Reynolds number, and pressure in the toughness-dominant fracture for an injection Reynolds number of 2000 after 60s of injection. Minimal differences are observed between the Poiseuille flow and GG22 solutions, verifying that in the context of planar hydraulic fractures, inertia is indeed negligible.

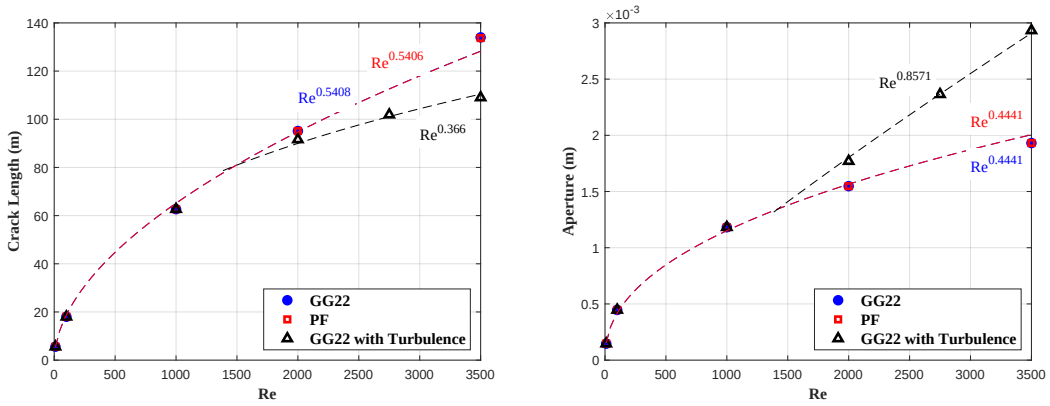

(a) Fracture Lengths (b) Fracture Inlet Aperture

Figure 4.14: Comparison of viscous-dominant fracture lengths and inlet aperture after 60s of injection. A power-law relationship between the aperture and injection Reynolds number is observed. Minor differences on the order of 10^{-4} are observed between the GG22 and Poiseuille flow solutions when turbulence is not considered. Turbulence produces significant changes and fundamentally different solutions.

pressure are all observed near the injection point. As a large surface roughness is adopted, the turbulent friction factor f_D is primarily a function of the surface roughness ($> 95\%$) instead of the Reynold's number ($< 5\%$) based on equation (5.9). While adopting smaller surface roughness would result in less turbulent effects, similar high surface roughnesses relative to the aperture are expected in natural fractures.

Therefore, the results verify the assumptions of previous works that inertia is indeed negligible within the context of planar fractures. Furthermore, non-cubic law behaviour does not appear in the vicinity of the fracture tips, suggesting that in these contexts fracture tip asymptotics remain unchanged. However, turbulence is important and will create substantially different solutions as soon as it is invoked. Inertia remains negligible even in the turbulent case. Care must be taken in considering the results of Poiseuille flow-based models when considering large flow rates, low viscosity fluids, or small formations.

These results are only applicable to hydraulic fracturing based on constant injection into a planar fracture. Further investigation is required to examine the role of inertia in axisymmetric and two-dimensional fractures, as well as non-constant injection scenarios like pressure pulsing [29]. Preliminary investigations into axisymmetric fractures suggest that inertia has a significant role [83, 84] and the null result returned here will not be applicable.

4.7 Conclusions

In this chapter, a fully-coupled hydro-mechanical coupled model based on the GG22 flow model is developed and numerical challenges are addressed. The hydro-mechanically coupled GG22 model yields comparable convergence properties to the Poiseuille flow model

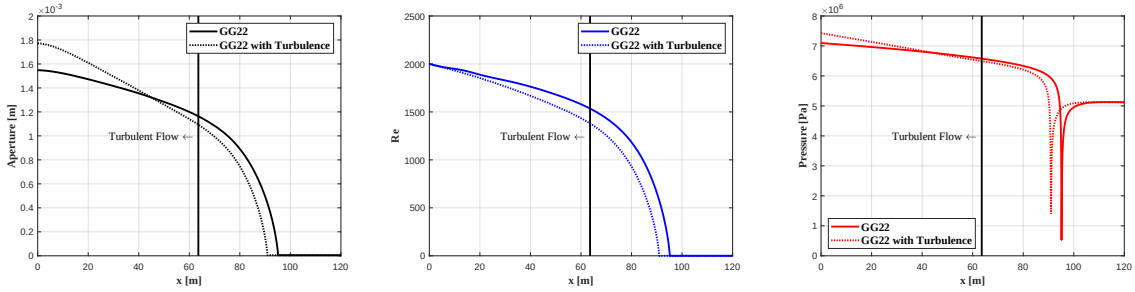

(a) Aperture (b) Reynolds number (c) Pressure

Figure 4.15: Spatial distribution of aperture, Reynolds number, and pressure in the viscous-dominant fracture for an injection Reynolds number of 2000 after 60s of injection. While the Poiseuille flow solution exhibits negligible differences, there are significant differences between the turbulent and laminar cases. The transition from turbulent to laminar flow occurs at 63 m, with the tip remaining laminar while turbulent flow occurs near the inlet. The characteristic shape of the solution changes in the turbulent region, such as steeper gradients can be observed.

when applied to elastic fractures, but slower convergence when combined with cohesive fracture models. Aitken's relaxation is extremely effective in both accelerating the convergence of the iterative scheme and improving its robustness. The use of a steepest-descent line search in this context is demonstrated to be superior to a Newton-Raphson method. The line search method using an empirically determined optimal step size parameter accelerates the rate of convergence and results in a robust solution algorithm.

The model is verified with applications to flow through a channel between oscillating elastic plates and the propagation of two-dimensional KGD-like hydraulic fractures. The case of oscillating elastic plates illustrates that the influence of inertia causes the GG22 solution to depart from the Poiseuille flow solution at higher loading rates and frequencies. Fluid behaviours similar to those in Chapter 3 are observed, including phase shifts, larger pressures, and lower fluxes. In the rock mass new phenomena including larger stresses, and wave-like interference behaviour are observed in both the rock mass and the fluid even when the rock mass is quasi-static. Next, the model was applied to hydraulic fracturing of cohesive planar KGD-like fractures. No inertial effects are observed in planar hydraulic fractures with constant injection rates. Turbulence is shown to have significant effects on the solution, resulting in shorter fractures with more fracture opening as a result of the increased resistance to flow. Non-cubic law behaviour does not appear in the vicinity of fracture tips, suggesting that in these contexts tip asymptotic behaviour is unchanged.

Now that we have developed a hydro-mechanically coupled numerical model for the GG22 model, we can apply it to common fracture flow scenarios to examine the role of inertia, turbulence, and transient behaviours.

Chapter 5

Inertia and Turbulence in Radial Hydraulic Fractures

5.1 Introduction

While planar fracture have large widths over which to distribute the flow, resulting in lower Reynolds numbers, this is not a luxury afforded to axisymmetric/radial fractures. Near the wellbore, the large flow rates are distributed around a very small circumference, leading to very large Reynolds numbers. These large Reynolds numbers decay quickly as the fluid is dispersed into the fracture, leading to a loss of kinetic energy that must be conserved or dissipated elsewhere in the domain. Large Reynolds numbers also imply the development of turbulence near the wellbore: consider for example the properties of water and a wellbore diameter of 15 cm, then a flow rate of 1 L/s is sufficient to produce inlet Reynolds numbers in excess of 2000. Near the tip, the gradient of aperture is large, which is a significant violation of the Poiseuille assumption, but the flow rate is small, so without investigation it is difficult to estimate the importance of inertial behaviours. Thus, in this chapter the hydro-mechanically coupled model developed in Chapter 4 is used to investigate the role of inertia and turbulence in radial fracture propagation.

Section 5.2 describes the axisymmetric governing equations of the rock mass deformation, fluid flow, and hydro-mechanical coupling. Section 5.3 establishes the parameters of a typical hydraulic fracturing scenario which we will consider for investigation. In Section 5.4, we investigate the solutions to the model problem by varying the fluid physics model, starting with the standard Poiseuille flow solution, then introducing one new phenomenon at a time until we reach the full GG22 fluid model. Next, we discuss the impacts of surface roughness and fracture toughness on the observed results in Section 5.5 and 5.6. Last, Section 5.7 discusses how the results change when we introduce friction reducers into the fluid and change the turbulent regime transition point.

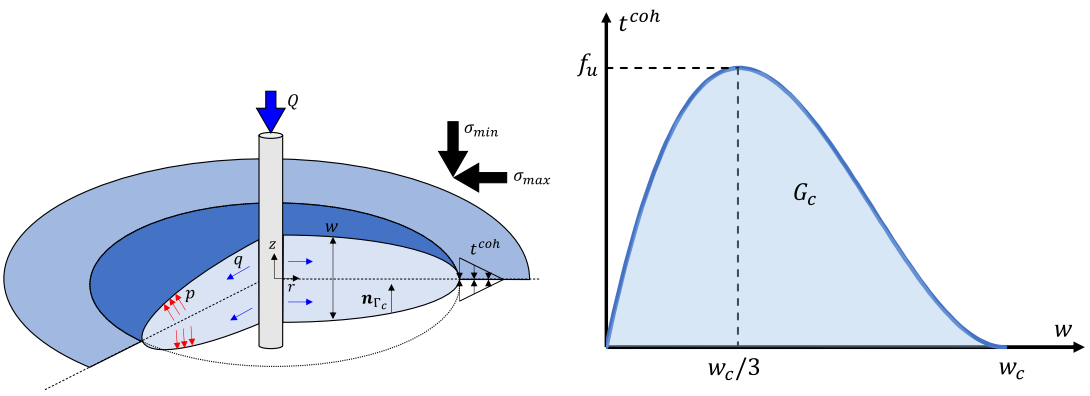

(a) Mathematical Domain. (b) Cubic cohesive traction-separation law.

Figure 5.1: Mathematical domain for an impermeable axisymmetric rock mass under in-situ stress with discrete pre-existing fluid-filled fractures. Fracture propagation is controlled by the fracture process zone ahead of the fracture tip which follows a cubic traction-separation law.

5.2 Governing Equations

Consider an impermeable rock mass under in-situ stresses as illustrated in Figure 5.1a. Fluid flows through fractures which may propagate through the rock mass. Axisymmetric conditions are assumed, such that the rock mass, Ω_s, is considered as a two-dimensional body and the fractures are considered as one-dimensional spaces characterized by an aperture $w(r,t)$ with negligible transverse flow. Typically, fluid flow within fractures is characterized by the Poiseuille flow equation. In this work, we use the GG22 fluid model to explore the phenomena that arise at high flow rates [41].

The GG22 flow model is a two-field model that describes the behaviour of an incompressible fluid with a flux, $q(r,t)$, and a pressure, $p(r,t)$. The incompressible fluid has density ρ_f and viscosity μ. The governing equations of the GG22 model in axisymmetric form are

$$\frac{\partial w}{\partial t} + \frac{1}{r}\frac{\partial}{\partial r}(rq) = 0 \tag{5.1}$$

$$\frac{\partial q}{\partial t} + \frac{1}{r}\frac{\partial}{\partial r}\left(r\alpha\frac{q^2}{w}\right) = -\frac{w}{\rho_f}\frac{\partial p}{\partial r} - \frac{1}{2}\frac{f_D}{w^2}q^2 \tag{5.2}$$

in which (5.1) is the continuity equation describing the conservation of fluid mass, and (5.2) describes the conservation of fluid momentum. The conservation of momentum equation is comprised of several new terms compared to the Poiseuille flow model. These terms will be referred to as follows:

$$\text{The transient term:} \qquad \frac{\partial q}{\partial t} \tag{5.3}$$

$$\text{The convective term:} \qquad \frac{1}{r}\frac{\partial}{\partial x}\left(r\alpha\frac{q^2}{w}\right) \tag{5.4}$$

$$\text{The pressure term:} \qquad -\frac{w}{\rho_f}\frac{\partial p}{\partial r} \tag{5.5}$$

$$\text{The friction term:} \qquad -\frac{1}{2}\frac{f_D}{w^2}q^2 \tag{5.6}$$

The transient term and the convective term will collectively be referred to as "the inertial terms". While turbulence cannot exist without inertia, the friction term is differentiated because friction is a dissipative phenomena, while the transient and convective terms capture transformative phenomena.

In addition to the fields q, p, the conservation of momentum is also a function of two dimensionless coefficients which are functions of the flow regime. First, the momentum correction factor $\alpha(Re)$ considers the increase in total momentum carried by a non-uniform velocity profile across the aperture. Assuming a parabolic velocity profile in laminar flow and a 1/7 power-law profile in turbulent flow, the momentum correction factor is defined as

$$\alpha = \begin{cases} \frac{6}{5} & \text{if } Re \leq Re_L \\ \frac{64}{63} & \text{if } Re \geq Re_T \end{cases} \tag{5.7}$$

$$Re = \frac{\rho_f |\overline{v}| w}{\mu} = \frac{\rho_f |q|}{\mu} \tag{5.8}$$

in which Re_L is the Reynolds number defining the threshold between the laminar regime and the transitional regime, and Re_T is the Reynolds number defining the threshold between the transitional regime and the fully turbulent regime.

The friction factor f_D accounts for the dissipation of fluid momentum by viscous and turbulent forces. In the laminar regime, dissipation is the result of viscous shear with the fracture faces, and in the turbulent regime dissipation is caused by both viscous shear and turbulent eddy formation. An empirical relationship is required to determine the friction factor in the turbulent regime, and so the Colebrook-White equation is adopted for simplicity [45]. The friction factor is thus defined as

$$f_D = \begin{cases} \frac{24}{Re} & \text{if } Re \leq Re_L \\ \frac{1}{\sqrt{f_D}} = -2\log(\frac{\epsilon}{7.4w} + \frac{2.51}{Re\sqrt{f_D}}) & \text{if } Re \geq Re_T \end{cases} \tag{5.9}$$

in which ϵ is a measure of the surface roughness of the fracture. In the transitional fluid regime, $Re_L < Re < Re_T$, both the momentum correction factor and the friction factor are linearly interpolated. Assuming a Newtonian fluid as the injection fluid (water) the transition from the laminar to the turbulent regime begins at $Re \approx 2000$, while the fully

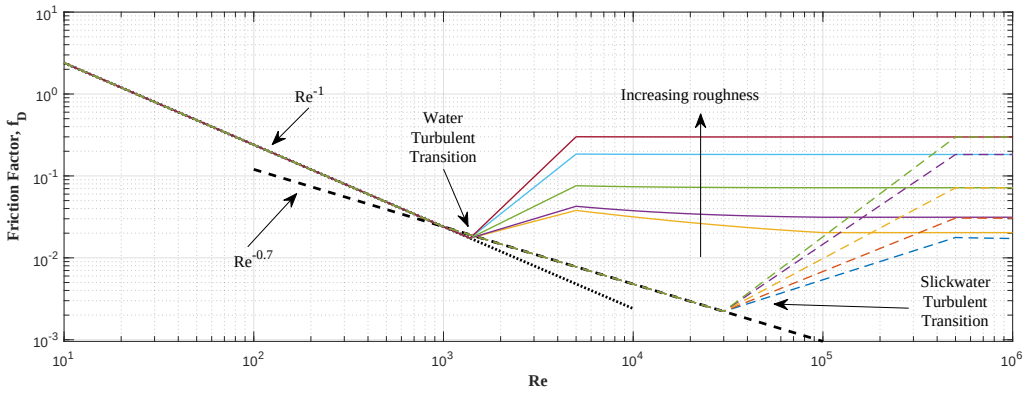

Figure 5.2: Friction factor as a function of Reynolds number for a standard Newtonian fluid (water) and a fluid enhanced with friction reducers (slickwater).

turbulent regime begins at $Re \approx 5000$. The friction factors for water are illustrated in Figure 5.2.

To reduce the energy required to pump the fluid down the wellbore, it is common to introduce friction reducers into the fluid to create slickwater [85, 86]. Friction reducers are long-chain polymers which may be added in small quantities to disrupt the formation of turbulent eddies, delaying the onset of turbulence. The reduction in friction factor reaches a maximum drag reduction asymptote (MDR) at small concentrations [85]. The concentration is dilute, so the density of the bulk fluid remains unchanged, but the viscosity is affected. The fluid becomes non-Newtonian and experiences shear thinning, with the viscosity approaching an asymptotic viscosity after shear degradation. After degradation, the fluid viscosity is approximately constant. It is thus assumed that the slickwater has experienced sufficient shear during in the wellbore that it has reached its asymptotic viscosity in the fracture. A Newtonian fluid behaviour is thus assumed in the fracture with an appararent viscosity of $5mPa \cdot s$ [87]. The friction reducers delay the onset of turbulence from $Re \approx 2000$ up to $Re \approx 3 \times 10^4$. Fully turbulent flow is observed at $Re \approx 5 \times 10^5$, so there is a transitional regime between the fully turbulent and MDR regimes. In the MDR regime, which begins at $Re \approx 1000$, the MDR asymptote is correlated with the Reynolds number such that $f_D \propto Re^{-0.7}$ [85]. The friction factor for slickwater is illustrated in Figure 5.2.

In the laminar regime, the friction term simplifies to $\frac{-12\mu}{\rho_f w^2} q$. Under Poiseuille flow conditions, i.e. steady flow through parallel plates, the conservation of momentum equation (5.2) recovers the Poiseuille flow constitutive model:

$$0 = -\frac{w}{\rho_f}\frac{\partial p}{\partial r} - \frac{12\mu}{w^2 \rho_f} q \implies q = -\frac{w^3}{12\mu}\frac{\partial p}{\partial r} \tag{5.10}$$

such that flux is a function of the pressure gradient, $q = f(p)$, and the fluid may be described with a single field, $p(r, t)$.

The rock mass is modeled as a quasi-static impermeable linear elastic axisymmetric medium under in-situ stress. The equilibrium equation governs the deformation of the rock mass,

such that

$$0 = \nabla \cdot \boldsymbol{\sigma}(\boldsymbol{u}) \text{ on } \Omega_s \tag{5.11}$$

$$\boldsymbol{\sigma} - \boldsymbol{\sigma}_0 = \mathbb{C} : \varepsilon \tag{5.12}$$

in which $\boldsymbol{u}(r, z, t)$ is the rock mass deformation, $\boldsymbol{\sigma}$ is the axisymmetric Cauchy stress tensor, $\boldsymbol{\sigma}_0$ is the in-situ stress tensor, $\mathbb{C}$ is the axisymmetric elasticity tensor, and ε is the axisymmetric linear strain tensor. The rock mass contains fractures defined by an aperture w which is a function of the deformation of the rock mass. The relationship between aperture and deformation is

$$w = w_0 + \boldsymbol{n}_{\boldsymbol{\Gamma_c}} \cdot \boldsymbol{u}\Big|_{\Gamma_c} \tag{5.13}$$

in which w_0 is some residual aperture in a pre-existing cemented fracture that may arise from surface roughness, and Γ_c is the fracture surface. The pre-existing cemented fractures are modelled with a traction-separation law such that a quasi-brittle cohesive fracture process zone forms ahead of the fracture. A cubic traction-separation law [76] is adopted, as illustrated in Figure 5.1b. The traction-separation law is defined as a function of the aperture according to

$$t^{coh}(w) = \begin{cases} \frac{27}{4} f_u \Delta(1 - 2\Delta + \Delta^2), \ w \leq w_c \\ 0, \ w > w_c \end{cases} , \ \Delta = \frac{w}{w_c} \tag{5.14}$$

$$w_c = \frac{48}{27} \frac{G_c}{f_u} \tag{5.15}$$

in which f_u is the cohesive strength of the rock mass, G_c is the fracture energy, and w_c is the critical aperture which defines the boundary between the cohesive zone and the physical fracture tip. The rock mass is therefore subject to tractions on the fracture surfaces such that

$$\boldsymbol{\sigma} \cdot \boldsymbol{n}_{\Gamma_c^{\pm}} = (-p + t^{coh})\mathbf{I} \cdot \boldsymbol{n}_{\Gamma_c^{\pm}} \text{ on } \Gamma_c^{\pm} \tag{5.16}$$

in which $\boldsymbol{n}_{\Gamma_c^{\pm}}$ is the corresponding normal to the face of the fracture, $\Gamma_c^{\pm}$.

5.3 Model Problem: Radial Fracture Propagation

In this paper, we consider a single hydraulic fracturing scenario and examine how it reacts to varying fluid physics.

Consider the re-opening of a cemented radial fracture with a small residual aperture. The fracture is assumed to have an initial residual aperture of $w_0 = 5 \ \mu m$. Due to the residual aperture, the fracture tip allows fluid flow. Ahead of the fracture tip at the end of the computational domain, a Dirichlet condition is imposed on the pressure such that the pressure is fixed at the far-field hydrostatic pressure of $\overline{p} = \rho_f g h$ in which g is the

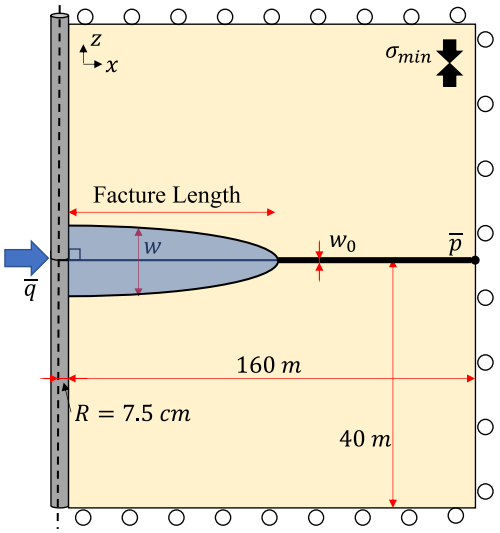

Figure 5.3: Computational domain for the reopening of a cemented radial fracture.

acceleration due to gravity. The surface roughness of the fracture faces is conceptualized as asperities which are compressed in the initial stress state and decompress as the fracture opens, such that the maximum relative roughness is set to $\epsilon/w = 0.99$ is set when the roughness up to a maximum of 0.5 mm.

The radial fracture exists within an impermeable granite rock mass at a depth of 2000 m and a minimum in-situ stress of 25 MPa. The dimensions of the computational domain are illustrated in Figure 5.3. The rock mass has a tensile strength of 10 MPa, and elastic modulus of 60 GPa, and a Poisson's ratio of $\nu = 0.25$.

Fluid is injected into a wellbore with a diameter of $D = 15\ cm$. The injection fluid is assumed to be water with a constant viscosity of $\mu = 1\ mPa \cdot s$ and a constant density of $\rho_f = 1000\ kg/m^3$. The injection rate Q_o is specified in terms of the injection Reynolds number, $Re = \frac{\rho_f \overline{q}}{\mu} = \frac{\rho_f Q_o}{\mu \pi D}$. Injection rates of $Re = 10$ up to $Re = 2 \times 10^5$ are considered. Figure 5.4 illustrates the relationship between injection flow rate, injection Reynolds number, and wellbore diameter. For the problem considered, the maximum injection Reynolds number corresponds to a maximum injection flow rate of 36 bpm (5.75 m^3/min, 96 L/s). The injection rate is applied with a linear ramp over the first 6 s, and a constant injection rate for the rest of the simulated time. The fracture propagation is simulated for a total of 60 s.

A zero-toughness fracture case is considered first, such that the fracture propagation is restricted only by the resistance of the initial residual aperture. In this case, the physical tip is assumed to be the coordinate where $w > w_0$. Next, various fracture toughnesses are considered using the cubic cohesive zone traction-separation law.

The model problem is solved numerically using a fully-coupled monolithic mixed FEM-FVM method [88]. Finite elements are used to discretize the rock mass, while finite volumes are used to discretize the fracture.

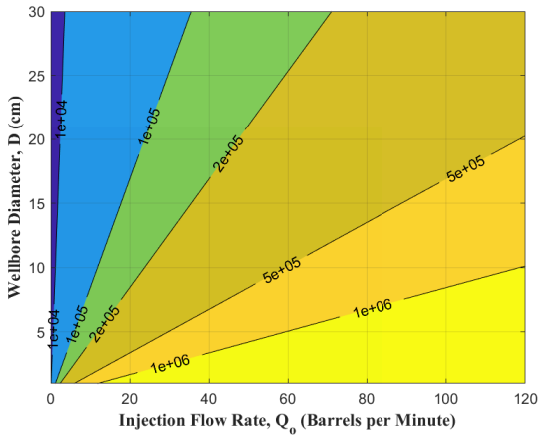

Figure 5.4: Reynolds number at the wellbore as a function of wellbore diameter and injection flow rate. Even small flow rates can induce large Reynolds numbers at the wellbore.

5.4 The Effects of Turbulence and Inertia

In this section, we will examine the behaviour of the fracture propagation problem described in Section 5.3. To isolate the fluid behaviour, a zero-toughness fracture is considered ($G_c = 0\,J/m^2$). We will consider the problem with four layers of fluid physics by modifying the conservation of momentum equation (5.2). First, we will consider the problem using the standard Poiseuille flow model, which assumes steady laminar flow through constant aperture. Next, we will upgrade the friction term to capture turbulent flow, but neglect the inertial terms introduced by the GG22 model. Third, we will assume laminar flow, but introduce the inertial terms into the conservation of momentum. Last, we will consider the full GG22 conservation of momentum equation. By layering the physics one at a time, we will be able to isolate how each term affects the solution and determine the flow rate threshold at which each layer becomes relevant.

5.4.1 The Poiseuille flow solution

First we discuss the standard Poiseuille flow solution as a baseline case for the model problem. The Poiseuille flow model is the standard assumption for across most fracture flow simulations. Steady laminar flow is assumed and the conservation of momentum equation (5.2) simplifies to

$$0 = -\frac{w}{\rho_f}\frac{\partial p}{\partial r} - \frac{12\mu}{\rho_f w^2}q \tag{5.17}$$

which can be rearranged as a constitutive relationship between flux and pressure such that

$$q = -\frac{w^3}{12\mu}\frac{\partial p}{\partial r} \tag{5.18}$$

Figure 5.5 illustrates the pressure at the wellbore. There is an initial peak pressure associated with the re-opening of the fracture, followed by a monotonic decrease in pressure.

Within the constitutive equation there are two competing processes, fracture lengthening and fracture opening. Lengthening requires an increase in pressure at the wellbore to propel the fluid a farther distance. Opening decreases the pressure at the wellbore as the resistance to fluid flow decreases. The injection pressures indicate that fracture opening generally dominates, but at higher injection rates, the pressure decreases more slowly over time as fracture lengthening has a greater contribution.

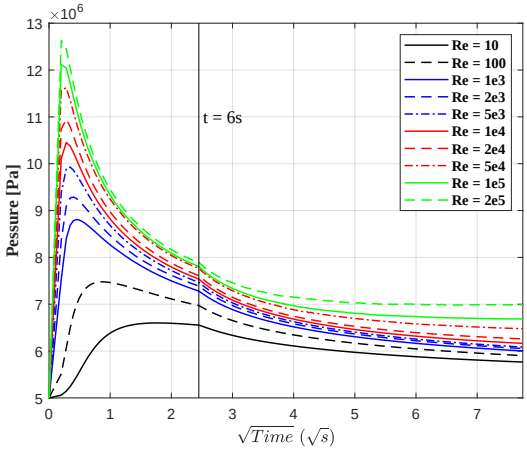

Figure 5.5: Injection pressure for varying injection rates with a Poiseuille flow model. The Poiseuille flow solution shows a spike in pressure to reopen the fracture, then decreases over time.

Figure 5.6a illustrates the pressure along the fracture after 60 s of injection at the highest tested injection rate of $Re = 2 \times 10^5$. The pressure decreases monotonically until the fracture tip. There is a discontinuity in the pressure gradient at the fracture tip, as the permeable fracture tip creates a zone of negative flow ahead of the tip. Farther ahead of the fracture tip, the pressure slowly returns to the far-field pressure. Figure 5.6b illustrates the aperture along the fracture. Aperture decreases monotonically and continuously. There is a discontinuity in the aperture gradient at the tip.

5.4.2 The effects of turbulence

Next we consider replacing the Poiseuille constitutive equation with a turbulent friction term. Given that most fracture flow simulation tools are developed for Poiseuille flow, the inclusion of the inertial terms in the conservation of momentum equation are intrusive and require significant modifications. The implementation of a turbulent friction term without the inertial terms is therefore an attractive prospect for capturing the effects of turbulence with minimally intrusive implementation.

The equation for conservation of momentum (5.2) becomes

$$0 = -\frac{w}{\rho_f}\frac{\partial p}{\partial r} - \frac{f_D(q)}{w^2}q^2 \tag{5.19}$$

which may be rearranged into a non-linear constitutive equation

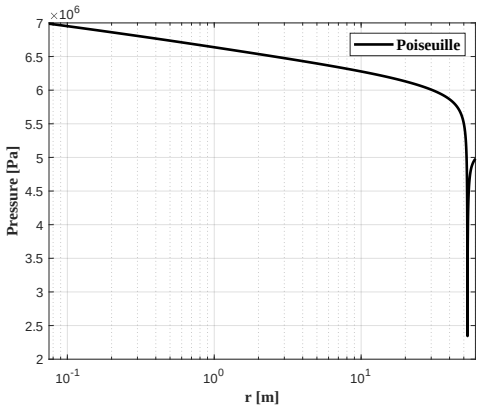

(a) Pressure decreases along the fracture and a sharp decrease in pressure is observed at the fracture tip.

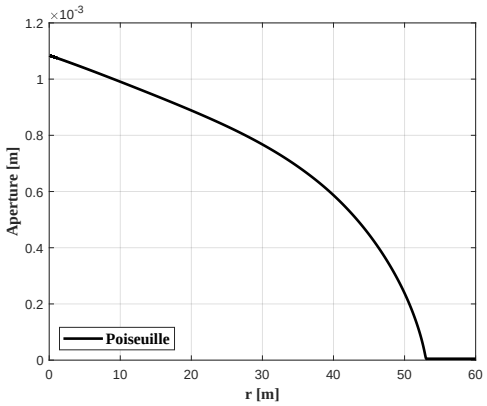

(b) Aperture decreases along the fracture.

Figure 5.6: Pressure and aperture along the fracture with a Poiseuille flow model after 60 s of injection with an injection rate of $Re = 2 \times 10^5$.

$$q = -\frac{w^3}{\rho_f f_D(q) \cdot q} \frac{\partial p}{\partial r} \tag{5.20}$$

Figure 5.7 illustrates the pressure at the wellbore for increasing flow rates. There is an initial local peak pressure associated with the opening of the fracture, as observed in the Poiseuille flow case. Unlike the Poiseuille flow case, at sufficiently high flow rates to induce turbulence, the required pressure to maintain the injected flow rate increases due to the resistance created by turbulence. With a turbulent flow model, the pressure required to maintain a flow of $Re = 2 \times 10^5$ is approximately four times greater than with the Poiseuille flow model.

Figure 5.8a illustrates the pressure along the fracture compared to the Poiseuille flow case after 60 s of injection at the highest tested injection rate of $Re = 2 \times 10^5$. There is a region of significantly elevated pressure near the wellbore extending up to 5 m along the fracture radius. Farther along the fracture, the fluid returns to laminar flow and the pressures are similar to the Poiseuille flow profile. Figure 5.8b illustrates the aperture distribution along the fracture. The elevated pressures near the wellbore create a region of increased aperture, with an increase of 90 % at the wellbore in this case. The aperture decreases monotically along the fracture, but the curvature of the aperture changes around 20 m. To conserve the total injected volume, the aperture farther along the fracture are slightly smaller and the overall fracture length is slightly shorter than the Poiseuille flow case.

5.4.3 The effects of inertia

Next, we consider the behaviour of fracture growth when we introduce the inertial terms but maintain the laminar flow assumption from Poiseuille flow. The conservation of momentum

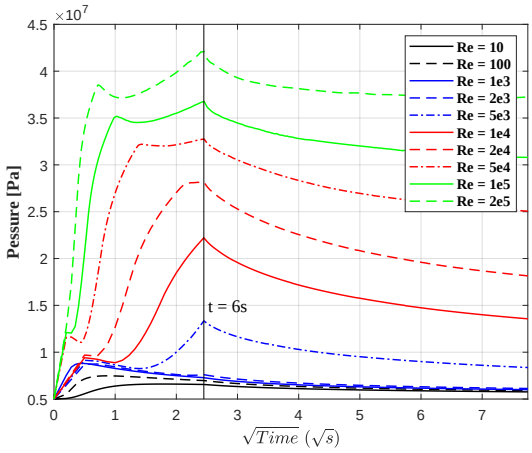

Figure 5.7: Injection pressure for varying injection rates with a turbulent model neglecting inertia. The inclusion of turbulence requires much higher pressures to achieve the same injection rates. Large pressures are required to open the fracture, then pressure decreases, but the increasing flow rate increases resistance to flow resulting in a peak pressure at 6s when the flow finishes ramping up to its prescribed injection rate.

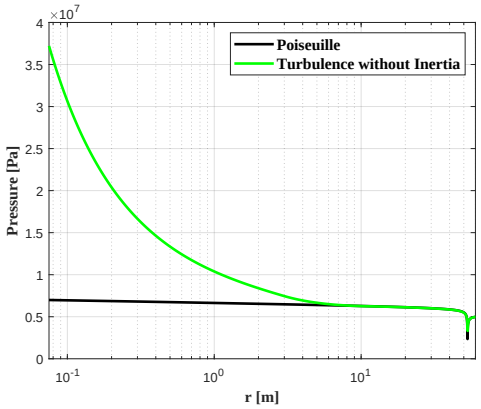

(a) A large increase in pressure is observed near the wellbore to overcome the turbulent resistance.

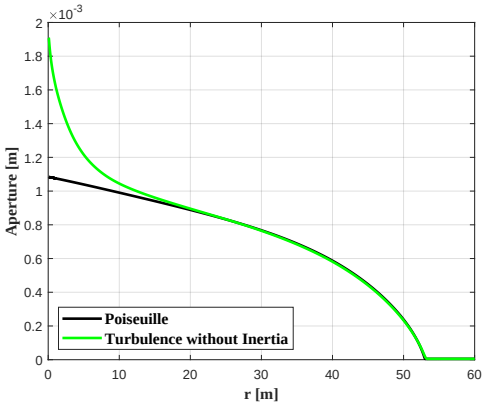

(b) The large increase in pressure at the wellbore causes a large increase in aperture (a 90% increase in this simulation).

Figure 5.8: Pressure and aperture along the fracture with a turbulent flow model that neglects inertia after 60 s of injection with an injection rate of $Re = 2 \times 10^5$.

equation (5.2) becomes

$$\frac{\partial q}{\partial t} + \frac{1}{r}\frac{\partial}{\partial r}\left(r\frac{\alpha}{w}q^2\right) = -\frac{w}{\rho_f}\frac{\partial p}{\partial r} - \frac{12\mu}{\rho_f w^2}q \tag{5.21}$$

and cannot be re-arranged into a constitutive equation. It remains a separate coupled governing partial differential equation which must be simultaneously solved.

Figure 5.9 illustrates the pressure at the wellbore for increasing injection rates. At sufficiently high flow rates, the inertial terms induce positive pressure gradients and therefore

the pressure at the wellbore required to maintain the injection flow rate decreases. There is an initial peak positive pressure associated with reopening the fracture, after which as the flow rate increases, the wellbore pressure drops precipitously. The pressures illustrated in Figure 5.9 are gauge pressures relative to the hydrostatic pressure, and so the negative gauge pressure are still positive absolute pressures and cavitation is not a concern.

The dominant term behind the negative pressure is the continuity term. Consider the case of injection at a constant rate into a set of radial parallel plates (constant w). In this case, the steady-state solution for flux takes the form, $q \propto 1/r$. The velocity of the fluid is proportional to the flux, $q = \overline{v}w$, where $\overline{v}$ is the average fluid velocity across the cross-section. Thus as the flux moves away from the wellbore, the velocity of the fluid must decrease to maintain continuity. When the fluid velocity is decreasing, that kinetic energy must be transformed into potential energy or dissipated. If the friction term cannot dissipate the excess kinetic energy faster than the rate at which the fluid is decelerating, the transformation and conservation of energy causes an increase in potential energy which is represented by an increase in fluid pressure. The result is the development of a positive pressure gradient at the wellbore despite the positive direction of flow. The negative pressure causes the aperture to decrease, which then increases the friction term, leading to non-monotonic interactions at high Re.

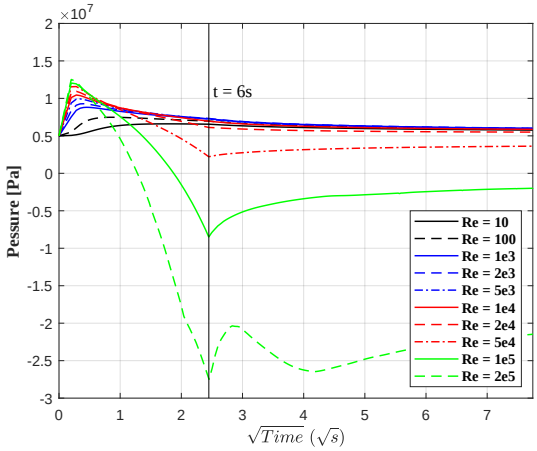

Figure 5.9: Injection pressure for varying injection rates with a model including inertial terms but assuming laminar flow. Fluid velocity rapidly decreases as it moves away from the wellbore. If the kinetic energy of the fluid cannot be dispersed by frictional forces, it gets transferred back into potential energy in the form of pressure. The result is a positive pressure gradient that requires negative injection pressures to satisfy the boundary value problem. Pressure here is measured relative to the hydrostatic pressure, so total pressure remains positive.

Figure 5.10a illustrates the pressure along the fracture when considering the inertial terms with laminar flow compared to the Poiseuille flow solution after 60 s of injection at the highest tested injection rate of $Re = 2 \times 10^5$. Similar to the turbulent flow solution, there is a region of deviation from the Poiseuille flow solution near the wellbore, but it does not extend as far as in the turbulent solution. Approximately 1 m along the fracture, the fluid

returns the pressures are well approximated by the Poiseuille flow profile. Figure 5.10b illustrates the aperture profile along the fracture. The negative pressures at the wellbore induce a decrease in the aperture at the wellbore, which also increases the velocity and thereby exacerbates the influence of the convective term. To conserve the overall injected volume, the fracture is slightly longer than the Poiseuille flow case and the apertures near the tip are slightly larger.

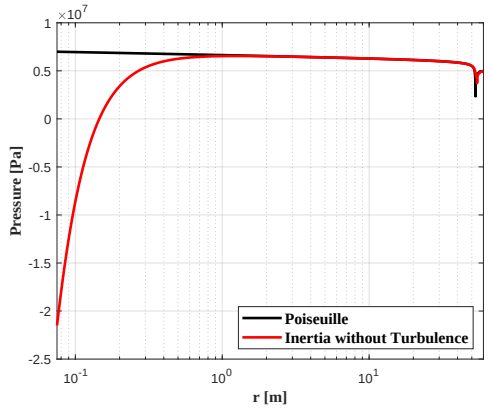

(a) The slowing fluid introduces a positive pressure gradient near the wellbore and creates negative pressures. The effect is localized near the wellbore and the solution returns towards the Poiseuille flow solution within 1 m.

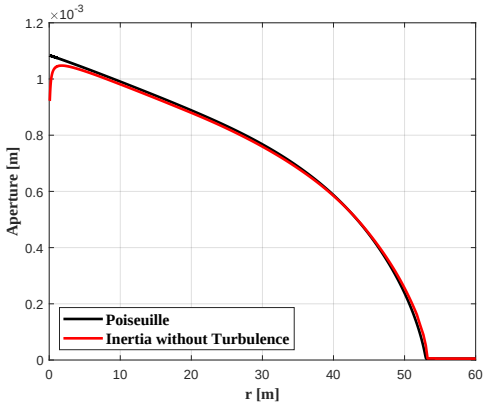

(b) The negative pressures cause a decrease in the aperture near the wellbore. To accommodate the total injected volume, the fracture length must increase.

Figure 5.10: Pressure and aperture along the fracture with a model that includes inertial terms but assumes laminar flow after 60 s of injection with an injection rate of $Re = 2\times10^5$.

5.4.4 The combined effects of inertia and turbulence

Based on the results of the previous sections, we can observe that the two phenomena of inertia and turbulence are in conflict. One seeks to increase pressure and decrease crack length, while the other seeks to decrease pressure and increase crack length. Only by combining the two phenomena into a single model can we observe the true fluid behaviour. Thus we now consider the full GG22 flow model and solve the conservation of momentum equation as

$$\frac{\partial q}{\partial t} + \frac{1}{r}\frac{\partial}{\partial r}\left(r\frac{\alpha}{w}q^2\right) = -\frac{w}{\rho_f}\frac{\partial p}{\partial r} - \frac{f_D(q)}{w^2}q^2 \tag{5.22}$$

Figure 5.11 illustrates the pressure at the wellbore for increasing injection rates. The overall form of the pressure curves is similar to the turbulent-only solution in Figure 5.7, but the peak pressures at $t = 6$ s are reduced. We therefore observe that the turbulent friction factor is dominant at lower Re and the effects of the inertial terms do not manifest

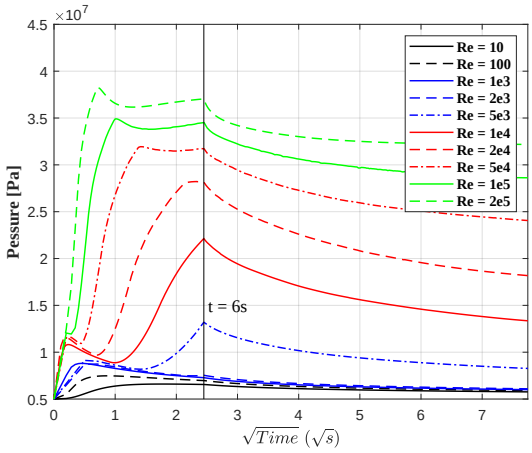

Figure 5.11: Injection pressure for varying injection rates with a model with turbulent and inertial terms. In general, the turbulent solution is dominant, however the influence of the negative pressures from the inertial terms significantly reduce the pressures.

until higher Re, though it has significant effects on the pressure (a reduction of 5 MPa at $t = 6\ s$ for $Re = 2 \times 10^5$).

Figure 5.12a illustrates the pressure along the fracture after 60 s of injection at the highest tested injection rate of $Re = 2 \times 10^5$. The full model pressure generally aligns with the turbulent-only model, though pressures are reduced up to 20% in the vicinity of the wellbore. Figure 5.12b illustrates the aperture along the fracture. The increase in aperture from turbulence reduces the influence of inertia, as the increased aperture at the wellbore results in a lower fluid velocity to maintain the prescribed wellbore flux ($q = \overline{v}w$). The decrease of pressure at the wellbore does not translate directly to the same decrease in aperture, and though it is reduced compared to the turbulent-only model, the reduction is small. We attribute this difference to the fact that aperture and pressure are no longer directly correlated through a constitutive equation and instead are now indirectly correlated through a partial differential equation. The crack length is similar to the turbulent-only model. In all cases, the changes in crack length are very small, on the order of 10^{-3} compared to the overall fracture length.

Figure 5.13 illustrates how the various fluid models affect the distribution of stress in the rock mass. The Poiseuille flow model generates a single stress concentration at the fracture tip. Introducing turbulence generates increased fluid pressure at the wellbore, which in turn increases the stresses in the rock mass at the wellbore. Including inertia but neglecting turbulence causes the pressure to decrease at the wellbore and restricts the wellbore aperture. Echoing the fluid pressure behaviours, the stress concentration induced by the inertial terms is more localized than the stress concentration induced by turbulence. The full GG22 fluid flow model shows stress concentrations at the wellbore, but the magnitude and size of the concentrations are reduced due to the influence of inertia compared to the turbulent-only model.

Figure 5.14a illustrates the pressure at the wellbore after 60 s of injection for various Re. The full flow model deviates from the Poiseuille flow model as soon as turbulence is

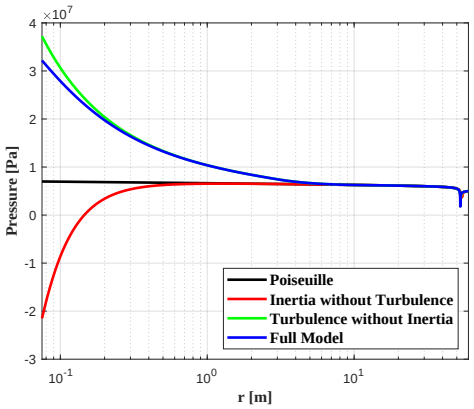

(a) Turbulence is dominant over the inertial terms in the pressure solution but inertia reduces the pressures within $1m$.

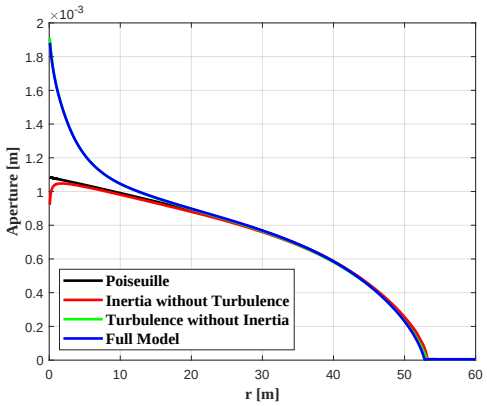

(b) Differences in pressure are significant between turbulent solutions with and without inertia, but the translation to aperture is more modest.

Figure 5.12: Pressure and aperture along the fracture with a with turbulent and inertial terms after 60 s of injection with an injection rate of $Re = 2 \times 10^5$.

induced at $Re \approx 2 \times 10^3$. The full model and the turbulent-only model remain similar up to $Re \approx 2 \times 10^4$, after which the effects of inertia manifest and the full model deviates from the turbulent-only model. Figure 5.14b illustrates the aperture at the wellbore after 60 s of injection time. The full model deviates from the Poiseuille flow model as soon as turbulence is introduced, but the effects of inertia are more modest and differences with the turbulent-only model are small.

Figure 5.15 illustrates the fraction of inertial and turbulent forces to the total pressure drop observed along the fracture. As the inertial and turbulent forces are localized to the wellbore (approximately 2 m or 13 wellbore diameters), this fraction indicates the ratio of entrance losses to the total pressure loss along the fracture. This fraction is calculated as

$$\text{Entrance loss fraction} = \frac{\Delta p_{Full} - \Delta p_{PF}}{\Delta p_{Full}} \tag{5.23}$$

in which Δp_{Full} is the difference between the wellbore pressure from the full GG22 model and the far-field pressure, and Δp_{PF} is the difference between the wellbore pressure from the Poiseuille flow and the far-field pressure. We observe that the majority of the pressure loss that occurs along the fracture is attributable to entrance losses. The fraction of entry losses increases rapidly after turbulence is induced at $Re = 2000$, surpassing 0.5 by $Re = 5000$. It approaches an asymptote of 0.93 at higher Re, though the exact value of this asmptote is likely unique to this specific problem setup. Crack length and injection time do not appear to have a significant impact on the ratio. These results imply that entrance losses, a phenomenon observed experimentally [89] and often attributed to wellbore perforations, may be described wholly or in part by turbulent and inertial forces which develop near the wellbore due to high Re flow conditions. However, true near-wellbore behaviour is a complicated phenomenon, confounded by the flow in the wellbore, the effects

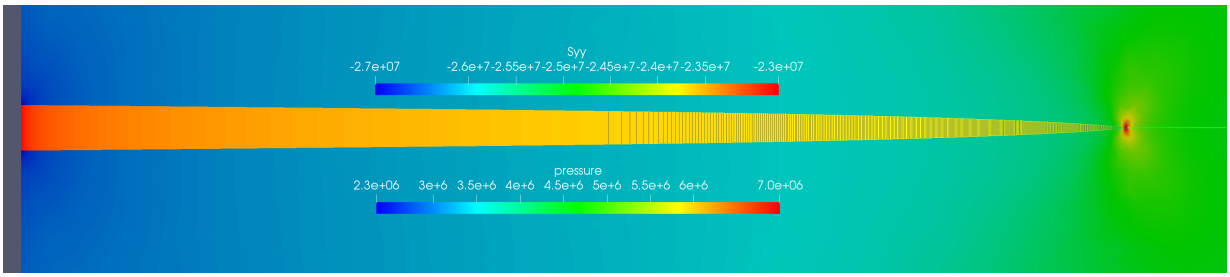

(a) Poiseuille flow model. A stress concentration is observed near the fracture tip.

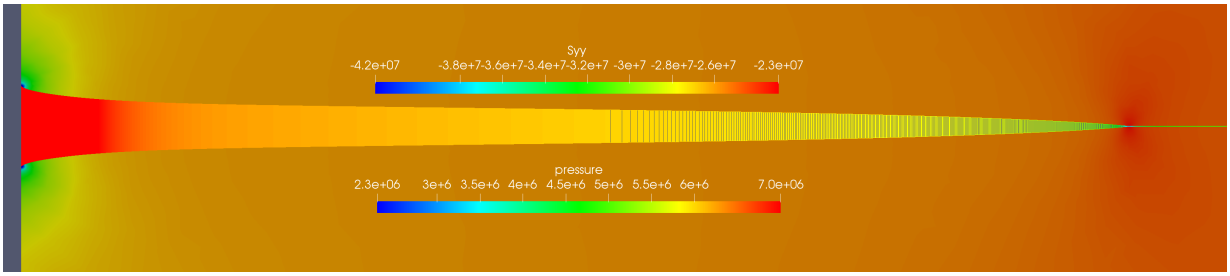

(b) Turbulent-only flow model. The increased fluid pressure at the wellbore creates a stress concentration at the wellbore.

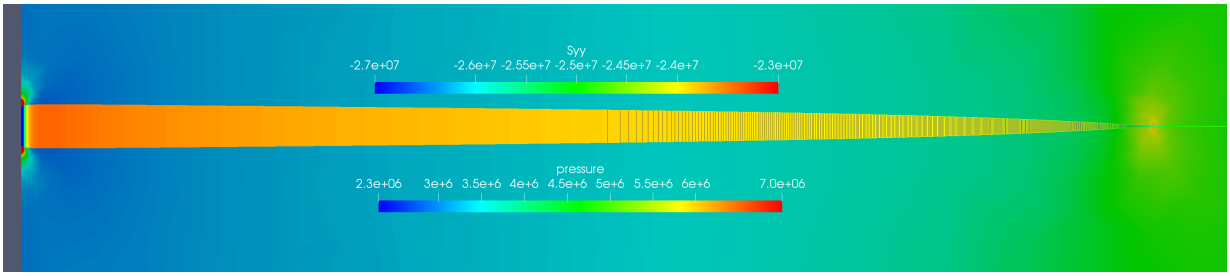

(c) Inertia-only flow model. The decreased fluid pressure at the wellbore creates a stress concentration at the wellbore.

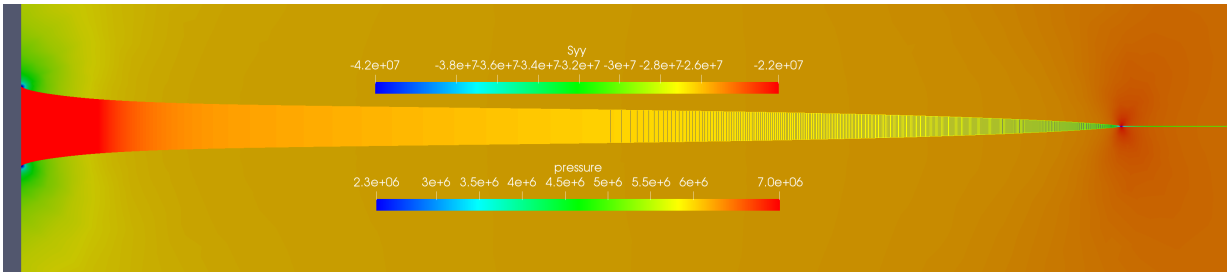

(d) Full GG22 flow model. The interaction of turbulence and inertia decrease the magnitude of the stress concentration at the wellbore compared to the turbulent only model.

Figure 5.13: Rock mass stresses and fluid pressures for an injection rate of $Re = 2 \times 10^5$ for various fluid models after 60 s of injection. Displacements are scaled $\times 2000$.

of perforations, and near-wellbore tortuosity [90]. This model does not capture all these near-wellbore effects but suggests that these effects must be considered in combination with inertia and turbulence to fully capture the near-wellbore behaviour. These results imply that near-wellbore behaviour may govern the wellbore pressure and thus the power required to inject fluid at these high flow rates into the fractures.

With regard to the implications and importance of inertia to the overall fracture propagation, it is concluded in Zia and Lecampion [26] by dimensional analysis that the inertial terms are always negligible, while in Garagash [27] it is concluded that inertial terms are only important in the early-time solution. We have shown that inertia is primarily a near-wellbore effect, so the assumption that inertial terms are negligible is comparable to assuming that near-wellbore effects are negligible as the fracture length increases. In the context of the overall fracture propagation, our results agree with this conclusion, and the scaling arguments presented by Garagash [27] can be used to estimate the importance of inertia to the overall fracture propagation. However, inertia is a phenomenon that occurs relative to the forces over a cross-section, so when concerned with near-wellbore behaviour, the inertial effects are not negligible at high flow rates. Furthermore, the pressure drop along the fracture appears to be dominated by near-wellbore behaviour caused by turbulent and inertial effects. By neglecting this combination effects near the wellbore, it may be possible to predict the overall fracture length, but considerably under- or over-estimate the amount of power (product of flow rate and pressure) required to generate a fracture of that length.

Based on these observations, the following recommendations for the simulation of axisymmetric fractures are proposed. For injection flow of $Re < 2000$, the Poiseuille flow model appears to be adequate. For injection flow rates in the range of $2 \times 10^3 \leq Re \leq 2 \times 10^4$, one should include the effects of turbulence but may neglect the effects of inertia with minimal error. For injection flow rates $Re > 2 \times 10^4$, one should include both the effects of inertia and turbulence. If one is only interested in predicting crack lengths and apertures, it appears that one could apply a higher upper bound on the range of applicability of the turbulent-only model at the cost of over-predicting the pressures. For wellbore diameters of 10, 15, and 20 *cm* (4, 6, 8 *in*), these thresholds correspond to flow rates of 0.24, 0.36, and 0.48 *bpm* for the onset of turbulence effects ($Re \geq 2 \times 10^3$) and 2.4, 3.6, and 4.8 *bpm* for the onset of inertial effects ($Re \geq 2 \times 10^4$) assuming water as the injected fluid.

While the results presented herein are discussed in terms of the dimensionless Re, the system is non-linear so the magnitudes of flow rate and wellbore diameter will have some effect on the results presented. However, the differences in the size of the wellbore that occur in practice are small, and the flow rates pumped through those wellbores scale with wellbore size, so in practice we expect qualitatively similar behaviour without significant differences when considering wellbores sizes other than the 15 *cm* adopted here. Furthermore, these results and recommendation thresholds assume water without additives as the injected fluid. The use of additives in the injected fluid, such as slickwater, which reduce drag and affect the transition from laminar to turbulent flow, will influence these thresholds and the results presented herein may not be applicable.

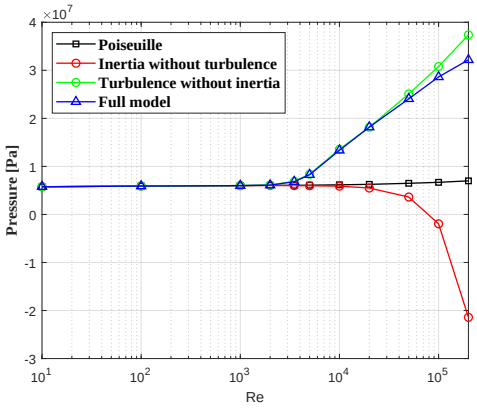

(a) Comparison of wellbore pressures after 60 s. The full physics behaviour departs from the Poiseuille flow solution by $Re = 5000$. The inclusion of turbulence increases the injection pressure by a factor of approximately 4. Including turbulence but neglecting inertia overestimates the required pressure by up to 20% in the tested range.

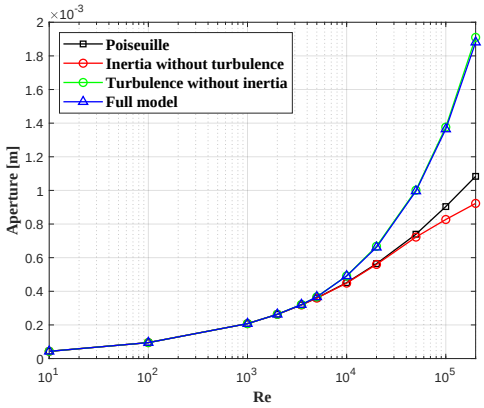

(b) Turbulence increases the pressure at the wellbore which in turn increases the aperture. Despite the large pressure differences that arise by neglecting inertia, this does not translate to the same difference in aperture. Smaller apertures are observed, but the difference is more modest.

Figure 5.14: Pressure and aperture at the wellbore after 60 s of injection for various injection flow rates and models.

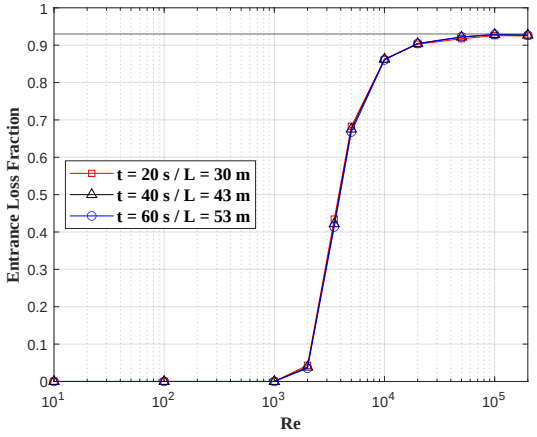

Figure 5.15: Relative contribution of turbulent and inertial forces to the total pressure difference along the fracture. The contribution of turbulent and inertial forces to the pressure difference rapidly increases once turbulence is induced and eventually converges towards an asymptote of 0.93 . Crack length L appears to have little effect on the contribution, but may increase in longer fractures.

5.5 The Effects of Surface Roughness

The friction factor as determined by the Colebrook-White equation is a function of two terms: the relative roughness of the fracture surfaces compared to the aperture, and the Reynolds number. At the Reynolds numbers considered in this analysis, the friction factor is controlled primarily by the surface roughness term. As the flux is not constant along the radius, neither is the friction factor, and the asymptotic friction factor is only reached near the wellbore. As the Colebrook-White equation is primarily applicable in the context of pipe flow, it is important to question the influence of the assumed empirical relationship on the results we are interpreting. The surface roughness we have specified is at the high end of the range of applicability of the Colebrook-White equation, and as rock mass fractures are highly heterogeneous and uneven, the friction factor is likely to be even greater in reality. To stay within the range of applicability of the adopted empirical relationship, let us examine the results using a lower surface roughness.

We consider a very smooth fracture surface with a roughness up to $\epsilon = 10\ \mu m$ and compare it to the earlier results with a surface roughness up to $\epsilon = 500\ \mu m$, which is still small compared to a real rock mass fracture. Figure 5.16 illustrates the wellbore pressures after 60 s of injection time for high and low surface roughness. Both show significantly different behaviour from the Poiseuille flow model and similar trends: they depart from the Poiseuille flow solution as soon as turbulence is induced, and the influence of the inertial terms manifests at higher Re than the influence of turbulence. The influence of the inertial terms is greater in the low roughness case as the smaller pressures create smaller apertures and therefore higher fluid velocities and greater inertial effects. The departure of the full model from the turbulent-only model therefore occurs at lower Re than the high roughness case. Nevertheless, it shows that even with smooth fracture faces, the influence of turbulence and inertia cannot be neglected, and with larger roughnesses the findings presented herein are only reinforced.

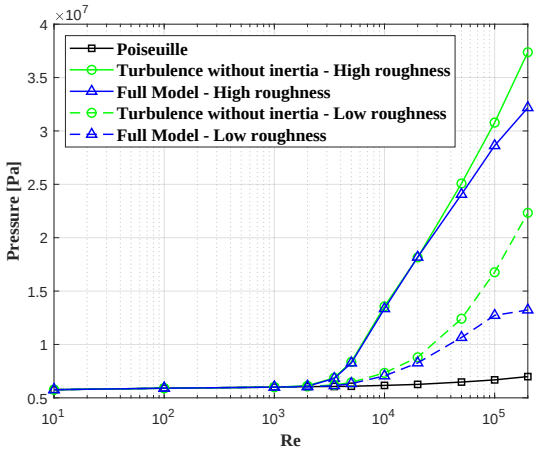

Figure 5.16: The influence of the surface roughness term on wellbore pressure after 60 s of injection.

5.6 The Effects of Fracture Toughness

Thus far, we have considered the reopening of a fracture for the model problem described in Section 5.3 for a zero-toughness fracture. In this section we will introduce fracture toughness through a cohesive fracture process zone ahead of the fracture with a cubic traction separation law.

Consider the definitions of the dimensionless viscous and toughness coefficients defined by Detournay [40]. The dimensionless viscous storage coefficient is proportional to

$$\mathcal{M} \propto \frac{\mu E^3 Q_o}{K_{Ic}^4} \propto \frac{\mu E^3 Q_o}{G_c^2} \propto \frac{\mu^2 E^3 Re}{\rho_f G_c^2} \tag{5.24}$$

while the dimensionless toughness coefficient is proportional to

$$\mathcal{K} \propto \frac{K_{Ic}}{(E\mu Q_0)^{\frac{1}{4}}} \propto \frac{G_c^{\frac{1}{2}}}{(E\mu Q_0)^{\frac{1}{4}}} \propto \frac{G_c^{\frac{1}{2}} \rho_f^{\frac{1}{4}}}{(E\mu^2 Re)^{\frac{1}{4}}} \tag{5.25}$$

where K_{IC} is the mode I fracture toughness of the rock mass. The two dimensionless coefficients are inversely proportional to each other, such that one decreases as the other increases. The viscous and toughness coefficients $\mathcal{M}$ and $\mathcal{K}$ are derived for Poiseuille flow fracture asymptotics, and so are not directly applicable to the model we consider here, and are rather used in analogy. As the viscous coefficient is proportional to the injection flow rate, Q_o, it seems likely that any fracture in which the flow rate is high enough to induce turbulent effects will also be a viscous dominant fracture. We therefore hypothesize that applications concerned with toughness dominant fractures need not consider turbulent effects.

The numerical results provide evidence to support this hypothesis. Figure 5.17a illustrates the wellbore pressure and Figure 5.17b illustrates the wellbore aperture as functions of the injection rate after 60 s of injection with the full fluid model for fracture energies of $G_c = 0,\ 250,\ 500\ J/m^2$. The fracture energies considered are very high for a brittle rock formation, but we consider high fracture energies to examine the asymptotic case and increase the toughness coefficient at high injection rates. At low Re, the pressure at the wellbore is governed by the pressure required to overcome the cohesive forces, i.e., toughness dominated, and pressure is correlated with fracture energy. At high Re, the pressure at the wellbore is correlated to the turbulent resistance of the fluid, i.e., storage dominated. At these higher Re, the cohesive tractions restrict the ability of the fracture to grow, resulting in shorter fractures with larger apertures which create less resistance to flow and resulting in lower pressures, such that pressure is inversely correlated with fracture energy. The cross-over between these two regimes occurs near the onset of turbulent flow. Both the pressures and aperture imply that at higher Re, even for rock masses with large toughness, fracture propagation in the GG22 model becomes dominated by turbulence rather than toughness or viscosity and the solutions converge towards the zero-toughness solution.

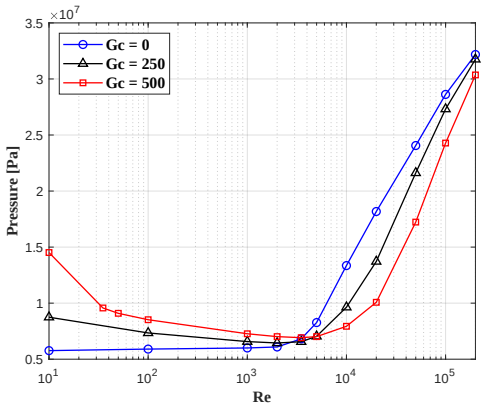

(a) Injection pressure after 60 s. At low Re, the pressure is correlated to fracture toughness. At high Re, the pressure is governed by the fluid resistance.

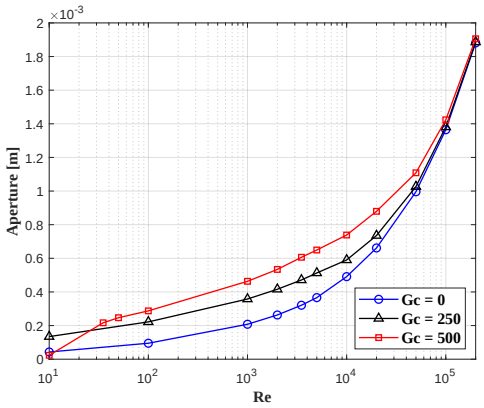

(b) Wellbore aperture after 60 s. At low Re, the cohesive tractions restrict fracture growth and cause the aperture to increase to maintian the overall injected volume. At Gc = 500 and Re = 10, the fluid forces are not capable of overcoming the cohesive tractions and the fracture does not open.

Figure 5.17: Pressure and aperture at the wellbore for various fracture energies (G_c, J/m^2). Though the fracture toughness create different responses at low Re, high injection rates cause the fractures to become viscosity dominant.

5.7 The Effects of Friction Reducers (Slickwater)

It is common in hydraulic fracturing treatments to use slickwater to reduce the energy of pumping the fracturing fluid down the wellbore [86]. The polymers introduced in slickwater delay the onset of turbulent flow from $Re \approx 2\times10^3$ to $Re \approx 3\times10^4$ [85] at the cost of higher viscosity, $\mu = 5mPa \cdot s$ [87]. In this section we examine how turbulent and inertial effects manifest in slickwater for the zero-toughness fracture problem ($G_c = 0\ J/m^2$) described in Section 5.3.

Figure 5.18 illustrates the pressure at the wellbore for increasing injection rates. While the behaviour is different from the water cases, the various terms in the governing equation produce the same effects. In the laminar regime, water and slickwater exhibit the same behaviour. As the slickwater enters the MDR regime ($10^3 < Re < 3 \times 10^4, f_D \propto Re^{-0.7}$), we observe a reduction in pressure at the wellbore. Much like the case of inertia without turbulence discussed in Section 5.4.3, the slowing fluid supplies energy faster than it is dissipated by friction, so a positive pressure gradient develops at the wellbore. As the injection flow rate continues to increase, the pressure at the wellbore increases after the MDR regime decrease. It enters the transitional regime ($3 \times 10^4 < Re < 5 \times 10^5$), which increases the friction factor and causes a positive pressure gradient to develop.

Thus, while turbulence was the dominant effect at lower Re in pure water and inertia did not become important until higher Re, we draw the opposite conclusion in slickwater. In slickwater, inertia is the dominant effect at lower Re and turbulence only becomes

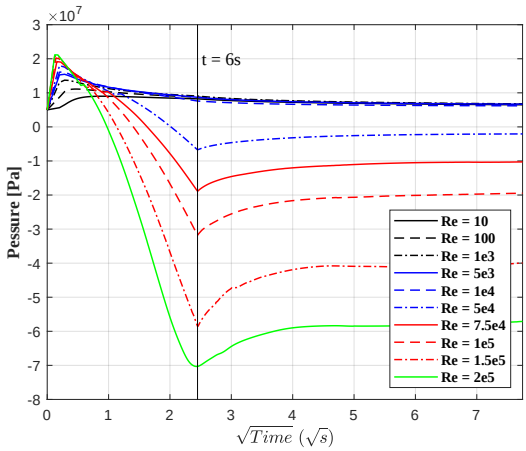

Figure 5.18: Injection pressure for various injection rates with slickwater considering the full GG22 model. The higher viscosity of slickwater implies larger flow rates at the same Reynolds number, creating inertia dominant flow and producing a positive pressure gradient at the wellbore which reduces pressure.

important at higher Re. Figure 5.19a illustrates the pressure at the wellbore after 60 s of injection for various Re and models with slickwater. While the MDR regime begins at $Re > 1000$, we observe that Poiseuille is a reasonably good approximation until $Re \approx 5 \times 10^3$. At $Re > 5 \times 10^3$, after which inertia creates deviations from the Poiseuille flow solution. Figure 5.19b compares the wellbore pressures for the full GG22 model between water and slickwater. The higher viscosity of slickwater implies that a larger flow rate of slickwater is required to produce the same Reynolds number, thus at low Re the slickwater pressures are increased compared to water. The larger flow rates increase the inertial effects, causing inertia to be the dominant mechanism in the wellbore pressure at large flow rates. In a similar but inverted case to water, turbulence and inertia are in opposition. Each mechanism moderates the other at high Reynolds numbers and turbulence reduces the magnitude of wellbore pressure by 50% in high Re slickwater flow. Turbulence leads to deviations from the inertia-only solution at $Re > 2 \times 10^4$. Figure 5.19c illustrates the wellbore pressures for various models as a function of flow rate. Slickwater successfully reduces the power needed to pump fluid down the wellbore at the same flow rate, and inertial effects are not observed until flow rates of 0.7 m^3/min (11 L/s, 4.5 bpm).

Figure 5.20a illustrates the pressure along the fracture after 60 s of injection at a rate of $Re = 5 \times 10^4$ for both water and slickwater. Figure 5.20b illustrates the aperture along the fracture. The larger viscosity of slickwater creates longer fractures with larger apertures and higher pressures away from the wellbore, but the shape of the solution is similar to the inertia-only model with water. The amplified inertial effects increase the aperture of the fracture near the tip. As the model is non-linear, the 5× increase in viscosity and flow rate correspond to an approximately 5× increase in fracture volume, but only a 2× increase in pressure.

The trends observed with slickwater do not substantially change when a fracture toughness is re-introduced. Similar trends to those observed with water in Section 5.6 are observed: at

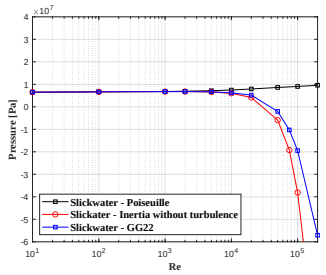

(a) Wellbore pressure as a function of Re.

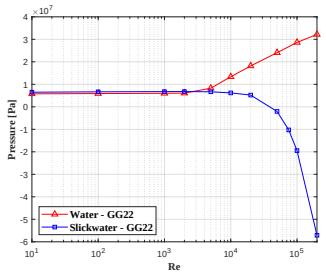

(b) Water and slickwater as a function of Re.

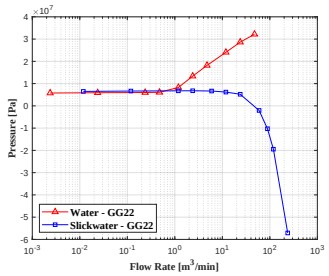

(c) Water and slickwater as a function of Q.

Figure 5.19: Wellbore pressure after 60 s of injection with water and slickwater.

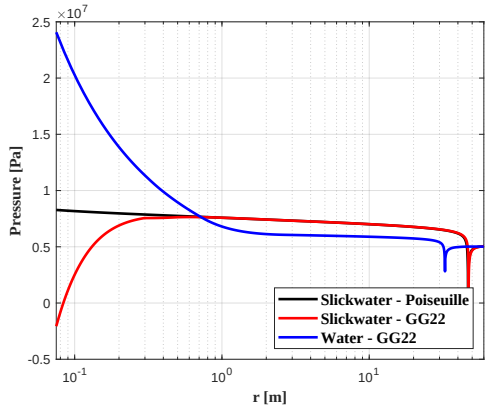

(a) Pressure in the fracture is greater and inertial effects dominate near the wellbore with slickwater.

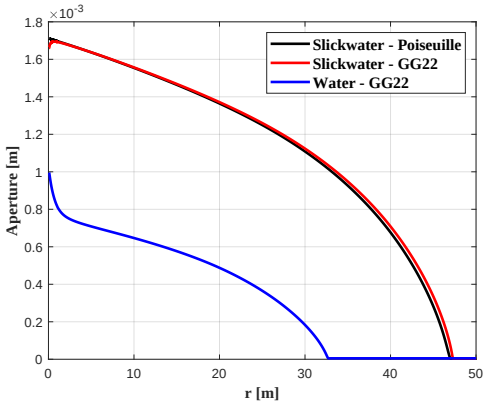

(b) The larger flow rate results in a larger fracture with an area of reduced aperture near the wellbore due to inertial effects.

Figure 5.20: Comparison of pressure and aperture along the fracture with water and slickwater after 60 s of injection with an injection rate of $Re = 5 \times 10^4$.

the flow rates large enough to induce inertial and turbulent effects, the fracture propagation is pushed away from toughness dominant propagation and is instead dominated by fluid behaviours.

5.8 Conclusions

In this chapter, the effects of inertia and turbulence on the hydraulic stimulation of fractured rock masses have been investigated. The phenomena of inertia and turbulence are significant near the wellbore where the flux is greatest. As the flow disperses into the fracture, laminar flow is recovered and Poiseuille flow is well-suited to modelling the flow behaviour. At the fracture tip, no inertial or turbulent effects are observed due to the low flow rates.

The development of turbulence leads to significant increases in the injection pressure and the formation of an area of increased aperture near the wellbore relative to the Poiseuille

flow solution. Pressure and aperture are no longer simply correlated because they are now indirectly related through a partial differential equation rather than directly related through a constitutive equation. These significant changes in wellbore aperture and pressure translate to only small changes in overall crack length. While turbulence increases wellbore pressure, inertia at high flow rates reduces wellbore pressure and a model which only includes turbulence leads to an overestimation of the injection pressure. Turbulence is generally the dominant phenomenon, causing deviations from the Poiseuille flow solution as soon as it is induced, at an injection Reynolds number of $Re \approx 2 \times 10^3$, approximately corresponding to a flow of 0.4 *bpm*. Inertial effects do not manifest until higher Reynolds numbers, deviating from a turbulent-only model at Reynolds numbers approximately one order of magnitude higher than the onset of turbulence, $Re \approx 2 \times 10^4$, approximately corresponding to a flow of 4 *bpm*. Inertial and turbulent forces manifest primarily within 2 m of the wellbore (13 wellbore diameters) and are responsible for up to 93% of the total pressure loss along the fracture. This suggests that inertial and turbulent forces may provide a more accurate description for entrance losses, an experimentally observed phenomenon which were previously accounted for in an empirical manner. Increasing surface roughness exacerbates turbulent effect and delays the onset of inertial effects. Flow rates large enough to induce turbulent effects also drive the fracture propagation regime towards viscous dominance and it appears unlikely that turbulent effects would manifest in toughness-dominant fracture propagation regimes.

Using slickwater as the injected fluid, the opposite trend is observed. Slickwater delays the onset of turbulence but not inertia, so reductions in wellbore pressure from the Poiseuille flow solution due to inertia are observed at a Reynolds number of $Re \approx 5 \times 10^3$ (approximate flow rate of 5 *bpm*). Turbulent effects in slickwater begin to manifest at $Re \approx 2 \times 10^4$ (approximate flow rate of 18 *bpm*).

Chapter 6

Conclusions

6.1 Concluding Remarks

In this thesis, a gap in the available models to capture fracture flow behaviour was identified and a new fracture flow model that balances physical processes with complexity was developed. The model was verified against existing models, and numerical methods were developed to solve the model on its own and with hydro-mechanical coupling. The new flow model reveals how inertial and turbulent phenomena manifest near the wellbore of traditional hydraulic stimulation setups.

The GG22 model is derived from the Navier-Stokes equations by integrating over the aperture and making simplifying assumptions. It is therefore not predicated on the same innate assumptions as the Poiseuille flow model and thus contains additional terms that allow it to capture inertial, transient, and turbulent flow behaviours. However, the increased capacity is accompanied by more complexity. While Poiseuille flow reduces to a single constitutive equation, the GG22 model consists of two separate partial differential equations which must be simultaneously satisfied. The GG22 model still significantly decreases complexity compared to the full Navier-Stokes equations. It is demonstrated that the GG22 model conserves energy in non-parallel apertures while the Poiseuille flow model does not. Furthermore, the GG22 model contains the Poiseuille flow model within its solution space, such that when the Poiseuille flow model is appropriate, the Poiseuille flow solution is recovered. Thus, there exists no case in which the GG22 model makes worse predictions than the Poiseuille flow model, as it is an expansion of the more common model. Neither model performs well when fundamentally two-dimensional phenomena arise across the fracture aperture, such as stable eddy formation.

Regarding numerical methods, while the formulations required to solve the GG22 model are undeniably more complex, the computational effort is overall comparable to Poiseuille flow models. With regards to hydro-mechanical coupling, the GG22 model is subject to many of the same issues as Poiseuille flow, so monolithic solution methods or clever sequential methods are still required. With regards to computation time, the numerical formulations of the GG22 model do not explicitly include the notorious cubic non-linearity that is characteristic of Poiseuille flow and the inertial terms provide stabilizing numerical

effects, so many problems (particularly elastic fractures) converge faster than the Poiseuille flow model. Convergence issues only arise when the GG22 model is paired with the cohesive fractures, an issue which is less pronounced in Poiseuille flow models. While the convergence issues observed with the GG22 model in planar cohesive fractures are severe, it is noteworthy that this computational difficulty does not persist into the axisymmetric models.

In practice, inertial, transient, and tuburlent behaviours are likely to be more common than currently considered. Poiseuille flow is a reasonable model for natural fracture flows and near-tip behaviour, but is very poor for capturing near-wellbore behaviour. Any simulation of flow in a radial fracture from a wellbore using water as the injection fluid should at the very least include turbulent behaviour. The threshold of departure from the standard Poiseuille flow solution is low, and the change in fracture geometry and flow behaviour is large. The threshold to induce inertial effects in water is also relatively low, and simulations dealing with higher injection Reynolds numbers should consider the implementation of inertia to capture the complete fluid behaviour. While Poiseuille flow is better at approximating slickwater behaviour, any simulation of flow in a radial fracture from a wellbore using slickwater should consider including inertial behaviour. The threshold for considering turbulent behaviours in slickwater is higher, so they may be neglected with minimal impact at modest flow rates. In traditional hydraulic stimulation applications, the driving force behind deviations from the Poiseuille flow solution appears to be flow rate. There are various other factors that can lead to non-Poiseuille flow behaviour, as explored in the various verification cases. For example, larger apertures like those of a geothermal installation lead to greater transient effects, and any sudden aperture change can induce inertial forces. In general, the influence of inertia, transience, and turbulence are expected to result in larger pressures, lower fluxes, greater stresses, and phase-shifts in the fluid response.

6.2 Research Contributions

In the development of the GG22 model and its applications, research contributions that expand the literature on non-Poiseuille flow processes in fractured rock masses were produced. The significant contributions produced by this research were disseminated in conferences and peer-reviewed journals and are summarized here.

The first objective of this thesis was to develop a new reduced-dimension model for fracture flow that captures inertial, transient, and turbulent behaviours. This research was disseminated in:

B. Gee and R. Gracie, "Beyond Poiseuille flow: A transient energy-conserving model for flow through fractures of varying aperture", *Advances in Water Resources*, vol. 164, p. 104192, 2022.

B. Gee and R. Gracie, "Reduced Dimension Fracture Flow – Deformable fractures coupled with inertial and transient fluid behaviour", *The 8th European Congress on Computational Methods in Applied Sciences and Engineering.* Oslo, Norway, June 2022.

B. Gee and R. Gracie, "Inertia Dominant and Transient Flow in Fractures – Beyond the Cubic Law", *56th US Rock Mechanics/Geomechanics Symposium.* ARMA. Santa Fe, NM, June 2022.

The key contributions of this work are:

- A new mathematical fracture flow model is derived from the Navier-Stokes equations by integating over the aperture and making simplifying assumptions.
- The performance of the new model is verified against the Navier-Stokes and Poiseuille flow models.
- The error in using reduced-dimension models is quantified at various flow rates in sinusoidal geometries.

The second objective of this thesis was to develop a simulator with novel numerical methods to solve the new fracture flow equations and simulate flow behaviour in rigid fractures. This research was disseminated in:

B. Gee and R. Gracie, "Beyond the cubic law: A finite volume method for convective and transient fracture flow," *International Journal for Numerical Methods in Fluids*, vol. 94, no. 11, pp. 1841–1862, 2022.

B. Gee and R. Gracie, "Reduced Dimension Fracture Flow – Deformable fractures coupled with inertial and transient fluid behaviour", *The 8th European Congress on Computational Methods in Applied Sciences and Engineering.* Oslo, Norway, June 2022.

The key contributions of this work are:

- The first numerical method to solve the GG22 equations is developed. An explicit finite volume solution algorithm with a continuity correction is presented to overcome numerical instabilities.
- The types of behaviours to be expected by inertial and transient flow are illustrated. These effects include lower fluxes, higher pressures, and phase-shifts in the fluid response.

The third objective of this thesis was to develop a multi-physics simulator to couple the new fracture flow model with rock mass deformation and fracture propagation. This research was disseminated in:

B. Gee and R. Gracie, "Inertial and turbulent flow in hydro-mechanically coupled planar fractures," Submitted to *International Journal for Numerical and Analytical Methods in Geomechanics*, February 2023.

R. Gracie and B. Gee, "Non-cubic law behavior in hydraulic fractures", 56th US Rock Mechanics/Geomechanics Symposium. ARMA. Santa Fe, NM, June 2022.

B. Gee, R. Gracie, and M.B. Dusseault, "Transient, Inertial, and other non-Cubic Law Phenomena", 3rd International Conference on Coupled Processes in Fractured Geological Media. Berkeley, CA, November 2022.

The key contributions of this work are:

- The first hydro-mechanical model for the GG22 equations coupled with rock mass deformation and fracture propagation is developed.
- A monolithic implicit solution algorithm is presented. Numerical convergence issues are addressed by introducing Aitken relaxation and adaptive line search techniques. The line search is demonstrated to be superior to a Newton-Raphson scheme.
- Previous modelling assumptions on inertia are verified and inertia is demonstrated to be negligible in KGD-like fractures. Previous findings on turbulent effects are verified and it is demonstrated that they have significant impacts on the shape of the fracture.

The fourth objective of this thesis was to investigate the role of inertia and turbulence in hydraulic stimulation and fracture propagation. This research was disseminated in:

B. Gee and R. Gracie, "The Influence of Turbulence and Inertia in Radial Fracture Flow," Submitted to *International Journal of Solids and Structures*, April 2023.

B. Gee. "Beyond the cubic law: Inertial, turbulent, and transient flow behaviours in hydraulic fractures". *American Rock Mechanics Association (ARMA) Hydraulic Fracturing Technical Seminar Presentation*, March 9th 2023.

The key contributions of this work are:

- The axisymmetric form of the GG22 equations is presented for the first time.
- The role of inertia and its interactions with turbulence is presented for the first time. Inertia is shown to have significant impacts on pressure and aperture in the vicinity of the wellbore. Inertia and turbulence are demonstrated to be at odds, as turbulence increases wellbore pressure while inertia deceases wellbore pressure.

6.3 Directions for Future Study

There are many new potential avenues for future study on inertial, transient, and turbulent flow in fractures. Some of these directions include:

Validation: Validation with experimental results is one of the largest remaining challenges. The combination of high flow rates with deformable apertures under high in-situ stresses leads to complex interactions and scale effects that are difficult to replicate at the lab scale. Validation with field data remains a significant challenge due to the high uncertainty and heterogeneity of rock masses. There has been experimental work performed to examine and validate Poiseuille and Forchheimer flow, and similar experimental setups could be leveraged to examine and validate the GG22 model at lower Reynolds numbers. Of particular interest might be a survey of existing experimental data to see if any unexplained phenomena could be attributed to effects captured by the GG22 model. Further design and refinement of experimental testing is recommended to validate the GG22 model and establish an experimentally verified range of applicability.

Model Extensions: There are several physical behaviours which the GG22 model cannot currently capture but are of interest for practical applications. These include fluid leak-off, fracture tortuosity, fluid compressibility, and fluid temperature among others.

Leak-off is the loss of fluid through the walls of the fracture. Leak-off is a phenomenon observed in the field and one which is important to predicting the behaviour of hydraulic stimulation and other fracture flow applications. This is commonly incorporated into the Poiseuille flow model through the conservation of mass, despite the Poiseuille flow assumption that the rock matrix is impermeable. To include leak-off in a mathematically consistent manner requires intrusion into the derivation of the GG22 governing equations, as it too assumes an impermeable rock mass. Such an extension would permit the GG22 model to be coupled with porous rock masses.

Fracture tortuosity is the concept that the centerline of the fracture follows a curved path, rather than a straight line or plane. Including tortuosity likely requires the re-derivation of the governing equations with respect to an arbitrary curved centerline. I suspect this would introduce new inertial terms associated with changing the flow path, and there are likely to be limits on the tortuosity and flow rate before a reduced-dimension model is inadequate. Such an extension would permit the GG22 model to capture non-mated fractures, which are a more accurate depiction of natural fractures.

Fluid compressibility is the concept that fluid density may change in response to temperature or pressure. Fluid compressibility is likely to be one of the easier extensions to the GG22 model as the assumption that density is constant is not critical. The resulting formulation would appear similar to the GG22 equations, except density would appear inside the transient and convective terms. This would form a three-field model where density is introduced as a function of time and space. A third governing equation, an equation of state, would be required to dictate how the density responds to changes in pressure or temperature. Temperature can be included in a similar fashion by introducing a governing equation associated with the conservation of energy and a temperature dependent friction factor. Such an extensions would be of particular interest to applications such as heat mining with supercritical carbon dioxide.

Non-Newtonian fluid rheology is a more complex extension. Non-Newtonian rheology will only manifest in the friction term, but it is likely that a complete re-derivation of the friction term following the methodology laid out in Chapter 2 is required for a new rheology of interest. This would allow the GG22 model to properly capture behaviours like shear-thinning that occur in slickwater, among other fracturing fluids.

Fracture Planes: The research presented in this thesis focused primarily on the one-dimensional form of the GG22 equations and fracture planes were only investigated under axisymmetric conditions. Fracture planes are of interest in hydraulic stimulation but also in applications such as geothermal energy. The complexity of the equations is significantly elevated by the introduction of a flux dyad, such that the equations are similar to the compressible Navier-Stokes equations in which aperture is a proxy for density. New numerical methods are required to solve the GG22 equations in this form, and the extension from one- to two-dimensions is non-trivial. The GG22 model in fracture planes is expected to unveil a myriad of new behaviours, such as in-plane re-circulation, which may have profound impacts on heat transfer and rock mass deformation in fractures at high flow rates.

Other Applications: This research has focused primarily on applications to hydraulic stimulation. The GG22 model should be applied to other fracture flow problems to examine the importance of inertia, transience, and turbulence. Other such applications might include but are not limited to: geothermal energy, hydraulic stimulation with pressure pulses, particle and contaminant transport during seismic excitation, and flow through fracture networks.

References

[1] R. A. Nelson and J. Handin, "Experimental study of fracture permeability in porous rock," *American Association of Petroleum Geologists Bulletin*, vol. 61, no. 2, pp. 227–236, 1978.

[2] D. Tang, E. Frind, and E. Sudicky, "Contaminant transport in fractured porous media: analytical solution for a single fracture," *Water Resources Research*, vol. 17, 1981.

[3] J. E. Elkhoury, A. Niemeijer, E. E. Brodsky, and C. Marone, "Laboratory observations of permeability enhancement by fluid pressure oscillation of in situ fractured rock," *Journal of Geophysical Research: Solid Earth*, vol. 116, no. B2, pp. B02311/1–n/a, 2011.

[4] M. Manga, I. Beresnev, E. E. Brodsky, J. E. Elkhoury, D. Elsworth, S. E. Ingebritsen, D. C. Mays, and C.-Y. Wang, "Changes in permeability caused by transient stresses: Field observations, experiments, and mechanisms," *Reviews of Geophysics*, vol. 50, no. 2, 2012.

[5] A. A. Osiptsov, "Fluid mechanics of hydraulic fracturing: A review," *Journal of Petroleum Science & Engineering*, vol. 156, pp. 513–535, 2017.

[6] S. Pandey, V. Vishal, and A. Chaudhuri, "Geothermal reservoir modeling in a coupled thermo-hydro-mechanical-chemical approach: A review," *Earth-Science Reviews*, vol. 185, pp. 1157–1169, 2018.

[7] B. Lecampion, A. Bunger, and X. Zhang, "Numerical methods for hydraulic fracture propagation: A review of recent trends," *Journal of Natural Gas Science and Engineering*, vol. 49, pp. 66–83, 2018.

[8] P. Witherspoon, J. S. Wang, K. Iwai, and J. E. Gale, "Validity of Cubic Law for fluid flow in a deformable rock fracture," *Water Resources Research*, vol. 16, no. 6, pp. 1016–1024, 1980.

[9] R. Zimmerman and G. Bodvarsson, "Hydraulic conductivity of rock fractures," *Transport in Porous Media*, vol. 23, no. 1, 1996.

[10] J. R. Murphy and N. R. Thomson, "Two-phase flow in a variable aperture fracture," *Water Resources Research*, vol. 29, no. 10, pp. 3453–3476, 1993.

[11] H.-B. Lee, I. W. Yeo, and K.-K. Lee, "The modified reynolds equation for non-wetting fluid flow through a rough-walled rock fracture," *Advances in Water Resources*, vol. 53, pp. 242–249, 2013.

[12] E. V. Dontsov and A. P. Peirce, "Slurry flow, gravitational settling and a proppant transport model for hydraulic fractures," *Journal of Fluid Mechanics*, vol. 760, pp. 567–590, 2014.

[13] E. Rivas and R. Gracie, "A monolithic coupled hydraulic fracture model with proppant transport," *Computer Methods in Applied Mechanics and Engineering*, vol. 372, p. 113361, 2020.

[14] D. J. Brush and N. R. Thomson, "Fluid flow in synthetic rough-walled fractures: Navier-Stokes, Stokes, and local cubic law simulations," *Water Resources Research*, vol. 39, no. 4, p. 1085, 2003.

[15] M. Javadi, M. Sharifzadeh, and K. Shahriar, "A new geometrical model for non-linear fluid flow through rough fractures," *Journal of hydrology (Amsterdam)*, vol. 389, no. 1, pp. 18–30, 2010.

[16] D. Crandall, G. Ahmadi, and D. H. Smith, "Computational modeling of fluid flow through a fracture in permeable rock," *Transport in porous media*, vol. 84, no. 2, pp. 493–510, 2010.

[17] L. Durlofsky, K. Aziz, and M. Karimi-Fard, "An efficient discrete-fracture model applicable for general-purpose reservoir simulators," *SPE journal (Society of Petroleum Engineers (U.S.) : 1996)*, vol. 9, no. 2, pp. 227–236, 2004.

[18] R. Ahmed, M. Edwards, S. Lamine, B. Huisman, and M. Pal, "Control-volume distributed multi-point flux approximation coupled with a lower-dimensional fracture model," *Journal of computational physics*, vol. 284, pp. 462–489, 2015.

[19] M. Parchei Esfahani and R. Gracie, "On the undrained and drained hydraulic fracture splits," *International Journal for Numerical Methods in Engineering*, vol. 118, no. 12, pp. 741–763, 2019.

[20] S. Salimzadeh, A. Paluszny, H. M. Nick, and R. W. Zimmerman, "A three-dimensional coupled thermo-hydro-mechanical model for deformable fractured geothermal systems," *Geothermics*, vol. 71, pp. 212–224, 2018.

[21] B. Gee, R. Gracie, and M. B. Dusseault, "Multiscale short-circuiting mechanisms in multiple fracture enhanced geothermal systems," *Geothermics*, vol. 94, 2021.

[22] B. Berkowitz, "Boundary conditions along permeable fracture walls: Influence on flow and conductivity," *Water Resources Research*, vol. 25, no. 8, pp. 1919–1922, 1989.

[23] R. Mohais, C. Xu, P. A. Dowd, and M. Hand, "Permeability correction factor for fractures with permeable walls," *Geophysical Research Letters*, vol. 39, no. 3, 2012.

[24] N. Hosseini and A. R. Khoei, "Modeling fluid flow in fractured porous media with the interfacial conditions between porous medium and fracture," *Transport in Porous Media*, vol. 139, no. 1, pp. 109–129, 2021.

[25] E. V. Dontsov, "Tip region of a hydraulic fracture driven by a laminar-to-turbulent fluid flow," *Journal of Fluid Mechanics*, vol. 797, 2016.

[26] H. Zia and B. Lecampion, "Propagation of a height contained hydraulic fracture in turbulent flow regimes," *International Journal of Solids and Structures*, vol. 110-111, pp. 265–278, 2017.

[27] D. I. Garagash, "Transient solution for a plane-strain fracture driven by a shear-thinning, power-law fluid," *International Journal for Numerical and Analytical Methods in Geomechanics*, vol. 5, no. 8, pp. 1439–1475, 2006.

[28] F.-E. Moukhtari and B. Lecampion, "A semi-infinite hydraulic fracture driven by a shear-thinning fluid," *Journal of Fluid Mechanics*, vol. 838, pp. 573–605, 2018.

[29] M. Parchei-Esfahani, B. Gee, and R. Gracie, "Dynamic hydraulic stimulation and fracturing from a wellbore using pressure pulsing," *Engineering Fracture Mechanics*, vol. 235, p. 107152, 2020.

[30] S. R. Brown, "Simple mathematical model of a rough fracture," *Journal of Geophysical Research: Solid Earth*, vol. 100, no. B4, pp. 5941–5952, 1995.

[31] K. Nazridoust, G. Ahmadi, and D. H. Smith, "A new friction factor correlation for laminar, single-phase flows through rock fractures," *Journal of Hydrology (Amsterdam)*, vol. 329, no. 1-2, pp. 315–328, 2006.

[32] X. He, M. Sinan, H. Kwak, and H. Hoteit, "A corrected cubic law for single-phase laminar flow through rough-walled fractures," *Advances in Water Resources*, vol. 154, pp. 103984–, 2021.

[33] R. Zimmerman, S. Kumar, and G. Bodvarsson, "Lubrication theory analysis of the permeability of rough-walled fractures," *International Journal of Rock Mechanics and Mining Sciences & Geomechanics Abstracts*, vol. 28, no. 4, pp. 325–331, 1991.

[34] B. Gee and R. Gracie, "Comparison of fully-coupled and sequential solution methodologies for enhanced geothermal systems," *Computer Methods in Applied Mechanics and Engineering*, vol. 373, p. 113554, 2021.

[35] R. Zimmerman, A. Al-Yaarubi, C. Pain, and C. Grattoni, "Non-linear regimes of fluid flow in rock fractures," *International Journal of Rock Mechanics and Mining Sciences*, vol. 41, no. 3, pp. 384–384, 2004.

[36] P. Ranjith and D. Viete, "Applicability of the 'cubic law' for non-Darcian fracture flow," *Journal of Petroleum Science & Engineering*, vol. 78, no. 2, pp. 321–327, 2011.

[37] R. Liu, B. Li, and Y. Jiang, "Critical hydraulic gradient for nonlinear flow through rock fracture networks: The roles of aperture, surface roughness, and number of intersections," *Advances in Water Resources*, vol. 88, pp. 53–65, 2016.

[38] L. Yu, R. Liu, and Y. Jiang, "A review of critical conditions for the onset of nonlinear fluid flow in rock fractures," *Geofluids*, vol. 2017, pp. 1–17, 2017.

[39] P. Forchheimer, "Wasserbewegung durch boden [movement of water through soil]," *Zeitschrift fur Acker und Pflanzenbau*, vol. 49, pp. 1736–1749, 1901.

[40] E. Detournay, "Propagation regimes of fluid-driven fractures in impermeable rocks," *International journal of geomechanics*, vol. 4, no. 1, pp. 35–45, 2004.

[41] B. Gee and R. Gracie, "Beyond Poiseuille flow: A transient energy-conserving model for flow through fractures of varying aperture," *Advances in Water Resources*, vol. 164, p. 104192, 2022.

[42] M. S. Olufsen, C. S. Peskin, W. Y. Kim, E. M. Pedersen, A. Nadim, and J. Larsen, "Numerical simulation and experimental validation of blood flow in arteries with structured-tree outflow conditions," *Annals of Biomedical Engineering*, vol. 28, no. 11, pp. 1281–1299, 2000.

[43] N. P. Smith, A. J. Pullan, and P. J. Hunter, "An anatomically based model of transient coronary blood flow in the heart," *SIAM Journal on Applied Mathematics*, vol. 62, no. 3, pp. 990–1018, 2002.

[44] R. B. Bird, W. E. Stewart, and E. N. Lightfoot, *Transport Phenomena*. New York: J. Wiley, 2nd ed., 2002.

[45] C. F. Colebrook, "Turbulent flow in pipes, with particular reference to the transition region between the smooth and rough pipe laws," *Journal of the Institution of Civil Engineers*, vol. 11, no. 4, pp. 133–156, 1939.

[46] S.-Q. Yang and G. Dou, "Turbulent drag reduction with polymer additive in rough pipes," *Journal of Fluid Mechanics*, vol. 642, pp. 279–294, 2010.

[47] J. Kim and P. Moin, "Application of a fractional-step method to incompressible Navier-Stokes equations," *Journal of computational physics*, vol. 59, no. 2, pp. 308–323, 1985.

[48] N. N. Yanenko, *The Method of Fractional Steps The Solution of Problems of Mathematical Physics in Several Variables*. Berlin, Heidelberg: Springer Berlin Heidelberg, 1st ed., 1971.

[49] P. M. Gresho and R. L. Sani, "On pressure boundary conditions for the incompressible Navier-Stokes equations," *International Journal for Numerical Methods in Fluids*, vol. 7, no. 10, pp. 1111–1145, 1987.

[50] R. L. Sani, J. Shen, O. Pironneau, and P. M. Gresho, "Pressure boundary condition for the time-dependent incompressible Navier-Stokes equations," *International Journal for Numerical Methods in Fluids*, vol. 50, no. 6, pp. 673–682, 2006.

[51] S. Patankar and D. Spalding, "A calculation procedure for heat, mass and momentum transfer in three-dimensional parabolic flows," *International Journal of Heat and Mass Transfer*, vol. 15, no. 10, pp. 1787–1806, 1972.

[52] R. Issa, "Solution of the implicitly discretised fluid flow equations by operator-splitting," *Journal of Computational Physics*, vol. 62, no. 1, pp. 40–65, 1986.

[53] P. F. Galpin, J. P. Van Doormaal, and G. D. Raithby, "Solution of the incompressible mass and momentum equations by application of a coupled equation line solver," *International journal for numerical methods in fluids*, vol. 5, no. 7, pp. 615–625, 1985.

[54] I. E. Barton, "Comparison of simple- and piso-type algorithms for transient flows," *International journal for numerical methods in fluids*, vol. 26, no. 4, pp. 459–483, 1998.

[55] A. J. Chorin, "A numerical method for solving incompressible viscous flow problems," *Journal of computational physics*, vol. 2, no. 1, pp. 12–26, 1967.

[56] N. Shauer and C. A. Duarte, "Improved algorithms for generalized finite element simulations of three-dimensional hydraulic fracture propagation," *International journal for numerical and analytical methods in geomechanics*, vol. 43, no. 18, pp. 2707–2742, 2019.

[57] J. H. Ferziger and M. Peric, *Computational methods for fluid dynamics*. Berlin: Springer, 3rd, rev. ed., 2002.

[58] F. Shakib, T. J. Hughes, and Z. Johan, "A new finite element formulation for computational fluid dynamics: X. The compressible Euler and Navier-Stokes equations," *Computer Methods in Applied Mechanics and Engineering*, vol. 89, no. 1-3, pp. 141–219, 1991.

[59] H. K. Versteeg and W. Malalasekera, *An introduction to computational fluid dynamics : the finite volume method*. Harlow: Prentice Hall, 2nd ed., 2007.

[60] A. Skopintsev, E. Dontsov, P. Kovtunenko, A. Baykin, and S. Golovin, "The coupling of an enhanced pseudo-3D model for hydraulic fracturing with a proppant transport model," *Engineering Fracture Mechanics*, vol. 236, p. 107177, 2020.

[61] B. Carrier and S. Granet, "Numerical modeling of hydraulic fracture problem in permeable medium using cohesive zone model," *Engineering Fracture Mechanics*, vol. 79, pp. 312–328, 2012.

[62] L. Chen, F. Fathi, and R. de Borst, "Hydraulic fracturing analysis in fluid-saturated porous medium," *International Journal for Numerical and Analytical Methods in Geomechanics*.

[63] P. Papanastasiou, "The influence of plasticity in hydraulic fracturing," *International journal of fracture*, vol. 84, no. 1, pp. 61–79, 1997.

[64] E. Sarvaramini, M. B. Dusseault, and R. Gracie, "Characterizing the stimulated reservoir volume during hydraulic fracturing-connecting the pressure fall-off phase to the geomechanics of fracturing," *Journal of applied mechanics*, vol. 85, no. 10, 2018.

[65] E. Gordeliy and A. Peirce, "Enrichment strategies and convergence properties of the XFEM for hydraulic fracture problems," *Computer Methods in Applied Mechanics and Engineering*, vol. 283, no. C, pp. 474–502, 2015.

[66] A. Sanchez-Rivadeneira and C. Duarte, "A stable generalized/eXtended FEM with discontinuous interpolants for fracture mechanics," *Computer Methods in Applied Mechanics and Engineering*, vol. 345, pp. 876–918, 2019.

[67] A. Peirce and E. Detournay, "An implicit level set method for modeling hydraulically driven fractures," *Computer Methods in Applied Mechanics and Engineering*, vol. 197, no. 33-40, pp. 2858–2885, 2008.

[68] E. Gordeliy and E. Detournay, "A fixed grid algorithm for simulating the propagation of a shallow hydraulic fracture with a fluid lag," *International journal for numerical and analytical methods in geomechanics*, vol. 35, no. 5, pp. 602–629, 2011.

[69] A. Mikelić, M. F. Wheeler, and T. Wick, "A phase-field method for propagating fluid-filled fractures coupled to a surrounding porous medium," *Multiscale modeling & simulation*, vol. 13, no. 1, pp. 367–398, 2015.

[70] Z. A. Wilson and C. M. Landis, "Phase-field modeling of hydraulic fracture," *Journal of the mechanics and physics of solids*, vol. 96, pp. 264–290, 2016.

[71] R. H. Nilson, "Gas-Driven Fracture Propagation," *Journal of Applied Mechanics*, vol. 48, pp. 757–762, 12 1981.

[72] V. C. Tsai and J. R. Rice, "A model for turbulent hydraulic fracture and application to crack propagation at glacier beds," *Journal of Geophysical Research: Earth Surface*, vol. 115, no. F3, 2010.

[73] B. C. Ames and A. P. Bunger, "Role of Turbulent Flow in Generating Short Hydraulic Fractures with High Net Pressure in Slickwater Treatments," vol. Day 1 Tue, February 03, 2015 of *SPE Hydraulic Fracturing Technology Conference and Exhibition*, 02 2015.

[74] B. Gee and R. Gracie, "Beyond the cubic law: A finite volume method for convective and transient fracture flow," *International journal for numerical methods in fluids*, vol. 94, no. 11, pp. 1841–1862, 2022.

[75] E. Gordeliy and A. Peirce, "Coupling schemes for modeling hydraulic fracture propagation using the XFEM," *Computer methods in applied mechanics and engineering*, vol. 253, pp. 305–322, 2013.

[76] V. Tvergaard, "Effect of fibre debonding in a whisker-reinforced metal," *Materials science & engineering. A, Structural materials : properties, microstructure and processing*, vol. 125, no. 2, pp. 203–213, 1990.

[77] D. I. Garagash, "Cohesive-zone effects in hydraulic fracture propagation," *Journal of the Mechanics and Physics of Dolids*, vol. 133, p. 103727, 2019.

[78] D. Liu and B. Lecampion, "Propagation of a plane-strain hydraulic fracture accounting for a rough cohesive zone," *Journal of the Mechanics and Physics of Solids*, vol. 149, p. 104322, 2021.

[79] J. Kim, H. Tchelepi, and R. Juanes, "Stability and convergence of sequential methods for coupled flow and geomechanics: Fixed-stress and fixed-strain splits," *Computer Methods in Applied Mechanics and Engineering*, vol. 200, no. 13-16, pp. 1591–1606, 2011.

[80] J. Kim, H. Tchelepi, and R. Juanes, "Stability and convergence of sequential methods for coupled flow and geomechanics: Drained and undrained splits," *Computer Methods in Applied Mechanics and Engineering*, vol. 200, no. 23-24, pp. 2094–2116, 2011.

[81] U. Küttler and W. Wall, "Fixed-point fluid–structure interaction solvers with dynamic relaxation," *Computational Mechanics*, vol. 43, no. 1, pp. 61–72, 2008.

[82] F. Zhang, E. Dontsov, and M. Mack, "Fully coupled simulation of a hydraulic fracture interacting with natural fractures with a hybrid discrete-continuum method," *International Journal for Numerical and Analytical Methods in Geomechanics*, vol. 41, no. 13, pp. 1430–1452, 2017.

[83] B. Gee and R. Gracie, "Inertia Dominant and Transient Flow in Fractures - Beyond the Cubic Law," vol. All Days of *56th U.S. Rock Mechanics/Geomechanics Symposium*, 06 2022. ARMA-2022-0731.

[84] B. Gee and R. Gracie, "Non-Cubic Law Fracture Flow Phenomena," vol. All Days of *56th U.S. Rock Mechanics/Geomechanics Symposium*, 06 2022. ARMA-2022-0740.

[85] P. S. Virk, "Drag reduction fundamentals," *AIChE Journal*, vol. 21, no. 4, pp. 625–656, 1975.

[86] B. Lecampion and H. Zia, "Slickwater hydraulic fracture propagation: near-tip and radial geometry solutions," *Journal of Fluid Mechanics*, vol. 880, p. 514–550, 2019.

[87] M. Habibpour and P. E. Clark, "Drag reduction behavior of hydrolyzed polyacrylamide/xanthan gum mixed polymer solutions," *Petroleum science*, vol. 14, no. 2, pp. 412–423, 2017.

[88] B. Gee and R. Gracie, "Inertial and turbulent flow in hydro-mechanically coupled planar fractures," *Submitted to International Journal for Numerical and Analytical Methods in Geomechanics*, 2023.

[89] B. Lecampion, J. Desroches, R. G. Jeffrey, and A. P. Bunger, "Experiments versus theory for the initiation and propagation of radial hydraulic fractures in low-permeability materials," *Journal of Geophysical Research: Solid Earth*, vol. 122, no. 2, pp. 1239–1263, 2017.

[90] A. Bunger and B. Lecampion, "Four critical issues for successful hydraulic fracturing applications," in *Rock Mechanics and Engineering*, vol. 5, pp. 551–593, CRC Press, 1 ed., 2017.

APPENDICES

Appendix A

Finite Volume Continuity Correction Derivation

In this appendix, the continuity correction is derived and the equation is discretized. Given the current fluxes q^{n*} which do not satisfy continuity, the problem is to find the new fluxes q^n which do satisfy continuity while minimizing the difference the new and current fluxes. Therefore, the problem is to minimize the residual

$$R = \frac{1}{2}\int_0^L (q^n - q^{n*})^2 \, dx \tag{A.1}$$

subject to the constraint

$$0 = \frac{\partial}{\partial x}(q^n) + \frac{\partial}{\partial t}(w^n) \tag{A.2}$$

This problem can be addressed by introducing a Lagrange multiplier. The new problem is to find the saddle point of the Lagrangian,

$$\mathcal{L}(q^{n*}, \lambda) = \frac{1}{2}\int_0^L (q^n - q^{n*})^2 \, dx - \int_0^L \lambda \left(\frac{\partial}{\partial x}(q^n) + \frac{\partial}{\partial t}(w^n) \right) dx \tag{A.3}$$

in which $\lambda = \lambda(x)$ is the Lagrange multiplier. Let q^n be the field which minimizes the residual R, such that $R(q^n) = \min(R)$. Introducing a small variation δq, then

$$\mathcal{L} = \frac{1}{2}\int_0^L ((q^n + \delta q) - q^{n*})^2 \, dx - \int_0^L \lambda \left(\frac{\partial}{\partial x}(q^n + \delta q) + \frac{\partial}{\partial t}(w^n) \right) dx \tag{A.4}$$

$$\mathcal{L} = \min(R) + \delta R \tag{A.5}$$

$$\delta R = \int_0^L \delta q \, (q^n - q^{n*}) \, dx - \int_0^L \lambda \left(\frac{\partial}{\partial x}(\delta q) \right) dx \tag{A.6}$$

in which the second order terms involving $(\delta q)^2$ have been dropped. The Lagrangian can therefore be minimized if $\delta R = 0$. Integration by parts is applied to the second term in

δR.

$$\delta R = \int_0^L \delta q \left(q^n - q^{n*} + \frac{\partial \lambda}{\partial x} \right) dx - \lambda \delta q \Big|_0^L = 0 \tag{A.7}$$

On boundaries where q is prescribed, $\delta q = 0$ as both q^{n*} and q^n satisfy the given conditions, which leads to the boundary condition $\frac{\partial \lambda}{\partial x} = 0$ on Γ_q. On boundaries where pressure is prescribed, δq is not necessarily zero, so we set the condition that $\lambda = 0$ on Γ_p. Therefore, the surface term in δR goes to zero. For δR to go to zero for arbitrary δq, we find that

$$q^n - q^{n*} + \frac{\partial \lambda}{\partial x} = 0 \tag{A.8}$$

q^n is still unknown, but is constrained by the continuity equation. Therefore the derivative is taken to substitute in the known aperture velocity, $\dot{w}^n$.

$$0 = \frac{\partial}{\partial x}(q^n) - \frac{\partial}{\partial x}(q^{n*}) + \frac{\partial^2 \lambda}{\partial x^2} \tag{A.9}$$

$$\frac{\partial^2 \lambda}{\partial x^2} = \frac{\partial}{\partial t}(w^n) + \frac{\partial}{\partial x}(q^{n*}) \tag{A.10}$$

This provides an equation for λ, which can then be used to correct the fluxes according to

$$q^n = q^{n*} - \frac{\partial \lambda}{\partial x} \tag{A.11}$$

A.1 Discretization using the Finite Volume Method

The minimization problem produces an additional equation for a Lagrange multiplier that will correct the fluxes to meet continuity. This equation is discretized using the finite volume method.

First, the equation is integrated over the flux control volumes.

$$\int_{x_1^e}^{x_2^e} \frac{\partial^2 \lambda_i}{\partial x^2} dx = \int_{x_1^e}^{x_2^e} \frac{\partial}{\partial t}(w_i^n) dx + \int_{x_1^e}^{x_2^e} \frac{\partial}{\partial x}(q^{n*}) dx \tag{A.12}$$

$$\frac{\partial \lambda_i}{\partial x}\Big|_{x_1^e}^{x_2^e} = \Delta x \dot{w_i}^n + (q^{n*})\Big|_{x_1^e}^{x_2^e} \tag{A.13}$$

$$\frac{\partial \lambda_i}{\partial x}\Big|_{x_1^e}^{x_2^e} = \Delta x \dot{w_i}^n + \left(q_{i,2}^{n*} - q_{i,1}^{n*} \right) \tag{A.14}$$

Next, the derivative is discretized using a central differencing scheme, such that

$$\frac{\partial \lambda_i}{\partial x}\Big|_{x_1^e}^{x_2^e} = \left(\frac{\lambda_{i+1} - \lambda_i}{\Delta x} \right) - \left(\frac{\lambda_i - \lambda_{i-1}}{\Delta x} \right) \tag{A.15}$$

Thus the following discrete equation for λ is obtained.

$$\lambda_{i-1} - 2\lambda_i + \lambda_{i+1} = (\Delta x)^2 \dot{w_i}^n + \Delta x \left(q_{i,2}^{n*} - q_{i,1}^{n*}\right) \tag{A.16}$$

Last, the derivative of the Lagrange multiplier is constructed in each cell using central difference, such that

$$\frac{\partial \lambda_i}{\partial x} = \frac{\lambda_{i+1} - \lambda_{i-1}}{2\Delta x} \tag{A.17}$$

Then the fluxes may be corrected such that

$$q_i^n = q_i^{n*} - \frac{\partial \lambda_i}{\partial x} \tag{A.18}$$

A.2 Boundary Conditions on λ

λ is subject to the boundary conditions $\lambda = 0$ on Γ_p where pressure is prescribed, and $\frac{\partial \lambda}{\partial x} = 0$ on Γ_q where flux is prescribed. Implementation of the flux boundary condition is applied directly through the discrete equation.

In volume 1,

$$\left.\frac{\partial \lambda_i}{\partial x}\right|_{x_1^e}^{x_2^e} = \left(\frac{\lambda_2 - \lambda_1}{\Delta x}\right) - (0) \tag{A.19}$$

$$-\lambda_1 + \lambda_2 = (\Delta x)^2 \dot{w_1}^n + \Delta x \left(q_{1,2}^{n*} - q_{1,1}^{n*}\right) \tag{A.20}$$

In volume m,

$$\left.\frac{\partial \lambda_i}{\partial x}\right|_{x_1^e}^{x_2^e} = (0) - \left(\frac{\lambda_m - \lambda_{m-1}}{\Delta x}\right) \tag{A.21}$$

$$\lambda_{m-1} - \lambda_m = (\Delta x)^2 \dot{w_m}^n + \Delta x \left(q_{m,2}^{n*} - q_{m,1}^{n*}\right) \tag{A.22}$$

To implement the pressure boundary condition, a ghost cell is introduced outside of the domain such the interpolated value of λ between the ghost cell and the end cell satisfies the boundary condition. Using a linear interpolation between cell $i = 1$ and ghost cell $i = -1$

$$\lambda_1 + \lambda_{-1} = 0 \tag{A.23}$$

$$-3\lambda_1 + \lambda_2 = (\Delta x)^2 \dot{w_1}^n + \Delta x \left(q_{1,2}^{n*} - q_{1,1}^{n*}\right) \tag{A.24}$$

Using a linear interpolation between cell $i = m$ and ghost cell $i = m + 1$

$$\lambda_m + \lambda_{m+1} = 0 \tag{A.25}$$

$$\lambda_{m-1} - 3\lambda_m = (\Delta x)^2 \dot{w_m}^n + \Delta x \left(q_{m,2}^{n*} - q_{m,1}^{n*}\right) \tag{A.26}$$

Appendix B

Pressure Poisson Equation Finite Volume Discretization and Boundary Conditions

This appendix documents the details of the finite volume discretization the pressure Poisson equation.

B.1 Discretization of the Pressure Poisson Equation in the Domain

The PPE is discretized using the finite volume method by integrating over the pressure cells.

$$\int_{x_1^e}^{x_2^e} \frac{\partial}{\partial x}\left(\frac{w}{\rho_f}\frac{\partial p}{\partial x}\right)^n dx = -\int_{x_1^e}^{x_2^e} \frac{\partial}{\partial x}\left(H\right)^{n-1} dx - \int_{x_1^e}^{x_2^e} \frac{1}{\Delta t}\left(-\dot{w}^n + \dot{w}^{n-1}\right) dx \tag{B.1}$$

$$\frac{w^n}{\rho_f}\frac{\partial p^n}{\partial x}\bigg|_{x_1^e}^{x_2^e} = -H^{n-1}\bigg|_{x_1^e}^{x_2^e} - \frac{1}{\Delta t}\left(-\dot{w}^n + \dot{w}^{n-1}\right)\bigg|_{x_1^e}^{x_2^e} \tag{B.2}$$

$$H = \frac{\partial}{\partial x}(\alpha\frac{q^2}{w}) + \frac{1}{2}\frac{f_D}{w^2}q|q| \tag{B.3}$$

On the right-hand side, a central differencing scheme is used to discretize the derivatives of α, w, and q. All terms in the following equations are evaluated at the previous timestep $n-1$ unless otherwise noted.

First, the friction term evaluated over the control volumes gives

$$\frac{1}{2}\frac{f_D}{w^2}q|q|\bigg|_{x_1^e}^{x_2^e} = \frac{1}{2}\left(\frac{f_D(q_i)}{(w_i)^2}(q_i)|q_i| - \frac{f_D(q_{i-1})}{(w_{i-1})^2}(q_{i-1})|q_{i-1}|\right) \tag{B.4}$$

Next, the convective term is expanded and discretized, such that

$$-\frac{\partial}{\partial x}\left(\alpha\frac{q^2}{w}\right)\Bigg|_{x_1^e}^{x_2^e} = -\left(\frac{\partial\alpha}{\partial x}\frac{q^2}{w}\Bigg|_{x_1^e}^{x_2^e} + 2\alpha\frac{q}{w}\frac{\partial q}{\partial x}\Bigg|_{x_1^e}^{x_2^e} - \alpha\frac{(q)^2}{(w)^2}\frac{\partial w}{\partial x}\Bigg|_{x_1^e}^{x_2^e}\right) \tag{B.5}$$

The gradients over each flux cell are constructed using the face values of q, α and w in each flux cell.

$$\begin{aligned}-\frac{\partial}{\partial x}\left(\alpha\frac{q^2}{w}\right)\Bigg|_{x_1^e}^{x_2^e} = &-\left(\frac{q_i^2}{w_i^{n-1}}\frac{\alpha(q_{i,2})-\alpha(q_{i,1})}{\Delta x} - \frac{(q_{i-1})^2}{w_{i-1}}\frac{\alpha(q_{i-1,2})-\alpha(q_{i-1,1})}{\Delta x}\right)\\ &-2\left(\alpha(q_i)\frac{q_i}{w_i}\frac{q_{i,2}-q_{i,1}}{\Delta x} - \alpha(q_{i-1})\frac{q_{i-1}}{w_{i-1}}\frac{q_{i-1,2}-q_{i-1,1}}{\Delta x}\right)\\ &+\left(\alpha(q_i)\left(\frac{q_i}{w_i}\right)^2\frac{w_{i+\frac{1}{2}}-w_{i-\frac{1}{2}}}{\Delta x} - \alpha(q_{i-1})\left(\frac{q_{i-1}}{w_{i-1}}\right)^2\frac{w_{i-1+\frac{1}{2}}-w_{i-1-\frac{1}{2}}}{\Delta x}\right)\end{aligned} \tag{B.6}$$

Last, the continuity term is evaluated by assuming that the difference in $\dot{w}_i$ and $\dot{w}_{i-1}$ is small, such that the rate of aperture change across the cell is approximately constant. This leads to

$$-\frac{1}{\Delta t}\left(-\dot{w}^n + \dot{w}^{n-1}\right)\Bigg|_{x_1^e}^{x_2^e} \approx -\frac{\Delta x}{\Delta t}\left(-\dot{w}_{i-\frac{1}{2}}^n + \dot{w}_{i-\frac{1}{2}}^{n-1}\right) \tag{B.7}$$

Therefore, the combined pressure source term is given as

$$\begin{aligned}S_{pi} = &-\left(\frac{(q_i^{n-1})^2}{w_i^{n-1}}\frac{\alpha(q_{i,2})-\alpha(q_{i,1})}{\Delta x} - \frac{(q_{i-1}^{n-1})^2}{w_{i-1}^{n-1}}\frac{\alpha(q_{i-1,2})-\alpha(q_{i-1,1})}{\Delta x}\right)\\ &-2\left(\alpha(q_i)\frac{q_i^{n-1}}{w_i^{n-1}}\frac{q_{i,2}^{n-1}-q_{i,1}^{n-1}}{\Delta x} - \alpha(q_{i-1})\frac{q_{i-1}^{n-1}}{w_{i-1}^{n-1}}\frac{q_{i-1,2}^{n-1}-q_{i-1,1}^{n-1}}{\Delta x}\right)\\ &+\left(\alpha(q_i)\left(\frac{q_i^{n-1}}{w_i^{n-1}}\right)^2\frac{w_{i+\frac{1}{2}}^{n-1}-w_{i-\frac{1}{2}}^{n-1}}{\Delta x} - \alpha(q_{i-1})\left(\frac{q_{i-1}^{n-1}}{w_{i-1}^{n-1}}\right)^2\frac{w_{i-1+\frac{1}{2}}^{n-1}-w_{i-1-\frac{1}{2}}^{n-1}}{\Delta x}\right)\\ &-\frac{1}{2}\left(\frac{f_D(q_i)}{(w_i^{n-1})^2}(q_i^{n-1})|q_i^{n-1}| - \frac{f_D(q_{i-1})}{(w_{i-1}^{n-1})^2}(q_{i-1}^{n-1})|q_{i-1}^{n-1}|\right)\\ &-\frac{\Delta x}{\Delta t}\left(-\dot{w}_{i-\frac{1}{2}}^n + \dot{w}_{i-\frac{1}{2}}^{n-1}\right)\end{aligned} \tag{B.8}$$

B.2 Implementation of Neumann Boundary Conditions on PPE

The Neumann boundary condition is first examined in cell 1. Starting from the integrated PPE (3.16), the Neumann boundary condition (3.10) is introduced such that $\Gamma_q = x_1^e$,

which yields the governing equation in cell 1 as

$$\frac{w^n}{\rho_f}\frac{\partial p^n}{\partial x}\bigg|_{x_2^e} = -\frac{\partial}{\partial x}(\alpha\frac{q^2}{w})\bigg|_{x_2^e} - \frac{1}{2}\frac{f_D}{(w)^2}q|q|\bigg|_{x_2^e} - \frac{\Delta x}{\Delta t}\left(-\dot{w}^n + \dot{w}^{n-1}\right) - \frac{\partial q}{\partial t}\bigg|_{x_1^e} \tag{B.9}$$

The left-hand side is discretized as

$$\frac{w^n}{\rho_f}\frac{\partial p^n}{\partial x}\bigg|_{x_2^e} = \frac{w_1^n}{\rho_f}\left(\frac{p_2 - p_1}{\Delta x}\right) \tag{B.10}$$

while the right-hand side is discretized as

$$\begin{aligned} S_{p1} = &-\left(\frac{(q_1)^2}{w_1}\frac{\alpha(q_{1,2}) - \alpha(q_{1,1})}{\Delta x}\right) - 2\left(\alpha(q_1)\frac{q_1}{w_1}\frac{q_{1,2} - q_{1,1}}{\Delta x}\right) \\ &+\left(\alpha(q_1)\left(\frac{q_1}{w_1}\right)^2\frac{w_{1+\frac{1}{2}} - w_{1-\frac{1}{2}}}{\Delta x}\right) - \frac{1}{2}\left(\frac{f_D(q_1)}{(w_1)^2}(q_1)|q_1|\right) \\ &-\frac{\Delta x}{\Delta t}\left(-\dot{w}^n_{1-\frac{1}{2}} + \dot{w}^{n-1}_{1-\frac{1}{2}}\right) - \frac{1}{\Delta t}(\overline{q}^n - \overline{q}^{n-1}) \end{aligned} \tag{B.11}$$

The discrete equation for pressure in cell 1 with a flux boundary condition is therefore

$$p_1 - p_2 = -\frac{\Delta x \rho_f}{w_1^n}S_{p1} \tag{B.12}$$

Next, the Neumann boundary condition is examined in cell $m+1$. Starting from the integrated PPE (3.16), the Neumann boundary condition (3.10) is introduced such that $\Gamma_q = x_2^e$, which yields the governing equation in cell $m+1$ as

$$-\frac{w^n}{\rho_f}\frac{\partial p^n}{\partial x}\bigg|_{x_1^e} = -\frac{\partial}{\partial x}(\alpha\frac{q^2}{w})\bigg|_{x_1^e} - \frac{1}{2}\frac{f_D}{(w)^2}q|q|\bigg|_{x_1^e} - \frac{\Delta x}{\Delta t}\left(-\dot{w}^n + \dot{w}^{n-1}\right) + \frac{\partial q}{\partial t}\bigg|_{x_2^e} \tag{B.13}$$

The left-hand side is discretized as

$$-\frac{w^n}{\rho_f}\frac{\partial p^n}{\partial x}\bigg|_{x_1^e} = -\frac{w_m^n}{\rho_f}\left(\frac{p_{m+1} - p_m}{\Delta x}\right) \tag{B.14}$$

while the right-hand side is discretized as

$$\begin{aligned} S_{pm+1} = &-\left(-\frac{(q_m)^2}{w_m}\frac{\alpha(q_{m,2}) - \alpha(q_{m,1})}{\Delta x}\right) - 2\left(-\alpha(q_m)\frac{q_m}{w^m_{i-1}}\frac{q_{m,2} - q_{m,1}}{\Delta x}\right) \\ &+\left(-\alpha(q_m)\left(\frac{q_m}{w_m}\right)^2\frac{w_{m+\frac{1}{2}} - w_{m-\frac{1}{2}}}{\Delta x}\right) - \frac{1}{2}\left(-\frac{f_D(q_m)}{(w_m)^2}(q_m)|q_m|\right) \\ &-\frac{\Delta x}{\Delta t}\left(-\dot{w}^n_{m+\frac{1}{2}} + \dot{w}^{n-1}_{m+\frac{1}{2}}\right) + \frac{1}{\Delta t}(\overline{q}^n - \overline{q}^{n-1}) \end{aligned} \tag{B.15}$$

The discrete equation for pressure in cell $m+1$ with a flux boundary condition is therefore

$$p_{m+1} - p_m = -\frac{\Delta x \rho_f}{w_m^n}S_{pm+1} \tag{B.16}$$

Appendix C

Definitions of Jacobian Derivative Matrices for the Hydro-Mechanically Coupled Model

The component matrices of the fully-coupled monolithic system Jacobian are defined in this appendix.

$$\mathbf{K}_{uu} = \mathbf{K}_{elastic} + \mathbf{K}_{cohesive} \tag{C.1}$$

$$\mathbf{K}_{elastic} = \int_{\Omega_s} \mathbf{B}^\top \mathbf{D}\mathbf{B} d\Omega \tag{C.2}$$

$$\mathbf{K}_{cohesive} = -\int_{\Gamma_c} \mathbf{N}^\top \boldsymbol{n}_{\boldsymbol{\Gamma_c}} \frac{\partial t^{coh}}{\partial w} \boldsymbol{n}_{\Gamma_c} [\![\mathbf{N}]\!] d\Gamma \tag{C.3}$$

$$\mathbf{K}_{up} = \int_{\Gamma_c} \mathbf{N}^\top \boldsymbol{n}_{\Gamma_c} \boldsymbol{\psi} d\Gamma \tag{C.4}$$

$$\mathbf{K}_{cu}(i,j) = \frac{3\Delta x}{2\Delta t} \boldsymbol{n}_{\boldsymbol{\Gamma_c}} \cdot [\![\mathbf{N}]\!] \Big|_{x_{i,1}}, \forall j \tag{C.5}$$

$$\mathbf{K}_{cq}(i,[i-1,i]) = \begin{bmatrix} -1 & 1 \end{bmatrix} \tag{C.6}$$

$$\mathbf{K}_{mp}(i,[i,i+1]) = \frac{w_i}{\rho_f} \begin{bmatrix} -1 & 1 \end{bmatrix} \tag{C.7}$$

$$\begin{aligned} \mathbf{K}_{mu}(i,j) = &- \frac{\alpha(q_{i,2})}{w_{i,2}^2} (q_{i,2})^2 \boldsymbol{n}_{\boldsymbol{\Gamma_c}} \cdot [\![\mathbf{N}]\!] \Big|_{x_{i,2}} \\ &+ \frac{\alpha(q_{i,1})}{w_{i,1}^2} (q_{i,1})^2 \boldsymbol{n}_{\boldsymbol{\Gamma_c}} \cdot [\![\mathbf{N}]\!] \Big|_{x_{i,1}} \\ &+ \left[\frac{p_{i+1} - p_i}{\rho_f} + \Delta x \frac{1}{2w_i^2} q_i |q_i| \frac{\partial f_D}{\partial w} - \Delta x \frac{f_D(q_i)}{w_i^3} (q_i) |q_i| \right] \boldsymbol{n}_{\boldsymbol{\Gamma_c}} \cdot [\![\mathbf{N}]\!] \Big|_{x_i} \end{aligned} \tag{C.8}$$

At $Re < Re_T$, where Re_T is the threshold Reynolds number which defines the transition between the turbulent and transitional regimes, $\frac{\partial f_D}{\partial w} = 0$. At $Re > Re_T$, the derivative $\frac{\partial f_D}{\partial w}$ is generally small, though the computational effort associated with computing derivative (which is defined implicitly) is high. It is therefore preferable to assume that $\frac{\partial f_D}{\partial w} = 0 \, \forall Re$.

The matrix $\mathbf{K}_{mq}$ is defined as

$$\mathbf{K}_{mq} = \frac{\partial \mathbf{F}_t}{\partial \mathbf{q}^n} + \frac{\partial \mathbf{F}_c}{\partial \mathbf{q}} + \frac{\partial \mathbf{F}_f}{\partial \mathbf{q}} \tag{C.9}$$

The derivative of the forcing vector $\mathbf{F}_t$ is defined as

$$\frac{\partial \mathbf{F}_t}{\partial \mathbf{q}^n}_i = \frac{3\Delta x}{2\Delta t} \tag{C.10}$$

The derivative of the convective forcing vector, F_c, depends on the interpolation scheme for the cell faces. The implementation adopted in this paper uses the QUICK scheme for non-uniform meshes. The version presented here assumes a uniform structured mesh. Let $\mathbf{Q}_i$ be the 5×1 matrix of cell face flux derivatives defined for each row i with column entries $i-2, i-1, i, i+1, i+2$.

In a structured mesh, case 1: $q_i \geq 0$

$$\mathbf{Q}_{i,1} = \frac{\partial q_{i,1}}{\partial \mathbf{q}}(i-2, i-1, i, i+1, i+2)_i = \frac{1}{8}\begin{bmatrix} -1 & 6 & 3 & 0 & 0 \end{bmatrix} \tag{C.11}$$

$$\mathbf{Q}_{i,2} = \frac{\partial q_{i,2}}{\partial \mathbf{q}}(i-2, i-1, i, i+1, i+2)_i = \frac{1}{8}\begin{bmatrix} 0 & -1 & 6 & 3 & 0 \end{bmatrix} \tag{C.12}$$

case 2: $q_i < 0$

$$\mathbf{Q}_{i,1} = \frac{\partial q_{i,1}}{\partial \mathbf{q}}(i-2, i-1, i, i+1, i+2)_i = \frac{1}{8}\begin{bmatrix} 0 & 3 & 6 & -1 & 0 \end{bmatrix} \tag{C.13}$$

$$\mathbf{Q}_{i,2} = \frac{\partial q_{i,2}}{\partial \mathbf{q}}(i-2, i-1, i, i+1, i+2)_i = \frac{1}{8}\begin{bmatrix} 0 & 0 & 3 & 6 & -1 \end{bmatrix} \tag{C.14}$$

Thus, the derivative of the convective forcing vector $\mathbf{F}_c$ with respect to the nodal fluxes is

$$\frac{\partial F_c}{\partial \mathbf{q}}_i = \frac{2\alpha(q_{i,2})}{w_{i,2}} q_{i,2} \mathbf{Q}_{i,2} - \frac{2\alpha(q_{i,1})}{w_{i,1}} q_{i,1} \mathbf{Q}_{i,1} \tag{C.15}$$

It is assumed here that $\frac{\partial \alpha}{\partial q} = 0$, which is true in the laminar and turbulent regimes.

Last, the derivative of the friction forcing vector $\mathbf{F}_f$ with respect to the nodal fluxes is divided by flow regime.

$$\frac{\partial F_f}{\partial q_i} = \frac{\Delta x}{w_i^2}\left(f_D |q_i| + \frac{1}{2} q_i |q_i| \frac{\partial f_D}{\partial q_i} \right) \tag{C.16}$$

In the laminar regime,

$$f_D = \frac{24}{Re} = \frac{24\nu}{|q_i|} \tag{C.17}$$

$$\frac{\partial f_D}{\partial q_i} = -\frac{24\nu}{q_i|q_i|} \tag{C.18}$$

$$\frac{\partial F_f}{\partial q_i} = \frac{12\Delta x\nu}{w_i^2} \tag{C.19}$$

In the transitional regime,

$$f_D = f_{DL} + (Re_i - Re_L)\frac{f_{DT} - f_{DL}}{Re_T - Re_L} \tag{C.20}$$

$$\frac{\partial f_D}{\partial q_i} = \frac{f_{DT} - f_{DL}}{Re_T - Re_L} \cdot \frac{\text{sign}(q_i)}{\nu} \tag{C.21}$$

in which $Re_L, f_{DL} = f_D(Re_L)$ are the Reynolds number and friction factor at the transition from the laminar regime to the transitional regime, and $Re_T, f_{DT} = f_D(Re_T)$ are the Reynolds number and friction factor at transition from the transitional regime to the turbulent regime.

In the turbulent regime,

$$\frac{1}{\sqrt{f_D}} = -2\log\left(\frac{\epsilon}{7.4w} + \frac{2.51}{Re\sqrt{f_D}}\right) \tag{C.22}$$

$$\frac{\partial f_D}{\partial q_i} = -\frac{10.04\nu}{\ln 10}\left(\frac{\epsilon}{7.4w_i} + \frac{2.51}{Re\sqrt{f_D}}\right)^{-1}\frac{f_D}{q_i^2}\left(1 + \frac{5.02\nu}{(\ln 10)q_i}\left(\frac{\epsilon}{7.4w_i} + \frac{2.51}{Re\sqrt{f_D}}\right)^{-1}\right)^{-1} \tag{C.23}$$